Quantitative Dynamic PET Imaging of the Heart: From Mouse to Man

Min Zhong
Wuhan, Hubei, China

Bachelor of Science, University of Science and Technology of China, 2009

A Dissertation presented to the Graduate Faculty
of the University of Virginia in Candidacy for the Degree of
Doctor of Philosophy

Department of Physics

University of Virginia
May, 2014

Abstract

Positron emission tomography (PET) imaging is an excellent tool to evaluate molecular, metabolic, physiologic and pathologic conditions of the body for diagnosis, therapy planning and research. It is based on annihilation coincidence detection technique, wherein a positron annihilates with an electron to generate two 511 keV photons that can be detected simultaneously. Several factors such as the detector element size, positron range, and noncollinearity of annihilation photons together limit the system spatial resolution of a PET system. Quantification of PET data is thus very challenging due to the limited spatial resolution. Tracer kinetic modeling is commonly used for quantitative evaluation of dynamic PET data. The image derived time-resolved curves are susceptible to incomplete radioactivity recovery called partial volume (PV) effect, and cross-contamination between adjacent regions called spillover (SP) effect, thereby image derived data do not reflect the true activity concentration in the region of interest. The objective of this dissertation is to develop tracer kinetic models for evaluation of metabolism and perfusion in the heart using dynamic PET imaging *in vivo*, accounting for PV and SP corrections.

Using Siemens microPET Focus F120 small animal scanner, efforts were devoted into the development and validation of an *in vivo* quantification methodology for 2-[18F] fluoro-2deoxy-D-glucose (FDG) dynamic PET images of mouse heart, which can simultaneously give an accurate estimation of metabolic kinetic parameters, and model

corrected blood input function with PV and SP corrections in a 3-compartment glucose transport model [1]. This advanced method not only improves quantitation but is also repeatable. Using the developed kinetic model, this dissertation also discussed the non-invasive measurement of the myocardial glucose uptake rate *ki* in mouse heart subjected to transverse aortic constriction (TAC) surgery induced pressure overload left ventricle hypertrophy (LVH), to test the hypothesis that metabolic changes precede and possibly trigger cardiac dysfunction in the pressure overloaded heart [2].

Adapting the quantification methodology developed in small animals to clinical practice, a first-in-human study was carried out on a Siemens Biograph mCT PET/CT clinical scanner using dynamic FDG PET imaging, to test the hypothesis that significant changes in glucose metabolism precede any structural and functional changes of the heart in patients with hypertension [3][4].

Also, this dissertation explored quantitative assessment of absolute blood flow in mouse heart using dynamic ^{13}N-ammonia PET imaging in a 3-compartment tracer kinetic model [5]. Larger positron range of isotope ^{13}N leads to further degradation of the spatial resolution, thereby making quantification more challenging than that in FDG PET imaging. Poor image quality, small size of the mouse heart and rapid heart rate results in significant PV effect and SP contamination. A quantitative 3-compartment tracer kinetic model was developed to measure blood flow in mouse heart *in vivo*. A correlation between blood flow and metabolism was established in the stressed mouse heart, for the first time, using dynamic ^{13}N-ammonia and FDG PET imaging respectively.

Acknowledgements

After a long cold winter, it is spring again in this small town. As I am approaching to the end of my student life, I would like to express my sincere appreciations to all the people who supported and encouraged me in this important era of my life.

My first gratitude goes to my thesis advisor, Prof. Bijoy Kundu, for all I have learned from him and his constant help throughout my graduate study. His continuous guidance helped me succeed, and his scientific dedication lightened my way. From the past four years, not only have I gained the knowledge that solves specific problems, but also I have acquired the methodology that will benefit me for a life time. I truly appreciate his professional advice as a mentor and his personal guidance as a friend.

I am grateful to Prof. Heinrich Taegtmeyer for sharing his knowledge and experience, and fruitful discussions on our projects. I would like to thank Drs. Jamieson Bourque, Yasmin Hamirani, David Glover and Julien Dimastromatteo, for the collaboration and effective teamwork. Many thanks to my colleagues: Dr. Landon Locke, Clayton Alonso, and Maanasi Mistry for working and solving the difficult problems together. I also would like to thank Gina Wimer and Bobi Thornhill for their productive assistance. The Physics department made sure I am on the track, and the Molecular Imaging Core provided me with a great platform to launch a range of interesting and useful projects. Therefore, I would like to thank all the members of department of Physics, Radiology and Medical Imaging for their support. It was a great pleasure to work in such a congenial and enjoyable environment.

I would like to express my special thanks to my dissertation committee members: Prof. P.Q. Hung, Prof. Gordon Cates, and Prof. Mark Williams. Thank you for all the insightful suggestions about my thesis research and my career concerns.

Last but not least, I would like to send my deepest thanks to my parents Weifang Liu and Yaosheng Zhong for making me who I am. Your unconditional love, support and beliefs in me are my greatest encouragement during the hard times. I would like to dedicate this dissertation work to you, my dearest mother and father.

Table of Contents

List of Figures

List of Table

1 Introduction

1.1 Fundamental Concepts of Nuclear Medicine

Nuclear medicine is a medical specialty. It uses safe, noninvasive and low-cost method of radioactive principle, to evaluate molecular, metabolic, physiologic and pathologic conditions of the body for diagnosis, therapy and research.

In nuclear medicine study and preparation, gamma-ray-emitting or positron-emitting radionuclides are combined with other elements to form radioactive substances, or combined with existing pharmaceutically active molecules to form radiopharmaceuticals, which happen to have chemical properties that allow them to be concentrated in places of medical interest for disease detection. The radiopharmaceuticals are more commonly referred as traces or radiotracers.

Nuclear medicine uses very low dosage of radiopharmaceuticals to diagnose and treat disease. Once the radiopharmaceutical is administered into the body, it can be localized in specific organs or cellular receptors, after which the radionuclide tracer atom enables it to be detected with a gamma camera or other imaging device, which then can provide very precise images of the body area being imaged. This property of radiopharmaceutical allows nuclear medicine the ability to image the extent of the metabolic process in the body, based on the chemical and biological properties of the radiopharmaceutical itself, rather than relying on structural changes in the tissue anatomy.

Nuclear medicine treatment of diseased tissue is using focused high energy ionizing radiation interfering cell multiplying based on metabolism. Cells multiply rates differs and the quicker multiplying cells are affected much stronger than standard cells, so the diseased cells have less time for detecting and fixing DNA errors before they multiply, so it is more likely to destroy them when corrupted by nuclear radiation [6].

1.2 Advantages of Nuclear Medical Imaging

Nuclear medical imaging is different from most of the traditional diagnostic imaging modalities that provide outstanding anatomic images but are limited in the ability of providing functional processes information, such as x-ray computed tomography (CT) and magnetic resonance imaging (MRI). They offer the potential to identify abnormalities at very early stage in the progression of the disease *in vivo* long before some medical problems are anatomically apparent. This early detection provides an early intervention timing window in the disease progression when there may be a better prognosis [7].

Nuclear medicine studies have the ability to provide exquisitely sensitive measurements of a wide range of functional processes in the body non-invasively. In addition, there are also nuclear medicine studies that allow imaging of the whole body depends on certain radiopharmaceuticals and functions [8][9]. Information regarding the location of abnormally active metabolism obtained from the whole-body scan helps physicians effectively pinpoint the source of disease [10].

To understand of biological processes at the cellular level in living organs is expanding [11]. Innovation and development of new tracers technology and “smart probes” [12] enable not only visualization and characterization of biological processes at the molecular level, but also quantification analysis, which allow nuclear medicine to be more organ- or tissue-specific and reveal very specific functional process of interest underlying a particular disease [13][14].

1.3 Diagnostic Nuclear Medical Imaging

There are two major instruments of nuclear medicine imaging: positron emission tomography (PET) and single photon emission computed tomography (SPECT). PET scan provides a three-dimensional image of functional processes within the body. Positrons are emitted during radiopharmaceuticals decay, followed by annihilation with an electron in the surrounding tissue; simultaneously send two photons in opposite directions that subsequently are detected by the gamma-ray cameras grouped around the body. The distribution of the recorded events is used to assess the distribution of the injected radiopharmaceuticals or products of metabolized radiopharmaceuticals, and to calculate the tomographic images.

Single photon imaging technique uses radionuclides that emit single instead of double gamma rays, which can be measured by using a gamma-ray camera directly. The image obtained by a gamma-ray camera from one particular angle is a planar view of 3-D distribution of the radionuclides with the body (also called projection), and SPECT imaging is performed by using a gamma-ray camera to acquire multiple 2-D projections from multiple angles. This information can be presented as cross-sectional slices along any chosen axis through the body.

The higher efficiency of PET scanner detects and records coincident events in time, which provides more radiation event localization information, thus higher resolution than

SPECT. However, SPECT offers a wider observation timing window due to its longer half-life radionuclides, thus allowing nuclear medicine researchers to observe longer biological process *in vivo* several hours or days after administration of the radiopharmaceutical [15].

1.4 Motivation

Nuclear medicine studies determine the cause of the medical problem based on functional process, it has major impacts on diagnosis and treatment of disease, among which PET scans allow researcher do accurate quantitative analysis to obtain more information [16], thus exploit the way that the body handles substance differently when there is a disease progressing. For example, PET can detect most cancer stages, often before they are evident through other medical tests. PET can also give important early detection about cardiovascular disease and many neurological disorders, like Alzheimer's.

While the quantification ability of PET data is unique and unsurpassed, it has its own limitations. The highest resolution of PET scanner is limited by physical and geometrical conditions, which introduces in inaccuracy in quantitative analysis [17]. Hence, there is a need to develop *in vivo* correction techniques of accurate PET data quantification for the diagnosis and treatment of disease.

2 Physics of Positron Emission Tomography

2.1 Basic Nuclear Physics Principles in PET

Radioactive decay is a physical process that an unstable nucleus loses energy by emitting particles of ionizing radiation, and transform to a nucleus in a more stable state, or to a nucleus containing different numbers of protons and neutrons. Among many different types of radioactive decay, positron emission, or called beta plus decay (β^+ decay) is a particular type of radioactive decay.

2.1.1 Unit of Radioactive Measurements

Radioactive activity is measured in SI-derived unit becquerel (Bq) or non-SI unit curie (Ci) [18]. One Bq is defined as the amount of radioactive material of which one nucleus decays per second.

$$1\,Bq = 1\,\text{decay per second} = 1\,s^{-1} \tag{2-1}$$

The non-SI unit Ci was originally defined as the activity of the quantity of radium emanation (radon-222) in equilibrium with one gram of radium isotope Ra-226. At present the curie is equal, by definition, to 3.7×10^{10} decays per second.

$$1\,Ci = 3.7\times10^{10}\,s^{-1} = 3.7\times10^{10}\,Bq \tag{2-2}$$

The unit curie is current discouraged by the SI. Low activities are also measured in disintegration per second (dpm).

2.1.2 Positron Emission and Annihilation

In a β^+ decay, an unstable radionuclide nucleus loses energy, a proton inside the nucleus emits a positron (e^+) and an electron neutrino (ν_e) while it is converted into a neutron. Schematically, the process is

$$p^+ \rightarrow n + e^+ + \nu_e \qquad \textbf{2-3}$$

The positron is emitted with a neutrino that is not detected. Positron emission typically happens in proton-rich radionuclides since the decay decreases proton number relative to neutron number.

The positron is the antiparticle of an ordinary electron (e^-), it has a very short life after ejection from the nucleus in electron-rich matters. The low-energy positron rapidly loses its kinetic energy in collisions with atomic electrons in the surrounding matter. The collision results in the annihilation of both the positron and electron, and creation of gamma ray photons [19][20][21]. The frame of reference in which the positron-electron system has zero net linear momentum before the annihilation, and this is also the most common case, thus two gamma ray photons are emitted in opposite direction after collision, and the rest energy of the positron and electron is evenly shared between them:

$$E = m_p c^2 = m_e c^2 = 511\,keV \qquad \textbf{2-4}$$

$$e^+ + e^- \rightarrow \gamma + \gamma \qquad \textbf{2-5}$$

The energy is released as a pair of high-energy gamma ray photons. Higher order annihilation is also possible [21], but the probability becomes lower because these more complex processes have lower probability amplitudes. It only occurs in about 0.003% [22][23] of all annihilations.

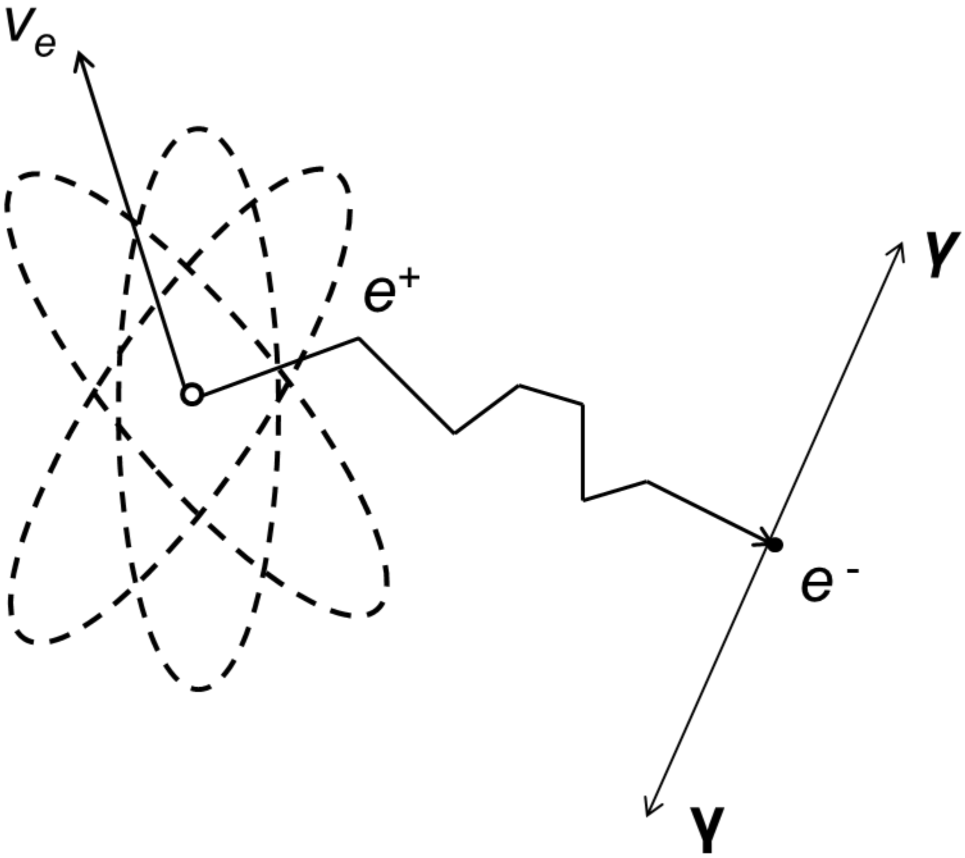

Figure 2-1 Positron-electron annihilation as a result of β^+ decay.

Positron emission and annihilation are very useful in nuclear medicine studies. First, the annihilation gamma ray photons are very energetic (511 keV) that they have a good chance of escaping from the body to be detected externally. Second, the two opposite annihilation photons are emitted following a precise geometric relationship, which enables PET to localize the annihilation event position [19][20]. It can be used as a good indicator of where the radioactive atoms are in the body because the annihilation event site is very close to the positron emission point.

2.2 Events Detection in PET

A PET scanner is designed to detect the simultaneous emitted back-to-back annihilation photons and localize the site of corresponding positron emission events. This unique mechanism is called annihilation coincidence detection (ACD) [24][25].

2.2.1 Coincidence Detection

A simple coincidence detection system consists of a pair of 511 keV gamma radiation detectors with associated electronics and a coincidence circuit.

The simultaneous detection of two annihilation photons allows PET to determine the annihilation site from which line the annihilation photons were emitted along, or more accurately which part of volume, connecting the two detectors. This line between the coincidence detector pairs is referred as a line of response (LOR). To obtain the complete 3D information of an object, a large number of LORs data are collected at different angles and different radial offsets that cover the entire field of view of the PET system. In a typical PET scan, millions of pairs of annihilation photons will be detected and recorded after a positron-emitting nucleus labeled chemical compound being administrated into the body [26][27].

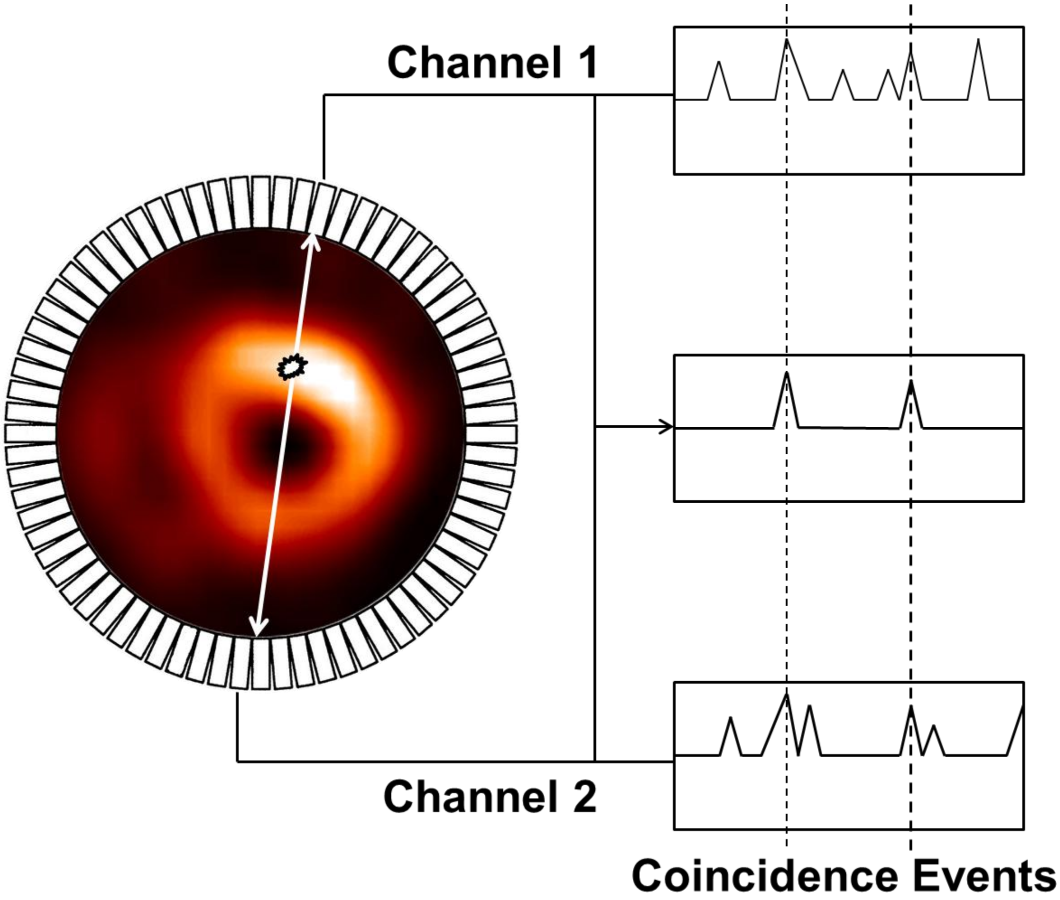

Figure 2-2 Diagram of a basic annihilation coincidence detection system.

Identically the two annihilation photons are emitted and detected simultaneously. Opposing detectors will generate timing signals for the pulses stimulated by the incident photons, which can then by analyzed by coincidence logic circuits. However, due to different distance travelled by two photons from the annihilation event point to the detectors, as well as different time delays in signal transit through electronics and cables, a small finite timing window is needed to avoid missing coincidence events. A coincidence event is determined by when a pair of photons are recorded within this coincidence timing window. In the same time, the timing window should be as narrow as possible to prevent from detection of other types of unrelated events that accidentally happen within the timing window. Usually the width of timing window is chosen to be as wide as the time resolution of a pair of coincidence detectors, which is 6-12 ns. Timing signal is generated from each pulse, and then it is passed to coincidence circuitry for processing [28].

Figure 2-3 shows the mechanism of a coincidence circuit. Except for the time-of-flight effect, two timing pulses arising from the same coincidence event usually can have some time differences due to the finite time resolution of the detector and coincidence circuit. To address this issue, a gate generator is adopted to process the timing pulses and then creates an electronic pulse lasts for time Δt, which is known as the coincidence resolving time of the system [26][27]. These fixed-width pulses then pass through a logic unit, which generates a pulse if there are two signals processing at the same time [29]. For example, a coincidence event will be recorded if a timing pulse is detected on one channel at time t, while there is another timing pulse detected on the other channel between $t - \Delta t$ and $t + \Delta t$. There are set criteria for choosing the value of Δt. If Δt is too small compared to the time resolution of the detection system, many true coincidences will be missed. If Δt is too large, more coincidences other than true events will be counted.

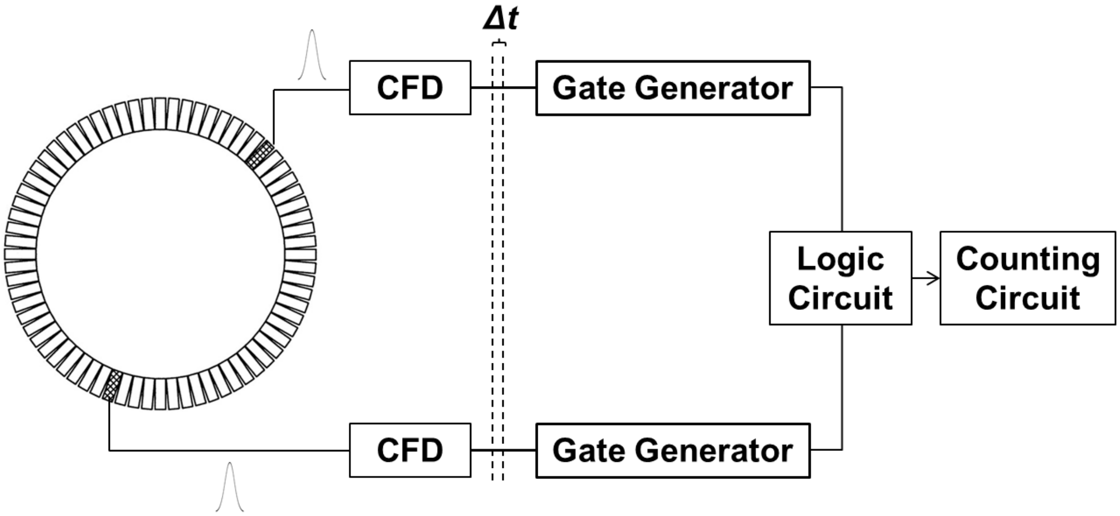

Figure 2-3 Schematic diagram showing timing signal processing in a PET camera.

If choosing sufficiently small Δt, then time-of-flight effects may arise problems. These effects occur when one photon from an annihilation event takes significantly different time to reach the detectors than the other. With proper alterations made to the PET imaging systems, time-of-flight information can be used for improving spatial resolution and signal-to-noise ratio [30]. These require extremely fast scintillators such as barium fluoride (BaF_2), which has a fast-component decay constant of 0.8 ns.

2.2.2 Types of Events

In the majority of total events detected by the PET system, only one of the two annihilation photons is registered. The other photon may be not on a trajectory that would intersect a detector, or may not deposit enough energy in the detectors to be registered. Normally these single events are rejected by the system.

ACD generates a signal whenever a pair of events is recorded by opposing detectors with the timing window, and all the events detected by the coincidence circuit in a PET system are referred as prompt coincidences [26][29]. In ideal discussion, only true coincidence events result from a pair of photons produced by the same annihilation event would be recorded. However, due to other possible interactions of the 511 keV photons within the object body, other types prompt coincidence could also occur within the timing window.

First shown in Figure 2-4 B is random coincidence. Random coincidence occurs when two photons from two seperate events are detected by opposing detectors within the width of timing window and recorded as coincidence event. This type of events is not rare and can occur anywhere even including the activity outside the field of view (FOV) of the scanner. The rate of random coincidence can be estimated by [26][29]:

$$R_{ij} = 2\tau N_1 N_2 \tag{2-6}$$

where R_{ij} is the rate of random coincidence, τ is coincidence timing window, and N_1, N_2 are the counting rates of the detector pair of interest. The random coincidence rate is proportional to the square of activity in the FOV and the width of coincidence window, while the rate of true coincidence events is directly proportional to the activity in the FOV. Random coincidences do not provide useful spatial information about the activity distribution, but create an approximately uniform background across the FOV of scanner, lower the image contrast and bring inaccuracy to quantification of activity within the object.

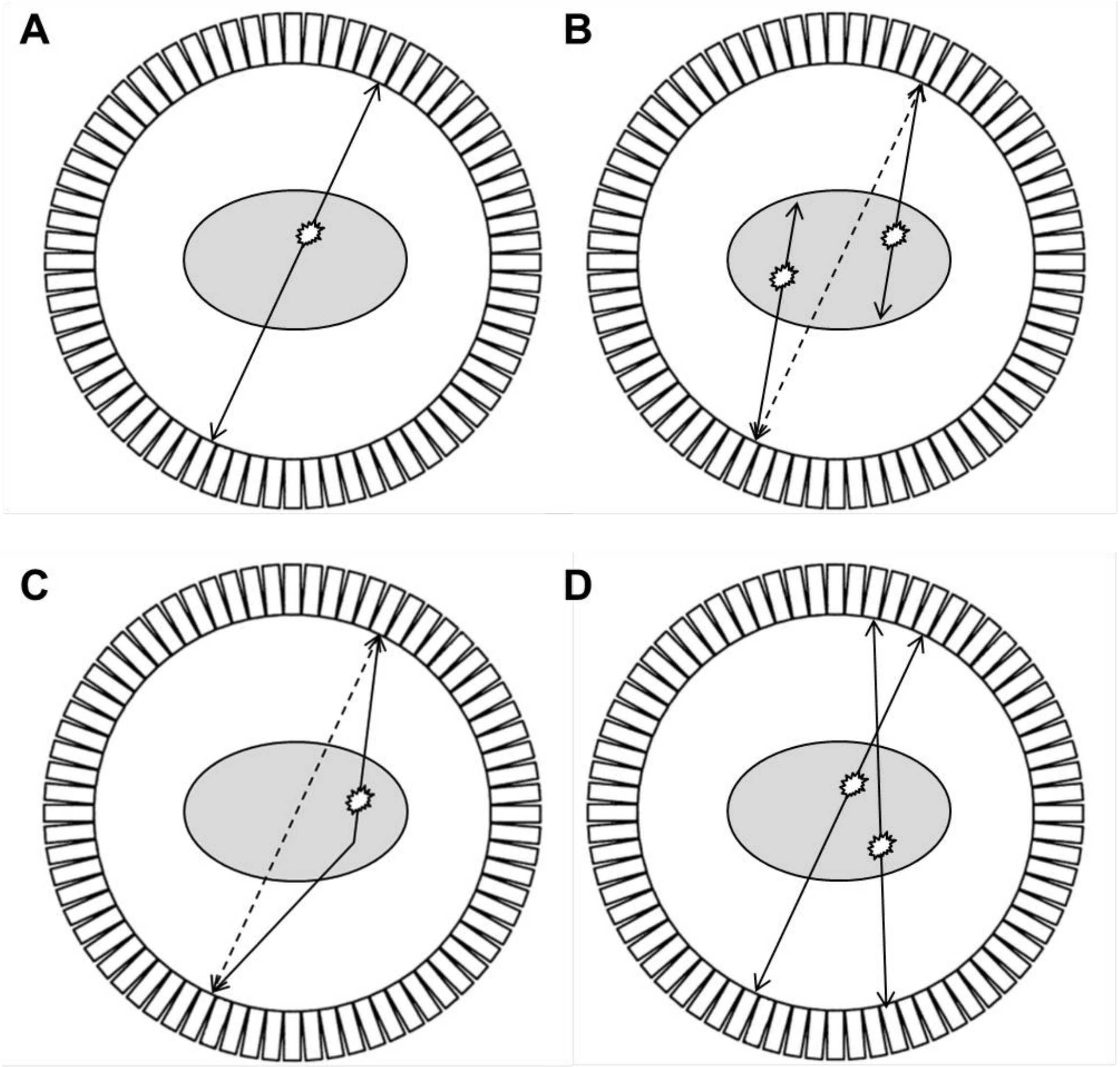

Figure 2-4 Different types of coincidence events. (A)True coincidence, (B) Random coincidence, (C) Scattered Coincidence, (D) Multiple Coincidence.

Another type of the invalid prompt coincidence is scattered coincidence [26][29] (Figure 2-4 C). These events occur originally from true coincidences, but one or both two annihilation photons have undergone scatter interactions and changed direction before they reach the detectors. In a scattered coincidence, the scattered photon is detected by detector other than the one that would correctly present for the original true event. The spatial information carried by a scatter coincidence is not true because the change of photon emitting direction changes the corresponding LOR. So the rate of scattered coincidence depends more on the distribution of activity, the attenuation property of object and geometry of PET cameras; also it is proportional to the activity in the FOV as the rate of true coincidence. Scattered coincidence leads to mispositioning events that are not directly correlated with position and could decrease contrast and cause an over estimation of isotope concentrations.

Multiple coincidences [26][29] (Figure 2-4 D) occur when three or more photons are detected in multiple detector pairs within the width of timing window. In multiple coincidences, it is hard to determine which LOR should be assigned to the event, so usually the event is rejected or assigned a position in between the events.

The prompt coincidence consists of true, random and scattered coincidence where only true coincidences carry the spatial information regarding the distribution of activity. It is important to estimate the percentage of the total prompt coincidences that result from random and scatter coincidences, which can then be removed to yield the actual distribution of the radiotracer.

2.3 Detector Principles and Configurations in PET System

To record millions of annihilation events in one PET scan from all directions, a large number of small detector pairs are need to be arranged in an array around the object, or a large area detector need to be placed near the object with the ability of determining positions hit by 511 keV photons enabled. Also, it is crucial for the detectors to be able to precisely identify when a photon strike the detectors, thus all the collected times can be compared to determine when the annihilation pairs were emitted.

2.3.1 Scintillation Detectors

Scintillators are transparent materials that exhibit the property of emitting visible light when excited by ionizing radiation (scintillation). These materials can be in solid, liquid or gas form and can be organic or inorganic compounds. The scintillation process converts high-energy photons into visible light via interaction with a scintillating material. In scintillators, when an incoming high energy photon strike and gets absorbed, it creates an energetic electron by either photoelectric absorption or Compton process. A photoelectric energy distribution is determined by photoelectric absorption and Compton scatter generate electrons of different. In photoelectric absorption, all the photon energy is transferred to the electron, so the energy distribution of the photoelectrons is sharply peaked close to the energy of the incident 511 keV photon [31][32]. In Compton scattering (Figure 2-5), the energy of scattered electron depends on the scattering angle [18]:

$$E^{'} = \frac{E}{1 + \frac{E}{m_e C^2}(1 - \cos\varphi)} \tag{2-7}$$

where φ is the photon scattering angle, E is the energy of the incident photon and E' is the energy of the scattered photon. E' reaches a maximum when φ = 0. A typical theoretical energy distribution spectrum for the electrons interacted with 511 keV photons is shown in Figure 2-6.

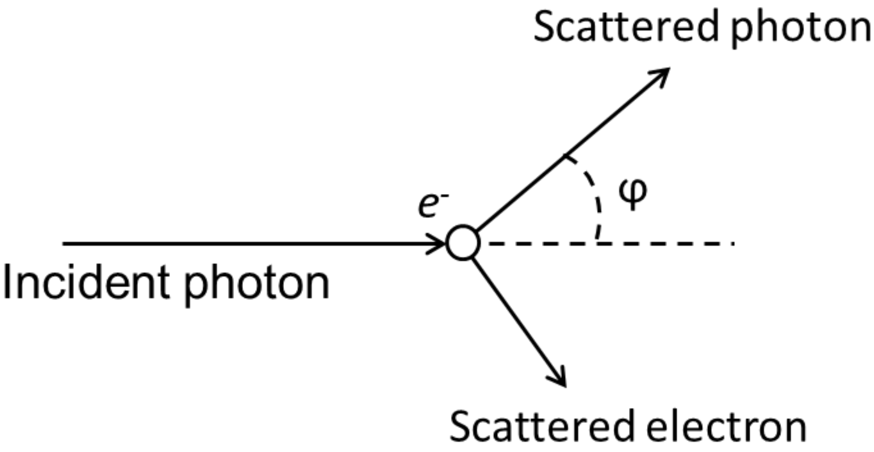

Figure 2-5 Compton scattering. A photon of energy *E* collides with a target electron at rest, then a new photon of energy *E'* emerges at scattering angle φ.

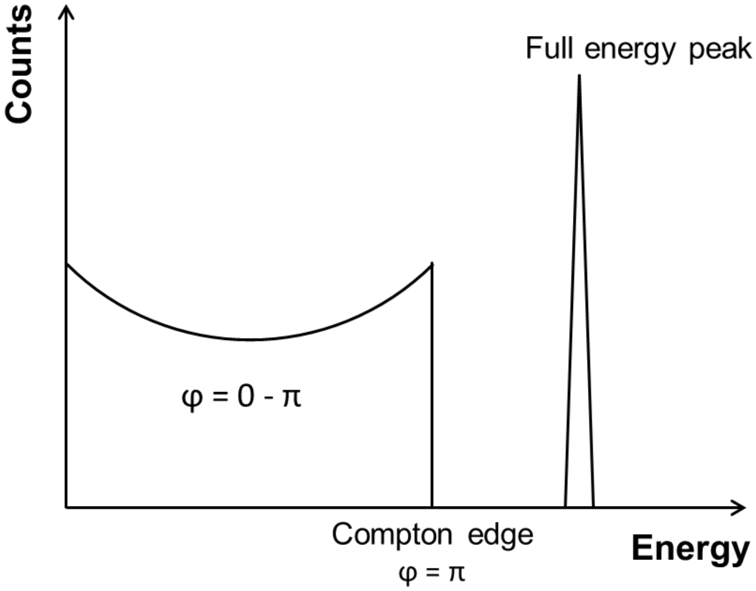

Figure 2-6 A typical energy distribution for photoelectrons involved in interactions with the incident 511 keV photons.

As an electron goes through the scintillator, it loses energy and excites other electrons, and then the excited electrons decay back to the ground state and emit light. The light is emitted isotropically, and the intensity is proportional to the energy of the electron that strikes the scintillator [31]. A scintillation detector consists of a scintillator optically coupled to a photomultiplier tube (PMT), which then generates an electrical signal in response to light incident upon its surface [31][32]. PMT absorbs the light emitted by the scintillator and re-emit electrons via the photoelectric effect. These detectors can produce an amplified current as much as 100 million times of the intensity of incident light, and produce a pulse of electrical current which can then be analyzed for information about the original light current that originally strike the scintillator.

The energy distribution is blurred by the limited energy resolution of the detector. In sufficiently large detectors, most photons can deposit all of their energy in the crystal and be registered in full energy peak, while in small size detectors only a portion of photons can undergo several Compton scattering processes prior to detection. The photons may escape before depositing all energy and give a continuous distribution lower within the full energy peak. There can also be some events with energy greater than the full energy peak because two or more photon interactions occur too close together to be resolved as separate events. So the actual energy distribution is smoother and wider [33].

Each 511 keV photon detected by a scintillation detector will ultimately generate a single electrical pulse by the PMT. A timing signal is done by passing the electrical pulse through a constant fraction discriminator (CFD), which generates a digital pulse if the pulse signal reaches a certain fraction of the peak pulse height. The digital pulse can then be used in the coincidence circuitry. Usually there is an upper energy-level discriminator (ULD), and a lower energy-level discriminator (LLD) which are used to reject electrical pulses out of a particular range [34]. The ULD is used to reject some events where more than one photon strikes on the detector within system time resolution. The LLD can be used for removing scattered annihilation photons since they have lower energy than those which are unscattered. However not all scatter photons can be removed by LLD because many of them have energy very close to 511 keV and the system energy resolution is not sufficient enough to distinguish them from unscattered photons. On the other hand, the majority of unscattered photons undergoes Compton process with the scintillation crystals and loses their energy within the crystal; thus choosing high LLD value will cause losing a significant part of true events. So there is a trade-off between scatter photons rejection and sensitivity to true events [34].

There are many criteria for choosing scintillation materials, such as high density and fast responding time. As discussed above, the proportion of events registered in the full energy peak increases with increasing detector size, which makes it possible to remove most events arising from photons scattered within the object by using a higher LLD in a detector system with sufficiently fine energy resolution. However, the spatial resolution of the system decreases with increasing detector size. The number of events registered in the full energy peak can also be increased by increasing the proportion of photons involved interactions of photoelectric absorption, and this can be achieved by choosing scintillator materials with a large value of effective atomic number Z (effective Z) [29]. Usually higher density materials have heavier ions that significantly increase the stopping power. High density materials with high stopping power reduces the size needed for stopping high energy γ-photons, therefore enables the ability of building more compact detector; for lower energy γ-rays, the range of Compton scattered photons will significantly decrease in high density materials. This results in better segmentation of higher proportion of photons in full peak energy and leads to better spatial resolution. PET detectors have to work at high count rates for millions of events, so high responding speed is needed for sufficient time resolution. Accordingly the scintillator decay time should be short since precision of time measurement with a scintillation detector is proportional to $\sqrt{\tau}$ [35].

Several other properties are also demanded for a good detector scintillator: high efficiency of converting the incident gamma photons into scintillation photons, transparency to its own scintillation light spectrum, an index of refraction close to that of glass that allow optimum optical coupling between the scintillator and PMT window, good linear attenuation over a wide range of energy [29][31][32]. And obviously the scintillator should be sturdy and easy to manufacture.

Table 2-1 Properties of scintillators material useful at 511 keV

Properties	ρ (g/ cm^3)	Decay time (ns)	Photons yield (per keV)	Index of refraction	Ration between photoelectric and Compton
NaI(Tl)	3.67	230	37.9	1.85	0.22
BGO	7.13	300	8.22	2.15	0.78
LSO: Ce	7.40	47	25.4	1.82	0.52
GSO: Ce	6.71	56	9.00	1.85	0.35
BaF_2	4.89	0.8†, 630‡	1.37†, 9.59‡	1.56	0.24

†, ‡: slow and fast components.

The properties of some important scintillation crystals are shown in Table 2-1 [32][36][37][38]. NaI has been widely used in SPECT and also used to a lesser extent in PET. The scintillation crystal widely used in clinical PET are bismuth germanate oxide

(BGO), gadolinium oxyorthosilicate (GSO) or cerium-doped lutetium oxyorthosilicate (LSO) [39].

2.3.2 Detector Design

There are several variations to decode the detector signals. For example, a 2D pixel related array of scintillation crystals are coupled to four single channel PMTs via a light guide to form the block detector [26] (Figure 2-7) is one major method of PET scanners [40].

When a photon incident is on one of the crystal elements, it will create a unique scintillation light signal that is shared by all four PMTs. Location of the event crystal element can be obtained from the individual PMT outputs [41]:

$$x = \frac{A+B}{A+B+C+D} \tag{2-8}$$

$$y = \frac{A+C}{A+B+C+D} \tag{2-9}$$

where *A*-*D* are fraction of light detected by each PMT.

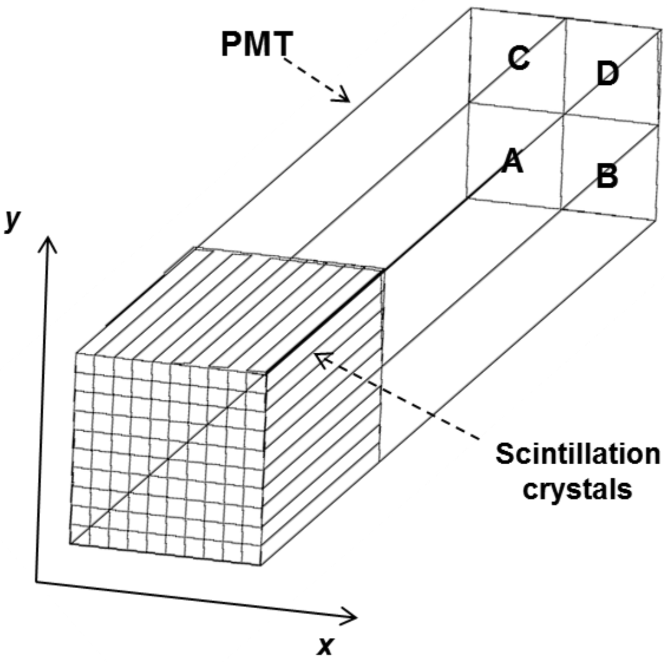

Figure 2-7 Schematic figure of block detector.

The positioning algorithm is subject to statistical fluctuations in the signals detected by the PMTs, which brings spatial distortion. The block detector provides a very cost effective method to ultimate intrinsic spatial resolution by reducing the number of photodetectors and associated electronics.

The other major approach to constructing a PET detector system is the continuous gamma camera [42]: a 2D array of PMTs be coupled to a single large area planar scintillation crystal. Since the spatial resolution decreases as the depth of scintillator goes up, high scintillation light output is required to achieve acceptable spatial resolution with large area planar detectors, so NaI is usually the choice in such systems.

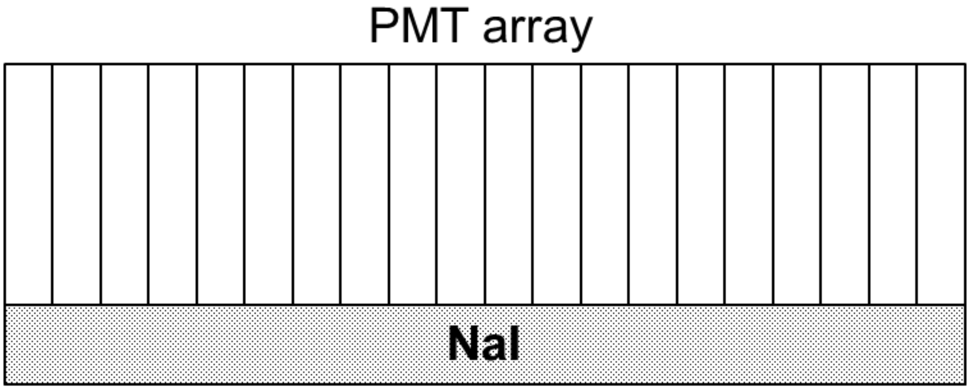

Figure 2-8 Schematic figure of continuous gamma camera.

Unlike the block detector, the location of the event is determined by analyzing the distribution of scintillation light among the PMT matrix in this continuous gamma camera detector [42]. The location information provided by this design is continuous, and then sampling can be done on the continuous location information based on different criteria. This positioning algorithm needs to take special efforts to allow detection of multiple events happening in different places on the same planar scintillator, otherwise the detector dead time (time interval required for properly processing one event after another) becomes a major problem. Also, due to the shape of large area scintillation crystal, significant dead space occurs on the edges of detectors and gaps between detectors [29].

There are also other scintillation detector configurations such as position-sensitive and multi-channel PMT, depth-encoding detectors, avalanche photodiodes, other gamma ray detectors like multi-wire proportional chambers (MWPCs), or direct detection using semiconductor materials [26]. However, due to different limitations, they are not as widely used in practice like the two major designs talked above.

2.3.3 PET Scanner Camera Configuration

Several pairs of block detectors or only one pair of large area planar detector would not make a PET system. The most common configuration of PET scanners is placing adjacent rings of block detectors around the object bed [26][29]. The plane of the detector ring is often referred in terms transverse or transaxial, while the directions perpendicular to this plane (along the object bed) is referred in term axial. It is also common to put less number of planar detectors in a polygonal geometry [26][29]. Both geometries will allow full coverage of the entire cross-section of the object and detection of many LORs with moving detectors, so they are very useful for rapid imaging of tracer dynamic distribution or short half-life radionuclide labeled tracers.

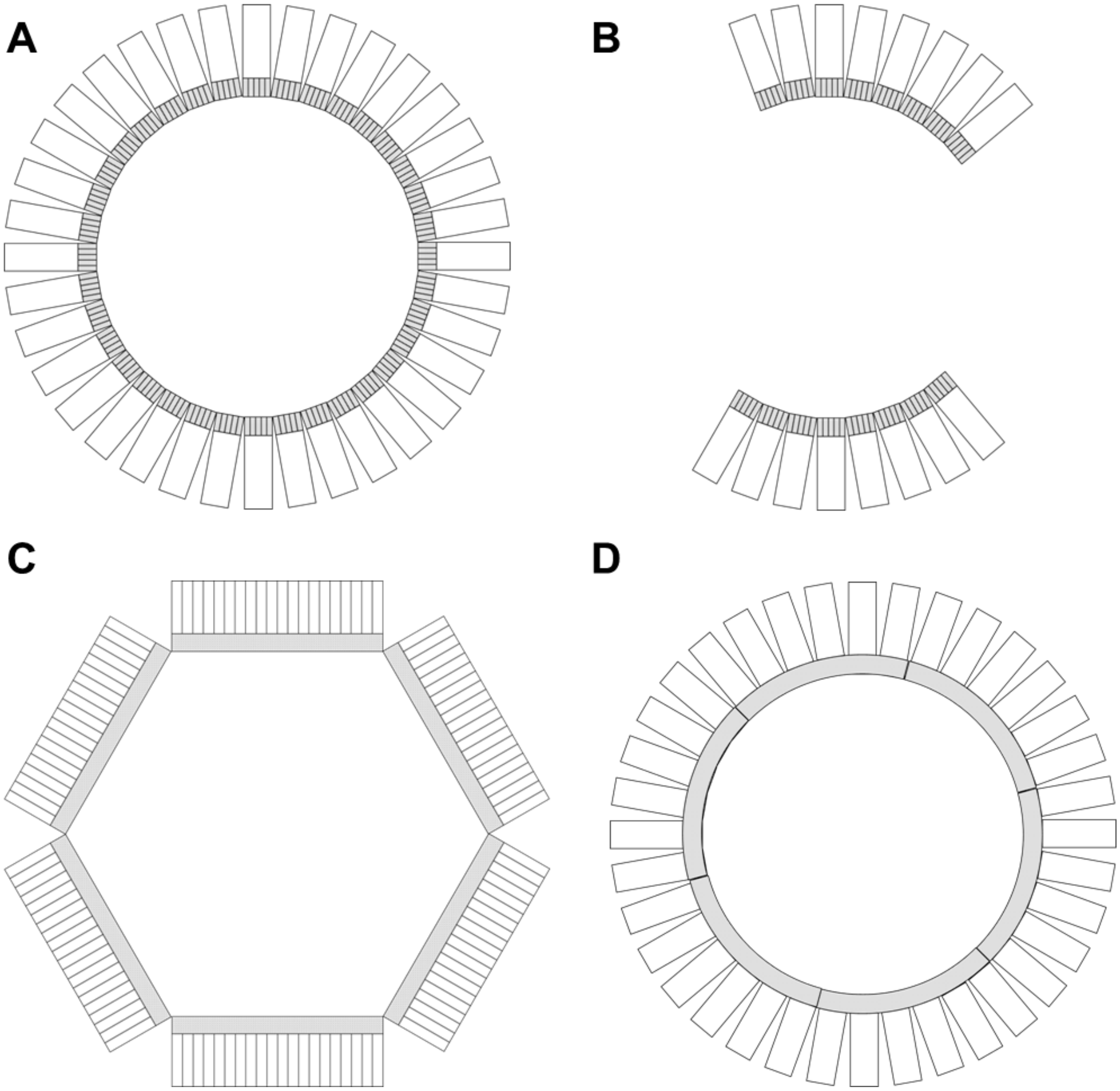

Figure 2-9 PET scanner configurations. (A) discrete design in a ring geometry; (B) discrete design rotation; (C) continuous design in a polygonal geometry; (D) continuous design in a ring geometry [26][29].

In PET system for static imaging with a long half-life radiolabeled tracers, a pair of opposing partial ring of detectors or large area planar detectors may be used to lower cost. This configuration requires rotating detectors around object to acquire sufficient data to reconstruct a tomographic image [26][29].

2.4 Data Acquisition for PET

In most of the first generation multiring PET systems, axial collimators or septa were placed in between adjacent rings of detectors. The septa absorb photons with large incident angle, so only those photons that are emitted within a small azimuthal angle can be detected and registered. Thus, the coincidences were only detected and recorded in the direct or cross planes, where direct plane is defined as the coincidences detected by the detectors on the same ring and cross plane is define as the coincidences detected by detectors on two adjacent rings (Figure 2-10) [29]. This design is commonly referred as two-dimensional data acquisition.

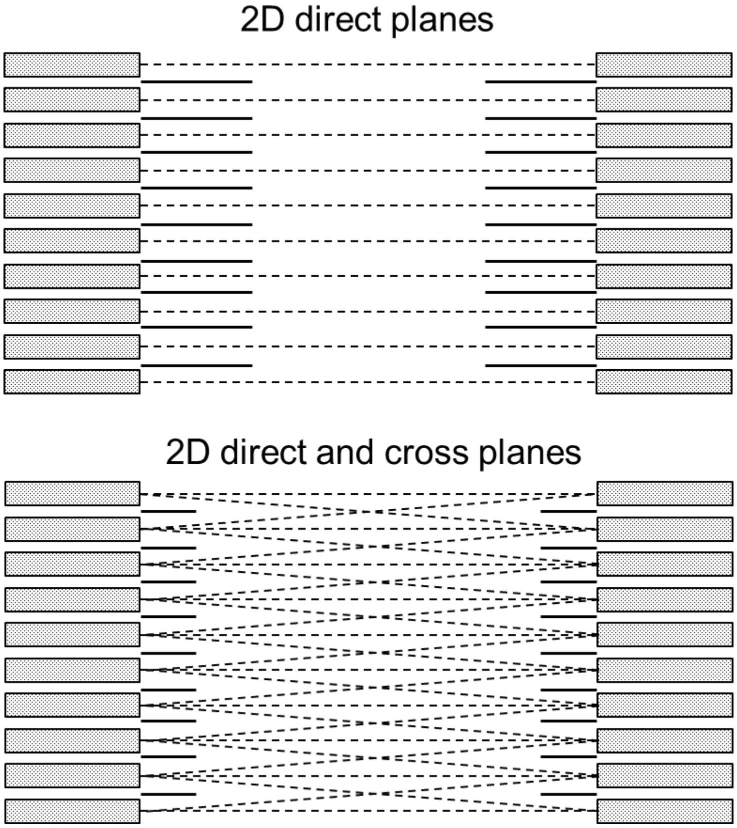

Figure 2-10 2D data acquisition for PET.

The septa reduces the single-channel counting rate by rejecting large angle photons that have a large possibility of being scattered within object body, therefore not only the scattered coincidences but also the random coincidences can be efficiently removed, and dead time can be minimized. In the cross planes, data are obtained from two different LORs, so they roughly have twice the sensitivity (twice the counting rates) than the positions in direct planes. However, the efficiency is low because the septa absorbs the annihilation photons on oblique LORs from many potentially valid coincidence events [29][43].

Newer PET systems remove septa in between adjacent rings, and the data is collected from all possible LORs. Because the coincidence planes are not only transaxial planes, this acquisition mode is referred as three-dimensional acquisition. The sensitivity of PET system can get dramatic improvement by defining addition coincidence planes. Typically 3-D acquisition leads to a fourfold to eightfold higher sensitivity compared to 2-D acquisition. In 3-D acquisition, the sensitivity profile along the axial direction is a triangular shape function with a peak in the middle of the FOV, so it is important to place object near center of FOV. The sensitivity on the edge on FOV is equivalent to 2-D acquisition.

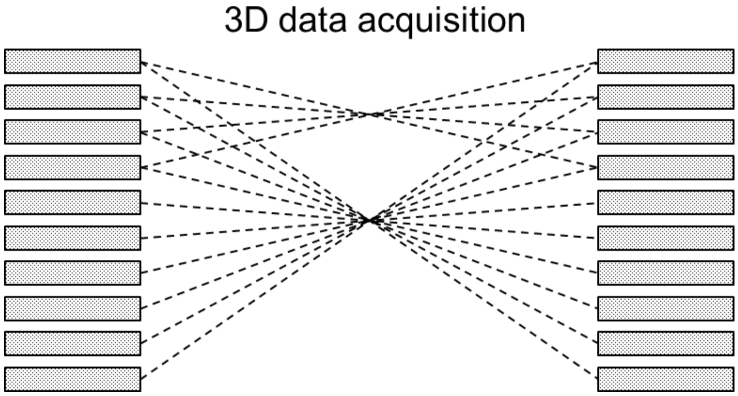

Figure 2-11 3D data acquisition for PET. The highest sensitivity is in the middle of the FOV.

The 3-D acquisition can be used to reduce imaging time for its higher sensitivity, and also reduce the injection dose of radioactivity. While 3-D acquisition provides overall higher sensitivity, the number of scattered coincidences and random coincidences is increased. Noise due to subtraction of random and scattered coincidence raises new problems when large amount activity is presented in the FOV. Also, there is a loss of spatial resolution along the axial direction due to the superposition of data from different positions [29][43]. Despite this, for the greatly improved sensitivity, 3-D acquisition mode is generally used on current commercially available PET scanners.

The basic data acquisition protocol is the collection of a single static frame over a period. The radioactive concentration represents the average distribution during the scan time. In some studies, it is necessary to follow the dynamic changes in radioactive concentration distribution to yield more information of interest about the dynamics of tracer delivery, accumulation and clearance in tissue. PET scanners with full cross-section coverage designs can simultaneously acquire data from all angles without detector motion, and have the ability to do dynamic studies. The scan usually starts as the radioactive tracer is being injected into object body and lasts for a number of time frames.

2.5 Data Correction

To produce a tomographic image which can reflect the true activity concentration, a number of corrections need to be applied to make sure the intensity of reconstructed image is proportional to the true activity in the corresponding area in the object.

2.5.1 Normalization

Fourier-based reconstruction method assumes all LORs have the same efficiency. However, the sensitivity of each LOR is affected by geometrical variations, non-uniformities in individual detector elements and difference in detector electronics. The normalization corrects each LOR with a multiplication factor referred as normalization coefficients (NCs), to compensate for the non-uniformities.

The most straightforward method of determining the NCs is to perform a scan of an uniform activity plane source, positioned at a number of equally spaced projection angles. This process will directly give a complete set of relative variation in coincidence detection efficiencies between all the LORs in the system. To reduce dead time and pile-up effects, the uniform source activity should be low [44], and this results in it taking quite large amount of time to acquire sufficient counts per LOR for good statistical estimation (tens of hours).

The time consuming problem can be solved by using a component-based variance reduction method [45][46], in which the coincidence detection efficiency between a pair of detectors of interest is assumed to be the product of the detector efficiencies and geometric factor, which can be written as:

$$NC = \frac{1}{\varepsilon_i \times \varepsilon_j \times g_{ij}} \qquad \textbf{2-10}$$

Where ε_i and ε_j are the individual detector efficiencies of the detector pair and g_{ij} is the geometric factor between them. The individual detector efficiencies can be obtained by performing a scan of uniform activity circularly symmetric source placing in the center of FOV. For each detector, the sum of coincidences between the detector of interest and all its opposing detectors is directly proportional to the detector efficiency. The geometric factors for a particular PET system can be determined by solid angle projected by the activity source at the detector and distance between the source and the detector, and can be assumed to remain constant. This process provides an estimation of *NC*s with low statistical noise because the measurement is based on averaging over a large number of detectors. However, the component-based method depends on empirical geometrical factor that could introduce systematic errors. There is a trade-off when choosing from these two correction methods [47].

2.5.2 Attenuation Correction

As discussed in section 2.2.2, one or both annihilation photons could have undergone Compton scatter interaction before escaping from the object material, and this results in the removal or attenuation of primary photons of the LOR and the potential detection of scattered photons in different LORs.

Consider a point source located at depth x inside an object material of thickness L along the LOR with linear attenuation coefficient μ, the probability of both annihilation photons will escape from the object is [29]:

$$p = e^{-\mu x} \cdot e^{-\mu(L-x)} = e^{-\mu L} \qquad \textbf{2-11}$$

Note that the probability is independent of the location of point source and only depends on the object thickness along the LOR.

In phantom studies, the attenuation correction can be made by calculating based on the dimension. The phantoms object being imaged can be approximated with a geometrical shape such as a cylinder or ellipse, and the attenuation coefficient within the phantom is also assumed to be constant. Object thickness L along each LOR is determined for the calculation of equation 2-11.

The most accurate method is direct measurements [29]. According to equation 2-11, if the point source is placed along the LOR outside the object, the activity measured by the detectors should be the same as the source inside the object. Thus, the attenuation factors can be obtained by performing two scans with or without an object in the FOV, and a rod source along the axial direction will rotate around the FOV [48]. First, the reference blank scan is measured with no object in the scanner, in which the blank data will be collected. Just before the injection of radioactive tracer, a transmission scan is acquired for the measured activity with the object inside the scanner. The attenuation factors along each LOR [49] are given by taking the ratio between the transmission scan and blank scan.

2.5.3 Scatter Correction

As discussed in section 2.2.2, scatter coincidence leads to many mispositioned events which change slowly with position and could reduce contrast and cause the isotope concentrations to be overestimated. The correction for scatter coincidence is difficult because it is impossible to distinguish the scatter events inside the object from the scatter events in the detector crystals on the bias of energy pulse height. Also, the scintillation crystal used in PET systems, mostly BGO detectors, have an energy resolution of 20% to 25% [50], which makes it hard to separate high energy scatter coincidence from true coincidence. Note that scatter and attenuation are the same physics phenomenon, when one annihilation photon undergoes the Compton scattering interaction with the object material, it gets attenuated; if the photon is barely absorbed by the object and reaches the detector on another LOR, it becomes a scatter event. For this reason, scatter correction should be performed before attenuation correction.

There are two main scatter correction methods currently being used in PET systems. First method uses the attenuation map obtained from the transmission scan and the uncorrected emission data [51][52]. Since both attenuation and scatter coincidence come from Compton scatter, it is possible derive the distribution of scatter photons falling in each projection profile from these two images and a model of the scanner, by using the Klein-Nishina formula [53]:

$$\frac{d\sigma}{d\Omega} = \alpha^2 r_c^{\,2} P(E_\gamma,\theta)^2 \left[P(E_\gamma,\theta) + P(E_\gamma,\theta)^{-1} - 1 + \cos^2\theta \right] / 2 \tag{2-12}$$

where α is the fine-structure constant, θ is the scattering angle, r_c is the reduced Compton wavelength of the electron, and $P(E_\gamma, \theta)$ is the ratio of photon energy after and before Compton scattering [52].

Then this estimated distribution can be subtracted from the profiles and reconstruction. This method gives very accurate result when all the volume contains radioactivity is within the FOV of the PET system. Problems will arise if there is a volume containing high radioactivity lying outside the FOV [29]. Also repeatedly creating projection profiles increases the calculation intensity.

The other method is fitting a Gaussian projection profile to the scatter distribution on the edge of each projection that requires the examination of the projection profiles immediately outside the FOV [54][55]. Since the scatter coincidence creates a low-frequency background, data on the edge of projection profiles can be extrapolated using smooth function over the entire area. The fitted scatter distribution is subtracted from the projection profiles which can then use for reconstruction. This method works fast and effective when the scatter situation is simple, and the object has a volume containing activity both inside and outside the FOV. If there is nothing outside, this method may cause significant error.

2.5.4 Random Correction

Random coincidence creates an approximately uniform background across the FOV of system, reduces the image contrast and can cause significant artifacts; thus it is necessary to remove random coincidence from the prompt coincidence to obtain quantitative PET image data. As discussed in section 2.2.2, the rate of random coincidence R_{ij} can be calculated for each LOR [56], which can be then subtracted. To accomplish this method, the single counting rate of each detector element and the coincidence window must be accurately known.

Another common method for estimating the random rate is delayed coincidence window method [29]. In this method, the timing signal from one of the two detectors is delayed by a time significantly greater than coincidence timing window. Therefore, no true coincidence will be recorded in the delayed window, so the coincidences found in this delayed window can only come from random coincidence. This estimated number from the delayed window can be subtracted from the prompts coincidences on-line. This method is free of systematic error because the delayed window is measured in the same electronic circuit used for the prompt coincidences. However the subtraction of two independent measurements leads to increased statistical uncertainty.

2.5.5 Dead Time Correction

Ideally the rate of the prompt coincidence should be directly proportional to the activity in the FOV. However in radiation detectors, there will be losses due to dead time at high counting rates, and the radioactive activity concentration could be significant underestimated if not corrected for dead time. The common method to do dead time correction is fitting the detector response function to paralyzable or nonparalyzable [57][58] dead time model.

Paralyzable model:

$$R_{measurement} = R_{true} \times \exp\left(-R_{true}\tau\right) \qquad \textbf{2-13}$$

Nonparalyzable model:

$$R_{measurement} = \frac{R_{true}}{1 + R_{true}\tau} \qquad \textbf{2-14}$$

where $R_{measurement}$ and R_{true} are the rate of measured coincidence and true coincidence, and τ is the dead time constant, which is usually the integration time of detectors and response time of coincidence circuit. Therefore, the dead time could be reduced by using faster scintillator and faster circuit.

3 Tracer Kinetic Modeling

3.1 Limited System Resolution

Ideally, after all corrections discussed above being performed to the PET data prior to the reconstruction of the image, the activity concentration should be proportional to the absolute activity in the volume of interest (VOI), which can then be calibrated to yield the true activity information. Due to limited system resolution, quantification of PET data is subject to partial volume (PV) and spillover effects (SP) which may cause overestimation or underestimation of activity concentration, depending on the distribution of activity in the VOI.

The design of scanner geometry, the properties of detectors and coincidence circuit will together contribute to the final resolution. The factors that determine system spatial resolution can be divided into two main components: geometric and physical. The final system resolution is the convolution of all the factors affecting resolution response function including both geometric and physical components.

3.1.1 Geometric Component

The geometric component is the best possible resolution that can be achieved for a particular scanner design using ideal detection elements [26].

For a detector pair of interests, the geometric resolution between the detector pairs can be described by coincidence response function. In discrete detector design system with detector size *w*, the coincidence response function is the possibility of the event is detected by detector pair of interest when the event is moving along the detector width.

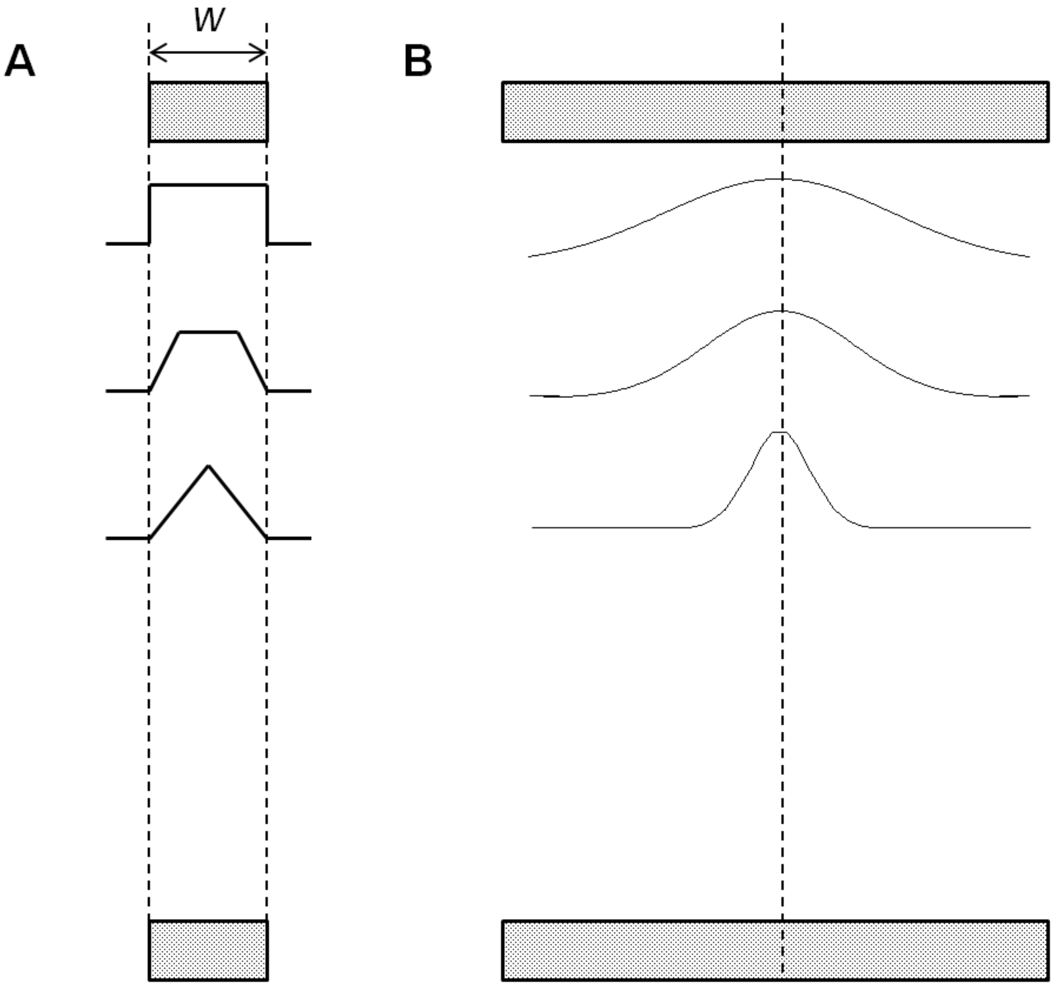

Figure 3-1 The change of response function when the event approaches the surface of the detector. (A) discrete design system; (B) continuous design system [26].

In the middle of the two detectors, the geometric resolution can be described by a triangular shaped coincidence response function with full width at half maximum

(FWHM) $= w/2$, and as the source is approaching either detector surface, the response function becomes trapezoidal and eventually becomes a square function on the surface of detector with FWHM equals *w*. In continuous design systems, the coincidence response function can be described by a Gaussian with FWHM equals $w/\sqrt{2}$. As approaching the detector surface, the coincidence response functions become broader and eventually become to have FWHM equals *w* [26]. Therefore, the detector size *w* is a limit factor for the intrinsic spatial resolution in both discrete and continuous design systems.

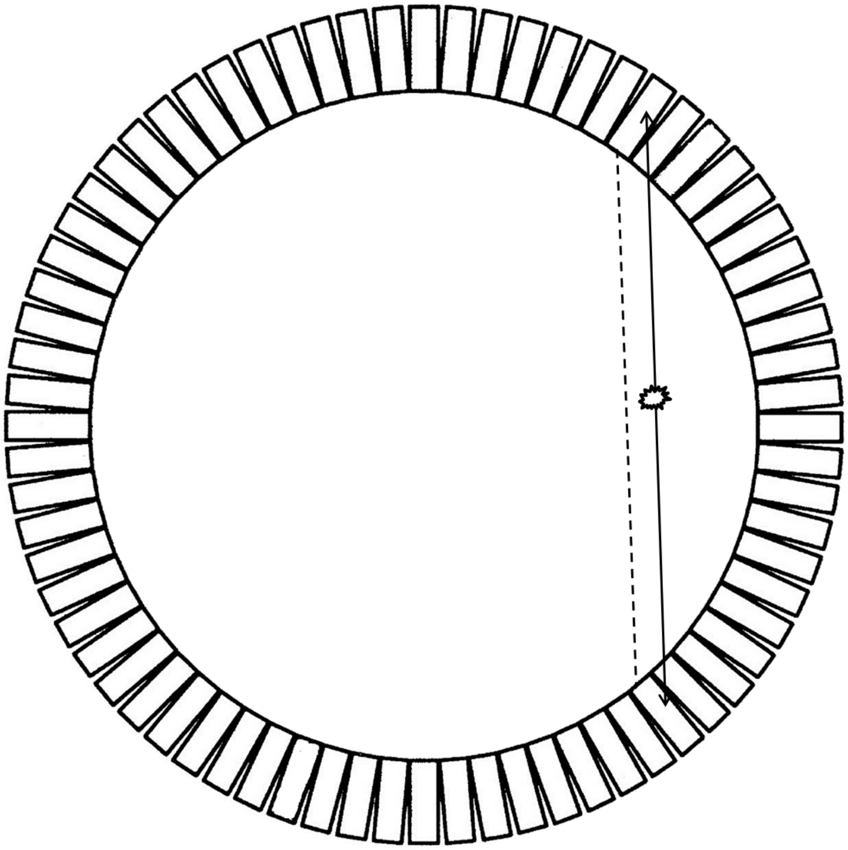

Figure 3-2 Depth of interaction effect**.**

Another geometric effect that degrades spatial resolution is called depth of interaction [26], caused by the thick scintillation crystals used for detectors. In the center of a ring design system, the annihilation photons will penetrate detectors perpendicular to the detector surface. When the source has a radial offset, the detector pair of interest is placed with an oblique angle to the line of response, and the annihilation photons may penetrate through the first detector interacted and then be detected by the adjacent detector.

The depth of interaction effect leads to mispositioning of events because the event is assigned to position on an LOR other than the true LOR. The other consequence is the coincidence response function becomes broader, because the detector is presenting a larger area to the LOR than the ideal perpendicular direction when the annihilation photons incident from an angle respect to the detector surface, which degrades the system spatial resolution. So the amount of decrease of resolution when the source is moving away from ring center depends on the scintillator size, absorption properties and geometry of the scintillation crystals. Also, PET systems using other scanner geometries like polygonal geometry suffer from the same problem. The center of FOV has the best system spatial resolution.

3.1.2 Physical Component

Based on the schematic of radiation detection, there are two physical effects lead to errors in determining the spatial information of coincidence event, which can degrade the system spatial resolution of PET systems.

The first effect is called positron range [59], and it is the distance from the site of positron emission to the site of annihilation. In 511 keV photons detection, scanner records the annihilation photons which define the line along the site of annihilation, not the decaying atom. Note here used the assumption that annihilation and photon emission happen in the same place. As the positrons travel through the object material, they give up their kinetic energy principally by Coulomb interactions with surrounding electrons. Since positrons have the same rest mass as electrons, the positrons may have undergone multiple direction-changing interactions and follow a tortuous path before eventually annihilating with electrons. Thus, there is an offset between where the photons are emitted and where the annihilation takes place blurring the final image.

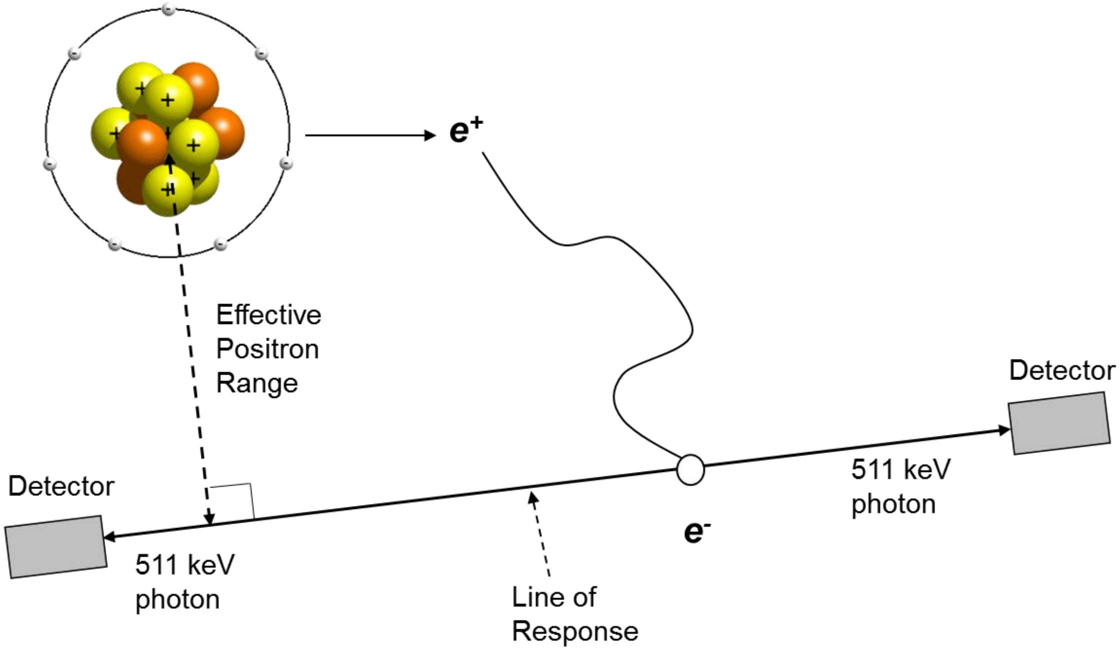

Figure 3-3 Positron range. It is radionuclide dependent: higher positron energy leads to larger positron range.

Table 3-1 Maximum positron energy and mean and maximum positron ranges of commonly used isotopes [38][60]

Isotope	Maximum positron energy (MeV)	Maximum positron range in water (mm)	Mean positron range in water (mm)
^{11}C	0.96	3.9	1.1
^{13}N	1.19	5.1	1.4
^{15}O	1.72	8.0	2.5
^{18}F	0.65	2.4	0.6
^{62}Cu	2.93	16.1	6.1
^{68}Ga	1.90	8.9	2.9
^{82}Rb	3.35	18.6	7.5

This effect is also radionuclide dependent. Different radionuclides emit positrons of different energy, and the positron range becomes larger as the maximum energy of the emitted positron goes higher, which makes the final image blurrier.

The second effect of photon noncollinearity [61] arises when the positron and electron are not completely at rest at the time they annihilate into two photons. From the conservation of system momentum, the annihilation photons are not emitted at exactly back to back, but with a distribution of angles around 180^0. Unlike positron range, photon noncollinearity is not radionuclide dependent. The distribution of emitted angles is roughly Gaussian in shape with a FWHM of 0.5^0 [29], so the degradation of the spatial resolution due to the noncollinearity is expressed as:

$$\Delta = 0.0022D \qquad \textbf{3-1}$$

where D is the diameter of the PET scanner. The effect is relatively small compared to the detector resolution limit *w* discussed in section 3.1.1, thus is not a significant problem.

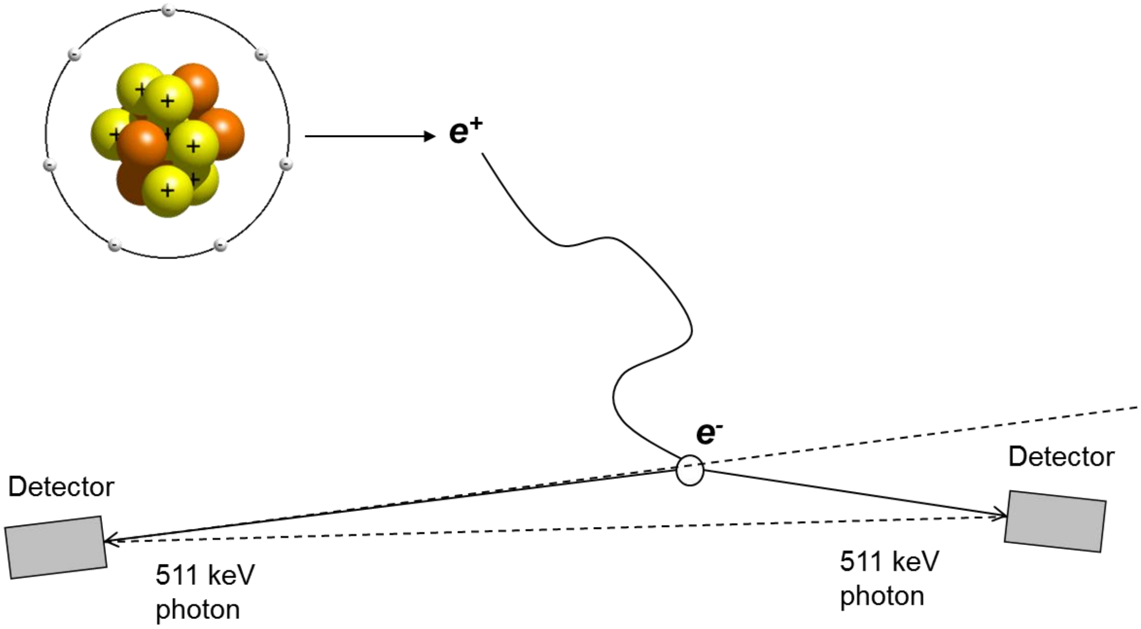

Figure 3-4 Photon noncollinearity: two gamma photons are not emitted back to back when the positron and electron are not completely at rest.

3.2 Partial Volume and Spillover Effect

Due to the limited system resolution, quantitative PET imaging suffers partial volume and spillover effects [38][62][63], which make it difficult to accurately determine the activity concentration in the VOIs or regions of interest (ROIs).

In the measurement of radioactive sources in the scanner, the intensity of the images reflects not only about the concentration but also the distribution in the measured volume and immediate adjacent volume. The annihilation events will be determined within a small region around their actual sites due to the schematic of radioactive detection. For objects that are small compared to the resolution volume of the PET scanner, the radionuclide's information is spread over a volume greater than the object. Although the total amount of measured activity stays the same, the measured radioactivity concentration should be lower than the true concentration. For the objects that are large compared to the resolution volume, the center radioactivity concentration could be accurately measured, while the edge of the objects appears to have lower than the actual concentration due to the spread over of radionuclides location information.

In a simulation work, a smoothing 10 mm filter has been applied to simulate a 10 mm resolution system [26]. The concentration of larger objects is accurately measured, although there is smearing on the edge. However, as the source becomes smaller, the measured concentration diminishes and only partial concentration can be recovered in the images.

The partial volume (PV) effect is characterized by recovery coefficient (RC):

$$RC = \frac{Measured\ peak\ activity\ concentration}{True\ activty\ concentration} \tag{3-2}$$

The *RC* is a function of object size and the resolution of PET system, which can be characterized by phantom study for a particular PET system. It is crucial to correct for partial volume effect to prevent from underestimation of activity concentration when the object size is comparable to the system resolution.

When the ROI or VOI is surrounded by tissue with radioactivity, the problem gets more complicated. It is necessary to do corrections for not only the partial volume effect, but also the cross contamination or activity spillover from the surrounding regions with radiotracer uptake into the region of interest. This is called spillover (SP) effect [62].

3.3 Tracer Kinetic Modeling

The spatial distribution of radioactive tracer in the object depends on the uptake, utilization and washout dynamics of the tracer inside body. The time-dependent radioactive concentration functions of tissue and blood yield information about the biological process of interest, especially the rate of change of tracer concentration usually directly reveals the rate of a specific metabolic process of interest. Therefore the radiopharmaceutical should be chosen wisely and the PET data should be analyzed carefully.

3.3.1 3-Compartment Model

Tracer kinetic modeling is commonly used for quantitative evaluation of dynamic PET data [64][65][66]. Most models in use are compartment models with first order of kinetic parameter indicating the exchange rate of radiotracer between compartments.

Following a general approach of a 3-compartment glucose transport model [67] for evaluating FDG metabolism in the heart (Figure 3-5), the differential equations for FDG transport can be written as:

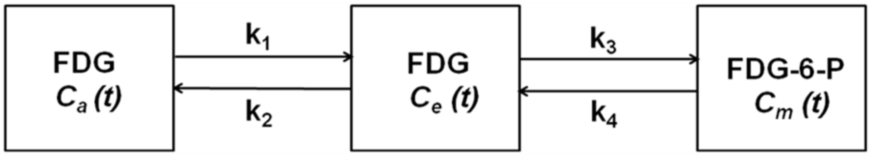

Figure 3-5 The schematic block diagram of 3-compartment FDG model. It indicates the rate constants, K1-k4, between the 3 compartments of the FDG kinetic model.

$$\frac{dC_e(t)}{dt} = k_1 C_a(t) - (k_2 + k_3) C_e(t) + k_4 C_m(t) \qquad \textbf{3-3}$$

$$\frac{dC_m(t)}{dt} = k_3 C_e(t) - k_4 C_m(t) \qquad \textbf{3-4}$$

The three compartments shown in Figure 3-5 can be described as equation 3-3 and 3-4: $C_a(t)$ is the FDG concentration in the vascular space, $C_e(t)$ is the concentration of FDG in the interstitial and cellular spaces and $C_m(t)$ is the FDG concentration within the cell of the phosphorylated FDG-6-Phosphate. k_1 and k_2 are the forward and reverse rate constants respectively between the first two compartments. k_3 and k_4 are the rates of phosphorylation and de-phosphorylation between compartments 2 and 3. $C_e(t)$ and $C_m(t)$ can be solved in terms of $C_a(t)$ and the rate constants, k_1-k_4:

Rewriting equation 3-4:

$$k_3 C_e(t) = \frac{dC_m(t)}{dt} + k_4 C_m(t) \qquad \textbf{3-5}$$

$$k_3 \frac{dC_e(t)}{dt} = \frac{d^2C_m(t)}{dt^2} + k_4 \frac{dC_m(t)}{dt}$$
$$= k_3 k_1 C_a(t) - (k_2 + k_3)\left(\frac{dC_m(t)}{dt} + k_4 C_m(t)\right) + k_3 k_4 C_m(t) \qquad \textbf{3-6}$$

Taking derivative of equation 3-6 and reorganizing gives:

$$\frac{d^2C_m(t)}{dt^2} + (k_2 + k_3 + k_4)\frac{dC_m(t)}{dt} + k_2 k_4 C_m(t) - k_1 k_3 C_a(t) = 0 \qquad \textbf{3-7}$$

Consider the characteristic equation of 3-7:

$$x^2 + (k_2 + k_3 + k_4)x + k_2 k_4 = 0 \qquad \textbf{3-8}$$

has two solutions $-\alpha_1$, $-\alpha_2$, where

$$\alpha_{2,1} = \frac{1}{2}\left[k_2 + k_3 + k_4 \pm \sqrt{(k_2 + k_3 + k_4)^2 - 4k_2 k_4}\right] \qquad \textbf{3-9}$$

and the solutions for characteristic equation are $y_1 = e^{-\alpha_1 t}$ and $y_2 = e^{-\alpha_2 t}$

Use Green's kernel: $\frac{e^{-\alpha_1 t} - e^{-\alpha_2 t}}{\alpha_2 - \alpha_1}$ and $f(t) = k_1 k_2 C_a(t)$

$$C_m(t) = \int_0^t k(t-\tau) f(\tau) d\tau = \frac{k_1 k_3}{\alpha_2 - \alpha_1}\left(e^{-\alpha_1 t} - e^{-\alpha_2 t}\right) \otimes C_a(t) \qquad \textbf{3-10}$$

$$C_t = C_e + C_m = \frac{k_1}{\alpha_2 - \alpha_1} \times [(k_3 + k_4 - \alpha_1)e^{-\alpha_1 t} + (\alpha_2 - k_3 - k_4)e^{-\alpha_2 t}] \otimes C_a(t) \qquad \textbf{3-11}$$

k_i is the net myocardium tissue concentration. Assuming the rate of de-phosphorylation k_4 =0 in equilibrium status, which is commonly true in this case, the net myocardial FDG influx constant k_i [68], can be written as:

$$k_i = k_1 k_3 / (k_2 + k_3) \tag{3-12}$$

3.3.2 Correction for Partial Volume and Spillover Effects

In a situation where there is no PV or SP, when a region of interest is drawn within the cavity of the left ventricle, the image derived input function (IDIF) would equal the whole-blood time activity curve $C_a(t)$. However, due to SP and PV effects, the model equation for an image-derived time activity curve from the blood pool can be written in terms of fraction of the tissue concentration in the blood compartment and partial recovery of radioactivity concentration from the blood as:

$$m_{IDIF,i} = \frac{\int_{t_b^i}^{t_e^i} [S_{mb}(C_e(t) + C_m(t)) + r_b C_a] dt}{t_e^i - t_b^i} \tag{3-13}$$

and similarly for the myocardium tissue, one can write the model equation as:

$$m_{myo,i} = \frac{\int_{t_b^i}^{t_e^i} [r_m(C_e(t) + C_m(t)) + S_{bm} C_a] dt}{t_e^i - t_b^i} \tag{3-14}$$

r_m, r_b, are the recovery coefficients (accounting for PV effect) for the myocardium and blood pool respectively. S_{bm}, S_{mb} are the SP coefficients from the blood pool to the myocardium and vice versa respectively. t_{bi} and t_{ei} are the beginning and end times respectively for frame i in a dynamic PET scan. Equation 3-13 and 3-14 represent the average radioactivity during the time of frame i, which matches the way with image derived raw data. The model equation for the blood input function can be written for 3-compartment model as [69]:

$$C_a = \begin{cases} 0, if\ t < \tau \\ \left[A_1(t-\tau) - A_2 - A_3\right] e^{L_1(t-\tau)} + A_2 e^{L_2(t-\tau)} + A_3 e^{L_3(t-\tau)}, otherwise \end{cases} \tag{3-15}$$

where each of the terms determines the amplitude, shape and wash-out of the tracer over time. The model equations can be fitted to the blood (PET_{IDIF}) and myocardium (PET_{myo}) time activity curves (TACs) obtained from OSEM-MAP cardiac and respiratory gated PET images with attenuation correction, as indicated below:

$$O(p) = \sum_{1}^{n} [(m_{IDIF} - PET_{IDIF})^2 + (m_{myo} - PET_{myo})^2] \tag{3-16}$$

Minimization of equation 3-16 results in simultaneous estimation of the blood input function, and compartment model parameters k_1-k_4 and hence k_i along with the SP and PV coefficients (S_{mb}, r_b, S_{bm}, r_m).

4 Optimization of a Model Corrected Blood Input Function from Dynamic FDG-PET Images of Small Animal Heart *in vivo*

4.1 Introduction

Tracer kinetic modeling is commonly used for quantitative evaluation of dynamic PET data. The estimation of kinetic rate constants requires an accurate knowledge of the blood input function. However, quantitation of dynamic PET data of the mouse heart *in vivo* is challenging due to the small size of the heart and the limited system resolution of the PET scanner [70][71].As a result, the image-derived blood input function (IDIF), which is the same as blood pool (BP) time activity curve (TAC), is susceptible to partial volume (PV) effect and spill-over (SP) radioactivity [72] from the surrounding myocardium tissue and vice versa. Also, cardiac and respiratory motion can cause further cross contamination between BP and myocardium by blurring the images. Although invasive arterial blood sampling is the gold standard for measuring the blood input function [73], it requires extensive animal handling. Hybrid imaging method is another technique which is a combination of the image-derived approach at the early time points and blood sampling at the late time points in a dynamic PET scan [74]. Factor Analysis is an image-derived approach which lacks the ability to account for the significant SP into the blood from the surrounding left ventricle (LV) and the right ventricle (RV) at the early time points [75]. Earlier work by El Fakhri et al [76] also accounted for blood volume contribution from both the RV and LV into the tissue, but did not account for SP contamination from the tissue to the blood in a factor analysis approach to measure myocardial perfusion using ^{82}Rb PET in a 2-compartment kinetic model.

The effect of iterative OSEM-MAP reconstruction algorithm on IDIF has been reported by Stout et al [77] and more recently by Shogi et al [78]. The authors reported significant SP contamination from the tissue to the blood especially at the late time points, in spite of using iterative algorithm. In an earlier work from our laboratory, we established the significance of cardiac gating and OSEM-MAP reconstruction algorithm in reducing SP contamination in IDIF [79]. Recent work by Fang et al concluded that a compartment model corrected blood input function when applied to IDIFs obtained from high-resolution images with less severe PV recovery and SP contamination, may result in an improved estimate of the downstream FDG influx constant [80]. The combined effect of resolution and model correction with correct bounds for PV recovery and SP contamination on the estimation of input function and FDG influx constant, has not been shown to-date. In this study, we optimized a compartment model which can simultaneously account for SP and PV effects for both BP and the myocardial tissue, compute kinetic rate parameters and generate model corrected blood input function (MCBIF) from OSEM-MAP cardiac and respiratory gated ^{18}F-FDG PET images of the mouse heart with attenuation correction *in vivo*, without the need for any invasive blood sampling. We validate our methodology by blood sampling and also measure the downstream rate of myocardial FDG uptake. We compare our results with the usual method of performing FBP reconstruction without gating [80].

4.2 Materials and Methods

All experiments were performed in compliance with the Guide for the Care and Use of Laboratory Animals, published by the National Institutes of Health and was conducted under protocols approved by the Institutional Animal Care and Use Committee at the University of Virginia.

4.2.1 Arterial and Venous Blood Sampling

Tracer kinetic modeling used in conjunction with positron emission tomography (PET) imaging is an excellent tool for the noninvasive quantification of physiological and molecular processes and their alterations due to disease. These kinetic models require two key measurements of tracer activity over time: tracer activity in the arterial blood (input function) and tracer activity in the organ or tissue of interest [72]. Direct blood sampling is considered the reference standard for obtaining the input function, however for small animal 18F-FDG studies, this procedure is challenging because of the small size of the blood vessels and the limited blood volume. Invasive surgery is required to insert the catheter into the femoral or carotid artery which is time-consuming, technically difficult, and is also challenging for the animal. In addition, the loss of blood through sampling may perturb the physiology and compromise the experimental outcome.

Blood input functions can be measured from PET images using methods that are not as well established as direct blood sampling. Using the left ventricular blood pool as the largest available vascular space, we can draw regions of interest on dynamic PET images to extract the blood input function. This technique offers a non-invasive way to estimate the blood input function and drastically simplifies the overall protocol. Because the LV is small compared to the scanner spatial resolution, we must take additional steps to correct for possible errors in the image-derived blood input function. We have taken a phantom based approach to correct for partial volume effects, or incomplete recovery of the total radioactivity in the LV blood pool and the myocardial wall due to their small size (~1 mm) comparable to the system resolution of the MicroPET scanner (1.32 mm FWHM in the center of the FOV) [71]. In order to replace invasive blood sampling with the non-invasive, imaging-based technique of determining the blood input function, we must directly compare the two techniques in living mice.

The surgical procedure for arterial blood sampling to validate the image-derived blood input function obtained from dynamic PET images was performed as follows: Prior to surgery, anesthesia was induced with 3% Isoflurane in Oxygen (0.5-0.8 L/ min) and maintained at 1.5% - 2.5% Isoflurane. Animals were carefully checked for pain response by toe and tail pinch prior to surgery and monitored for respiration and color throughout. Surgery was performed on a thermostatically controlled operating table maintained at 37-39 ^{o}C. Hair from the surgery area was removed and cleaned with alcohol (this was a non-survival surgery). An incision was made in the neck or the groin and the carotid or femoral artery exposed by blunt dissection. A catheter was formed from PE-50 tubing with the end stretched and placed in the carotid or femoral artery. The artery was tied off above the insertion site with 7-0 prolene and temporarily occluded distal to the insertion site using clamps or pressure from an untied ligature. The catheter was ligated in place with prolene in three places and all clamps removed. The incision was closed with prolene suture. Following the surgery the animal was placed in prone position in the

MicroPET scanner and a dynamic acquisition over 60 minutes initiated. Seventeen blood samples (< 30 μL each) were taken over the course of the scan by the following schedule: 3 blood samples were taken at 20, 40 and 60 seconds during tail-vein injection of FDG, then every minute up to 10 minutes and then 1 sample was taken every 10 minutes until the 60 minute mark. Blood draws are followed by flushing the catheter with a small volume of heparinized saline. Blood loss volume was replaced with an equal volume of sterile saline at the end of the first 10 min period. Each whole-blood sample is weighed and its FDG activity measured in a gamma counter (2480 Wizard, Perkin Elmer Inc.). Since arterial blood sampling was very challenging we resorted to venous blood samples from the tail-vein, at 43 and 56 minutes post FDG administration in n=6 mice, when the SP from the tissue to the blood is expected to be maximum [77]. Also, Fang et al [80] showed earlier that arterial blood is well approximated by venous blood at late time points.

4.2.2 Imaging Protocols

Following the protocol in [80], the animals were fasted overnight with only access to water. PET scans were performed between 9 a.m. and 5 p.m. on anesthetized animals. We used a similar imaging protocol as described in [79] except for using a different anesthesia and respiratory gating in addition to cardiac gating. Briefly, n=6 adult C57BL/6 male mice (9 to 10 weeks of age) obtained from Charles River, with ECG surface electrodes (Blue Sensor, Ambu Inc., Glen Burnie, MD) and a respiratory pillow attached to their limbs and chests respectively, were imaged using a MicroPET Focus-F120 scanner (Siemens, Inc.) under sevoflurane anesthesia [82]. Transmission scan using

^{57}Co point source was done for attenuation correction prior to FDG administration. 60 minute dynamic PET scan was performed under 2 to 2.5% sevoflurane anesthesia in oxygen, which was initiated few seconds before the administration of 29.6 MBq ^{18}F-FDG for 30 seconds via a tail-vein catheter to capture the initial time points. A small-animal gating and monitoring system (Small Animal Instruments, Inc., model 1025L for PET) was used for continuously monitoring heart rate, respiration, and core body temperature. Cardiac gate signals generated at the end-expiration phase of the respiratory cycle, using the small animal gating system, were used to trigger the PET scanner. The time stamped list mode PET data was then retrospectively arranged into 23 time bins and 3 cardiac phases per time bin [83]. The list mode data sorted into 23 time bins: frames x time in seconds (11 × 8 s, 1 × 12 s, 2 × 60 s, 1 × 180 s, and 8 × 400 s) [79][84][85]. And 3 cardiac gates was reconstructed using OSEM-MAP algorithm, and also into 23 time bins without gates using FBP algorithm [86]. An OSEM-MAP (FastMAP) version 2.4 was used for reconstruction and the parameters were 12 OSEM-3D subsets with 2 OSEM-3D iterations, 18 MAP iterations, span 3, ring difference 47 and image resolution 1.438 mm. The reconstructed image consisted of 95 slices with 128×128 pixels and an in-plane voxel resolution of 0.4 mm × 0.4 mm, corresponding to a zoom factor of 2.164 and slice thickness of 0.8 mm.

4.2.3 Recovery Coefficient (RC) Measurements

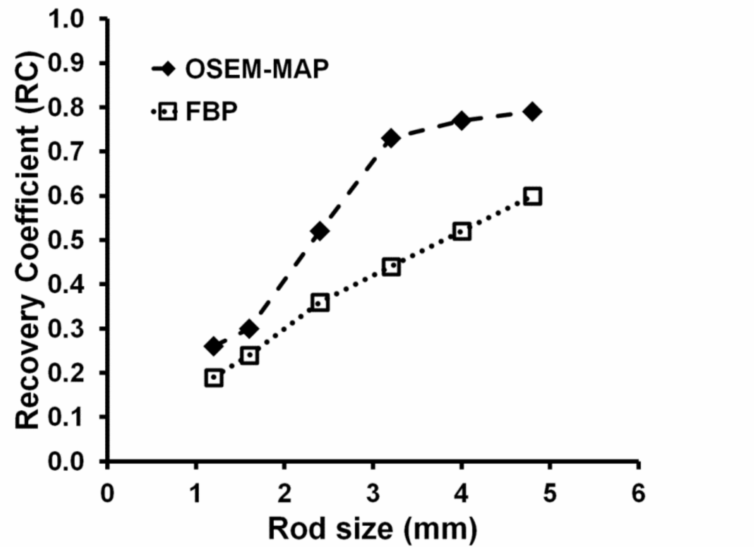

Figure 4-1 Plot of RC with different rod sizes using OSEM-MAP (dash line with diamonds) and FBP reconstruction algorithm (dotted line with open squares).

To characterize recovery coefficients for this particular small animal scanner MicroPET F120, a Jaszczak Micro Deluxe hot rod phantom scan (Data Spectrum Inc.) filled uniformly with about 14.9 MBq FDG was imaged in list mode format for 20 minutes. Co-57 scan was performed for attenuation correction. The list mode data corrected for attenuation was reconstructed with OSEM-MAP and FBP algorithms (Figure 4-1). The ratio of the measured average concentration to the known concentration determined the recovery coefficient (RC) for each of the rod sizes ranging from 1.2 mm to 4.8 mm. The initial guesses and bounds for the PV averaging coefficients (r_m, r_b) used in the kinetic model were derived from the RC plot. The dimensions of the myocardial wall (0.9±0.1 mm) and LV (3.3±0.2 mm) in mice were based on previous MRI measurements [87]. These dimensions are consistent with published work using ultrasound in mice of similar age and strain [88].

4.3 Data Analysis

Regions of interest (ROI) in the region corresponding to the left ventricle BP and the myocardium were drawn on short-axis slices in the last frame and the last gate of the dynamic image data and time activity curves (TAC) generated for the whole scan duration of 60 minutes. The blood pool ROIs were round shape of diameter approximately 1.6 mm located in the middle of the LV cavity, and the myocardium ROIs were donut shape of inner diameter ~ 3.2 mm and outer diameter ~ 5.6 mm drawn along the LV wall.

The initial guesses and bounds for all the parameters used in the optimization routine are shown in Table 4-1. Minimization of equation 3-12 results in simultaneous estimation of the blood input function, and compartment model parameters k_1-k_4 and hence k_i along with the SP and PV coefficients (S_{mb}, r_b, S_{bm}, r_m).

The general formalism described above is following [80] and [88], however the main difference lies in choosing correct PV bounds for the myocardium and the blood pool, based on the reconstruction algorithm Figure 4-1, in equation 3-16, as opposed to arbitrary bounds used in [80][89]. The difference also lies in using IDIF from high resolution gated images as opposed to the normal method of relying on IDIFs from FBP un-gated images.

Table 4-1 Initial guess values and bounds for parameters used in the optimization routine applied to OSEM-MAP gated images

Parameter	k_1 (1/min)	k_2 (1/min)	k_3 (1/min)	k_4 (1/min)	S_{mb}	r_b	r_m	S_{bm}
Initial value	0.01	0.01	0.001	0.001	0.5	0.75	0.3	0.5
Upper bound	1	1	1	0.001	1	0.9	0.4	1
Lower bound	0	0	0	0	0	0.6	0.15	0

Parameter	A_1 (MBq/min/mL)	A_2 (MBq/mL)	A_3 (MBq/mL)	L_1 (1/min)	L_2 (1/min)	L_3 (1/min)	τ (min)
Initial value	111	0.296	0.259	-27	-0.55	0.04	0.15
Upper bound	500	500	100	0	0	0	0.5
Lower bound	0	0	0	-200	-10	-10	0

The optimization was performed by minimizing the objective function 3-16 in the MATLAB programming environment using the function “fmincon”, which is based on an interior-reflective Newton method. The initial guesses and bounds for the PV averaging coefficients (r_m, r_b) are determined beforehand by performing phantom experiments [79]. We have kept the bounds for all the kinetic parameters (k_1-k_4) and SP factors (S_{bm}, S_{mb}) open between 0 and 1. As for the input function, one side of the bounds is determined by the distribution of the input function (A_1, A_2, $A_3 > 0$ and L_1, L_2, $L_3 < 0$) while the other side is wide open. Minimization of equation 3-16 results in simultaneous estimation of the blood input function equation 3-15, and compartment model parameters k_1-k_4 and hence k_i along with the SP and PV coefficients, without the need for any blood sampling.

4.4 Results

Figure 4-1 shows a plot of the RC obtained using OSEM-MAP and FBP reconstruction algorithms as a function of the rod size. The plot indicates that OSEM-MAP results in improved PV recovery as compared to FBP over the entire range. The initial guess values and the bounds used in the optimization routine for the two different algorithms were determined from this plot.

Representative results of comparison between TACs derived from dynamic gated PET images (Figure 4-2 E) (PET_{IDIF} and PET_{myo} TAC) and model corrected output time activity curves obtained ($Model_{blood}$ and $Model_{myo}$) of mouse left ventricle BP and myocardium respectively, are shown in Figure 4-2 E. Arterial blood samples collected over the whole scan duration for one mouse compared with the MCBIFs applied to the IDIFs obtained from OSEM-MAP gated image and from FBP un-gated image are shown in Figure 4-2 F. The figure indicates that, in this animal, MCBIF from OSEM-MAP gated image matches late time points better than FBP un-gated image.

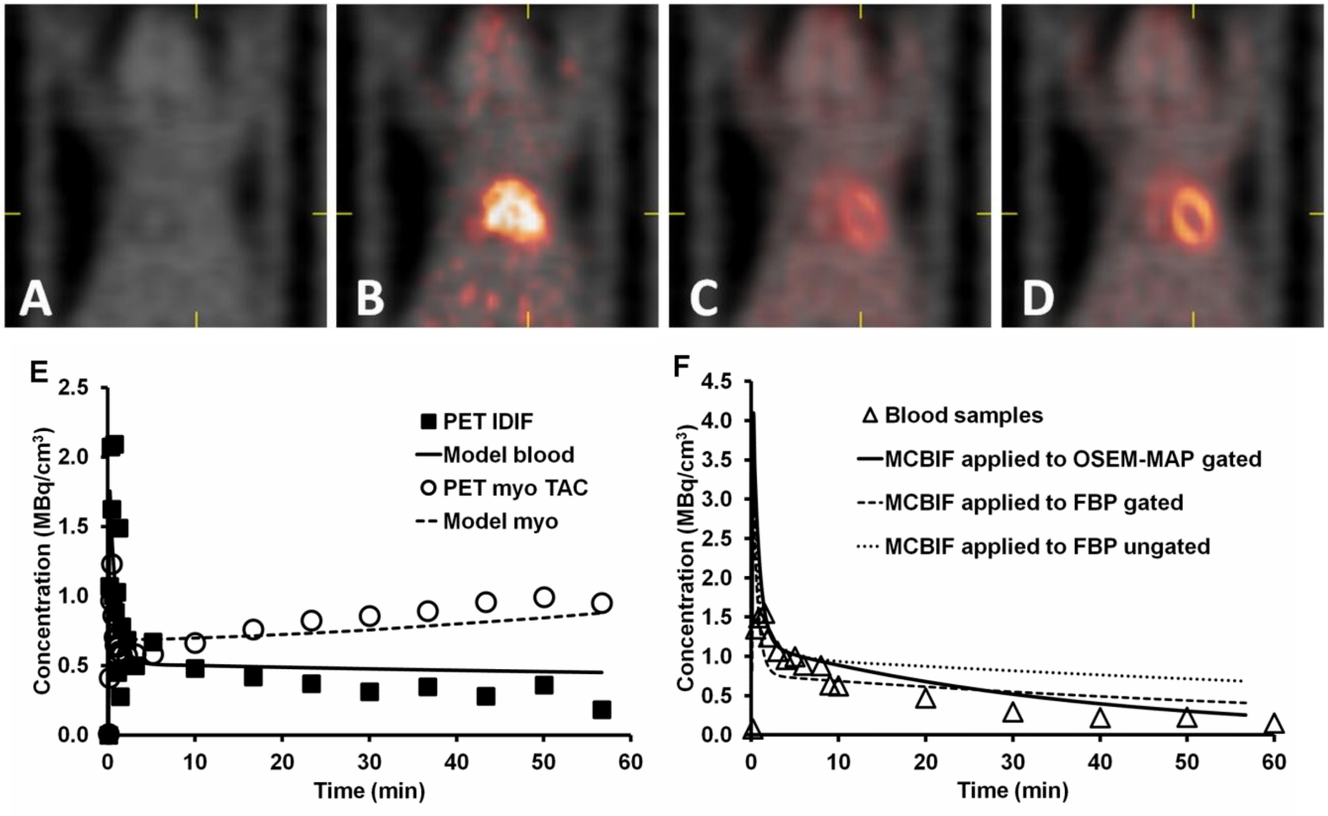

Figure 4-2 Select coronal dynamic end-diastolic PET images at 0, 0.5, 2 and 56 minutes fused with transmission images, and representative estimated results of mouse model correction. (A-D) respectively stands for pre, early time points and a late time point. (E) Representative image-derived time activity curves of BP (squares) and myocardium (open circles) obtained from OSEM-MAP cardiac and respiratory gated images shown above and model estimated BP (line) and myocardium (dash line) time activity curves are shown here. (F) MCBIF applied to the IDIF obtained from OSEM-MAP gated image (solid line) and FBP ungated image (dashed line), compared to the arterial blood samples (open triangles) obtained during the scan time of 60 minutes.

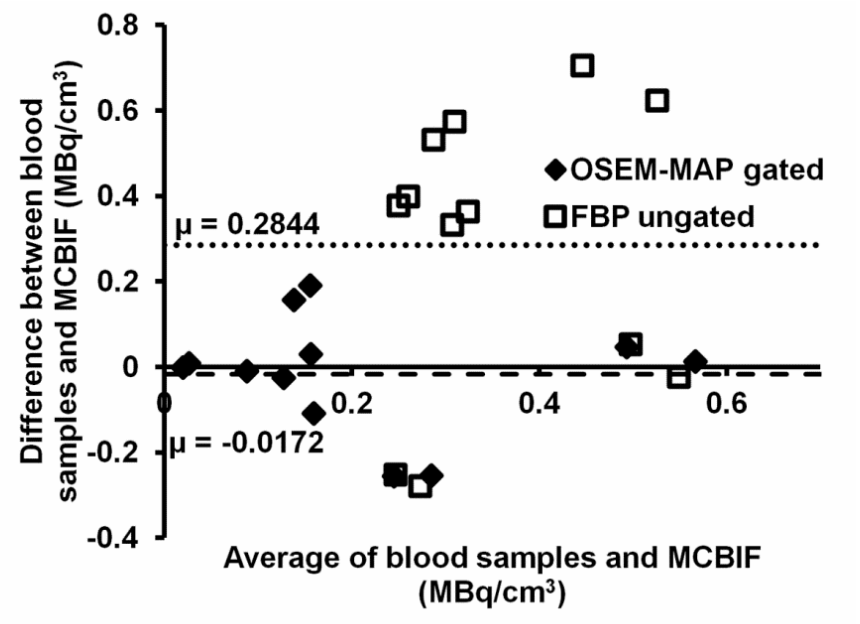

Figure 4-3 Residual plot shows the difference between MCBIF applied to OSEM-MAP cardiac and respiratory gated images (diamonds) and FBP un-gated images (open squares), when compared to the 2 late venous blood samples obtained at 43 and 56 minutes post FDG administration.

A residual plot of MCBIF applied to OSEM-MAP gated images, when compared to the two late venous blood samples obtained from n = 6 mice, is shown in Figure 4-3. The analysis reveals an average difference of 0.017 MBq/ cm^3. The precision (standard deviation of differences) was calculated to be 0.13 MBq/ cm^3. The figure also shows the analysis obtained from FBP un-gated images. An average difference of 0.28 MBq/ cm^3 and precision of 0.33 MBq/ cm^3 were obtained from FBP un-gated data sets. The residual plot exhibits the quantitative accuracy and repeatable behavior of MCBIF when applied to OSEM-MAP gated images.

Table 4-2 SP, PV factors, and FDG influx constant generated by model correction on OSEM-MAP gated images in n = 6 mice.

r_m	r_b	S_{bm}	S_{mb}	k_i
0.30 ±0.01	0.73 ±0.04	0.21 ±0.03	0.12 ±0.01	0.15 ±0.03

The PV and SP factors, along with the net myocardial FDG influx constant k_i generated by minimization, are shown in Table II. $k_i = 0.15 \pm 0.03$, shown in Table II, agrees with that obtained from arterial blood sampling, $k_i = 0.14 \pm 0.06$ [80]. A student t-test revealed a P value of less than 0.05, indicating statistical significance. Also, the downstream k_i has a lower variance (~20%) as compared to a variance of ~52% reported in [80] obtained from un-gated FBP images.

4.5 Discussion

Compartment model has long been regarded as a reliable way of analyzing dynamic PET images, and the accurate knowledge of blood input function is crucial to tracer kinetic modeling [90][91]. However, including the procedure of acquiring arterial blood samples in routine PET procedure is not practical due to the invasive blood sampling surgery preparation, limited blood volume and extensive radioactivity measurement efforts. Although there are automated procedures for sampling blood using beta-microprobes in small animals [69][92][93] an alternative methodology without invasive blood sampling is highly desired. Obtaining image-derived blood input function from dynamic PET images is the simplest way, but SP and PV effect makes it unreliable [77].

In this study we proposed a reliable and practical method, which can simultaneously correct for the SP and PV effects and generate kinetic rate constants without any invasive blood sampling.

A recent study by Shogi et al indicated that IDIFs obtained from high-resolution images still have about 15-20% SP contamination in them [78]. We showed, for the first time, that model correction on high resolution FDG PET gated images with correct PV bounds, models the wash-in and wash-out dynamics of the tracer from mouse blood, without the need for any blood sampling (equation 3-16) as opposed to [80]. Our study compares the gold standard blood input function obtained by arterial blood sampling from a single mouse and model corrected estimate of blood input function, for validation purposes only. Since the arterial blood samples are well approximated by venous blood at the late time points [80], we established statistical significance by sampling blood from the tail-vein at 43 min and 56 min, with same time points on MCBIF in n=6 mice. The residual plot indicates that MCBIF applied to OSEM-MAP gated images are repeatable compared to that obtained from FBP un-gated images. The downstream rate of myocardial FDG influx, Ki is not only quantitative but also repeatable as indicated in the results section.

The kinetic model proposed in this study may also be adapted to different PET tracers such as ^{13}N-ammonia for measuring myocardial perfusion or ^{11}C-acetate for measuring flow and oxygen consumption *in vivo* [93]. The kinetic rate constants and compartments can be adjusted to adapt to different metabolic processes for different tracers, while the form of the equations of the model corrected image-derived heart ventricle and image-derived tissue time activity would have a similar form. Also, the initial values and optimization bounds should be modified when switching to other tracers or animal models. In addition, blood samples from a number of experimental subjects may be necessary to validate model output estimates. Nevertheless, application of this technique to other scanners and isotopes would require careful validation since positron range and depth of interaction will be different for other isotopes and scanners.

4.6 Conclusions

MCBIF applied to OSEM-MAP gated images correctly accounts for the shape, wash-in and wash-out dynamics of FDG from mouse blood without the need of any invasive blood sampling. Lower SP of radioactivity from the myocardium to the BP and higher PV recovery from OSEM-MAP gated images lead to improved MCBIF estimate as compared to that obtained from un-gated FBP images in a dynamic PET scan of the mouse heart.

5 Early Detection of Metabolic Remodeling in a Mouse Model of Pressure Overload Left Ventricular Hypertrophy *in vivo*

5.1 Introduction

Myocardial hypertrophy is considered initially an adaptive response to stress. When stress is sustained, however, hypertrophy becomes maladaptive. Both functional and structural changes are accompanied by changes in energy substrate metabolism. A hallmark finding in myocardial hypertrophy is a shift away from fatty-acid to glucose oxidation [94]. Based on earlier work ex vivo, we have proposed that this metabolic remodeling precedes and triggers left ventricle (LV) structural and functional remodeling in pressure overload left ventricular hypertrophy (LVH) and induces the fetal gene program [95][96][97]. However, this hypothesis has never been evaluated *in vivo*. For this purpose we used the mouse model of left ventricular pressure overload after transverse aortic constriction (TAC) as a clinically relevant model to assess metabolism and function of the heart subjected to pressure overload [98] using 2-[18F] fluoro-2deoxy-D-glucose (FDG) Positron Emission Tomography (PET) imaging.

A compartmental modeling technique was used to analyze images obtained dynamically to compute rate of myocardial FDG uptake and utilization. The quantification of these rates has been limited by two important factors: a) the limited spatial resolution of the small animal PET scanners [70][71]leading to partial volume (PV) effects, and b) the spill-over (SP) of radioactivity from the blood pool (BP) to the myocardium and vice-versa. A major shortcoming of the image-derived blood input function (IDIF) method is that it is susceptible to SP and PV effects [70].

In this study, a compartment model corrected blood input function (MCBIF) was optimized, wherein the blood input function with SP and PV corrections and the metabolic rate constants in a 3-compartment model were simultaneously estimated from OSEM-MAP cardiac and respiratory gated PET images with attenuation correction [1][2]. Left ventricular ejection fraction (LVEF) was also measured using high resolution gated PET images, which enabled us to perform a side-by-side comparison of cardiac metabolism, and LV function.

5.2 Animal Model

Sixteen adult C57BL/6 male mice (9-10 weeks of age) obtained from Charles River were imaged at baseline using a MicroPET Focus-F120 scanner (Siemens, Inc.) under sevofluorane anesthesia [82]. A subset of these mice (n = 11) were subjected to a transverse aortic constriction (TAC) surgical procedure to induce pressure-overload hypertrophy [79]. Briefly, mice were anesthetized with isoflurane and intubated for ventilation. A thoracotomy was performed and a 7-0 silk suture was tied around the transverse aorta between the proximal and distal carotid arteries against a 27-gauge needle, after which, the needle was removed. Osmotic mini-pumps containing either propranolol (5 mg/kg/day) obtained from Sigma Aldrich Inc. (n = 6) or vehicle alone (n =

5) were implanted subcutaneously at the end of surgery. In addition, five sham-operated animals were subjected to the same surgical protocol, without tying off the suture. Before and after surgery all mice were kept in a 12 hrs light/12 hrs dark cycle environment. Prior to imaging, animals were fasted overnight with only access to water [81].

PET scans were performed between 9 a.m. and 5 p.m. on anesthetized animals. All experiments were performed in compliance with the Guide for the Care and Use of Laboratory Animals, published by the National Institutes of Health and was conducted under protocols approved by the Institutional Animal Care and Use Committee at the University of Virginia.

5.3 MicroPET Imaging Protocol

PET imaging for measuring myocardial FDG uptake and glucose utilization was carried out using 18F-FDG in the sham, TAC and TAC treated with propranolol mice as follows: Following the insertion of a tail-vein catheter, ECG surface electrodes (Blue Sensor, Ambu Inc., Glen Burnie, MD) were placed on both forepaws and the left hindpaw and a pneumatic respiratory pillow was placed on the animal's chest. 60 minute dynamic PET scan was performed under 2.5% sevoflurane anesthesia in oxygen [82], where data acquisition was initiated a few seconds before the slow administration of about 800 µCi FDG over 30-60 seconds via the catheter. Small Animal Instruments, Inc., model 1025L for PET was used for continuously monitoring heart rate, respiration, and core body temperature (rectal probe). Cardiac gate signals were generated at the end-expiration phase of the respiratory cycle to time-stamp the PET scanner data for subsequent retrospective reordering into heart and respiratory-cycle based time-bins [83]. Transmission scan using Co57 point source was done for attenuation correction prior to FDG administration. The list mode data sorted into 23 time bins (11 × 8 s, 1 × 12 s, 2 × 60s, 1 × 180 s, and 8 × 400 s) and 3 gates (hence referred to as gated) were reconstructed using OSEM-MAP algorithm [1][79][86] with attenuation correction. For comparison the data were also reconstructed using Filtered Back Projection (FBP) algorithm (ramp filter cutoff at the Nyquist frequency) with the same spatial resolution without gating. The images were corrected for radioactive decay, random coincidences and dead-time losses using the MicroPET Manager (Siemens Inc.). Regions of interest (ROI) in the region corresponding to the LV blood pool (LVBP) and the myocardium were drawn in the last frame and the last gate of the dynamic image data and time activity curves for the LVBP and the myocardium were generated for the whole scan duration of 60 minutes. Blood samples were also collected at around 43 and 56 minutes post FDG administration from the tail vein to validate the MCBIF. Three blood samples before and 3 blood samples after the PET scan were drawn by a tail-vein nick to measure blood glucose levels using a glucometer (Accu-Chek, Roche). The average of these blood glucose readings were used to compute the rate of myocardial glucose utilization (rMGU).

5.4 Data Analysis

A compartment model corrected blood input function (MCBIF) [1][80] was optimized in this manuscript (see below), which is based on simultaneous estimation of the blood input function with SP and PV corrections and the metabolic rate constants. The formalism for MCBIF was utilized to measure the net myocardial FDG influx, k_i and hence glucose utilization, rMGU, in the sham, TAC, and TAC treated with propranolol mice *in vivo*.

End-systolic volumes (ESV) and end-diastolic volumes (EDV) were also measured by drawing ROIs at the end-systolic and end-diastolic phases of the heart cycle over multiple slices covering the whole heart from the apex to the base. The volumes obtained in each phase over multiple slices were summed to obtain net ESV and EDV in micro liters (μl). The LVEF was measured by:

$$LVEF = \frac{EDV - ESV}{EDV} \times 100\% \qquad \textbf{5-1}$$

5.4.1 Dynamic Data Analysis

The rate of myocardial glucose utilization can then be computed as:

$$rMGU = k_i [Glu] / LC \qquad \textbf{5-2}$$

in μmoles/g/min, where [Glu] is the average non-radioactive blood glucose levels measured using a glucometer and LC is the lumped constant. The lumped constant corrects the difference of affinity between glucose and FDG to glucose transporters and the phosphorylating system. In recent years the value of the lumped constant has been questioned, and it is uncertain which value should be used [99][100][101][102]. In the 3-compartment model of glucose transfer into cells, the lumped constant is a function of the correlation between the net and the unidirectional rates of uptake of glucose and glucose tracers such as FDG. For sake of simplicity, like many investigators we have used LC =1 [103][104].

5.4.2 Statistical Analysis

Statistical analysis was performed using SigmaStat 3.0 (SPSS, Inc, Chicago, IL). Mean values of k_i, [Glu], rMGU and LVEF were calculated with standard error. Two way repeated measures analysis of variance (ANOVA) and Holm-Sidak post hoc test were used to compare mean values in the sham, TAC and TAC treated with propranolol groups at different time points. A p value of less than 0.05 was considered as statistically significant.

5.4.3 Quantitative Accuracy of MCBIF Applied to IDIF from OSEM-MAP Gated Images

Representative IDIF's obtained from OSEM-MAP gated images (line with open squares) and from FBP un-gated images (line with open circles) with attenuation correction are shown in Figure 5-1A. MCBIF applied to IDIF obtained from OSEM-MAP gated (line with solid squares) and FBP un-gated images (line with solid circles) are also shown in the figure. The venous blood samples at 43 and 56 minutes are shown for comparison (open triangles). MCBIF applied to the IDIF obtained from high resolution gated images correctly accounted for the wash-out dynamics of FDG from the blood, when compared to the late venous blood samples. Fig. 2B shows MCBIF estimation during the first 5 minutes of the scan, indicating improved PV recovery when applied to IDIF obtained from OSEM-MAP gated images as compared to that obtained from un-gated FBP images.

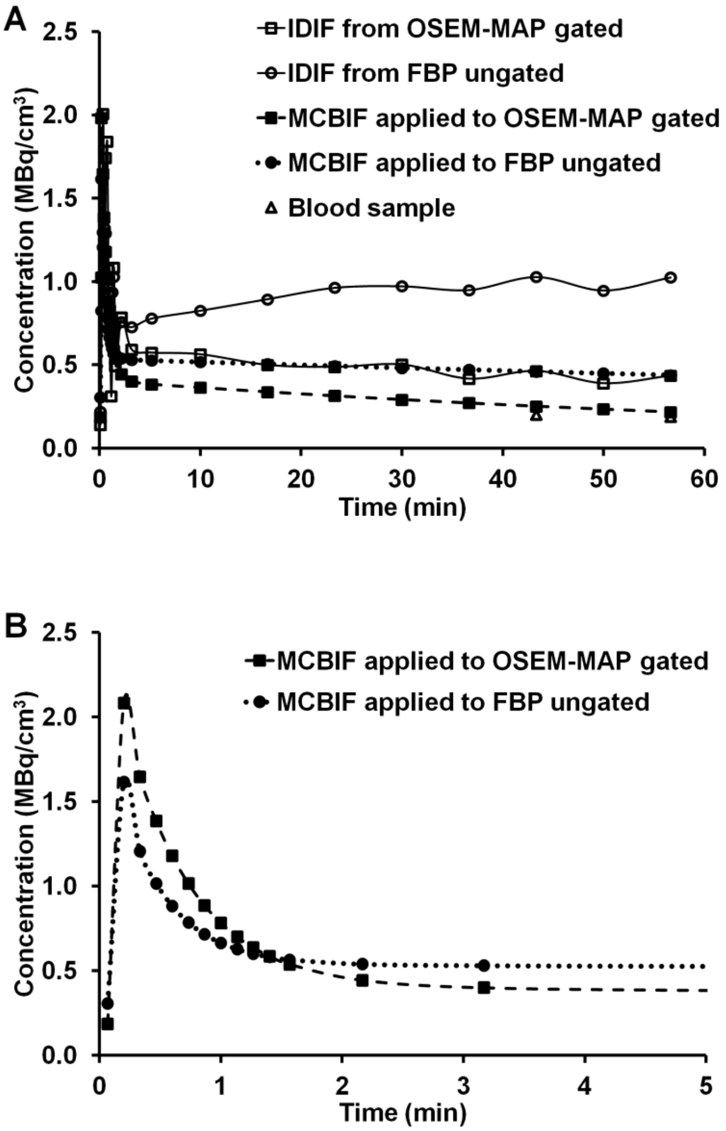

Figure 5-1 MCBIF estimation for the whole scan duration and first 5 minutes of the scan. **(A)** MCBIF estimation for the whole scan duration. Representative IDIF's obtained from OSEM-MAP cardiac and respiratory gated images (line with open squares) and from FBP un-gated images (line with open circles) with attenuation correction. MCBIF applied to IDIF from the former (line with solid squares) and the latter (line with solid circles) are also shown in the figure. The venous blood samples at around 43 and 56 minutes are shown for comparison (open triangles). MCBIF applied to the IDIF obtained from high resolution gated images, correctly accounts for the wash-out dynamics of FDG from the blood, when compared to the late venous blood samples. **(B)** MCBIF estimation during the first 5 minutes of the scan.

The scan indicates improved PV recovery when applied to IDIF obtained from OSEM-MAP gated images as compared to that obtained from un-gated FBP images.

5.5 Metabolic Remodeling in LVH in Mice *In vivo*

The measured rate of myocardial FDG uptake, k_i (ml/g/min), for the mice in the 3 categories are shown in Figure 5-3(A) over a period of 7 days. The plot shows increased myocardial FDG uptake at day 1 post TAC surgery by 580% indicating an adaptive response with preserved LVEF (Figure 5-3(B)). k_i increased further at day 7 with a drop in function by 24%.

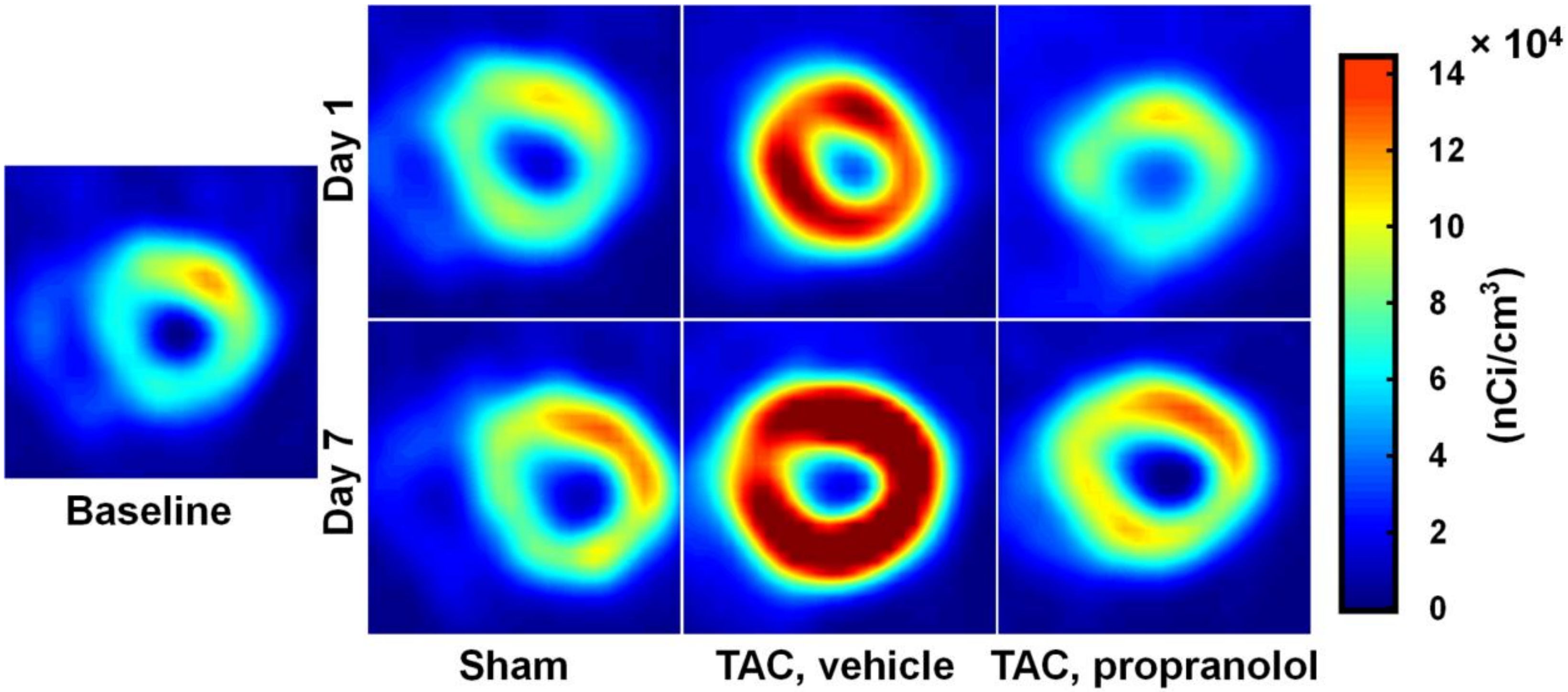

Figure 5-2 Gated transverse PET images *in vivo*. End-diastolic transverse PET images at last time bin for sham mice, TAC mice, and TAC mice treated with propranolol at baseline, day 1, and day 7 after surgery are shown. All scans are from same animals. Images indicate enlargement in LV cavity in TAC mice over 7 d. Images also show increase in 18F-FDG uptake in TAC mice starting at day 1, indicative of metabolic adaptation in pressure-overload LVH.

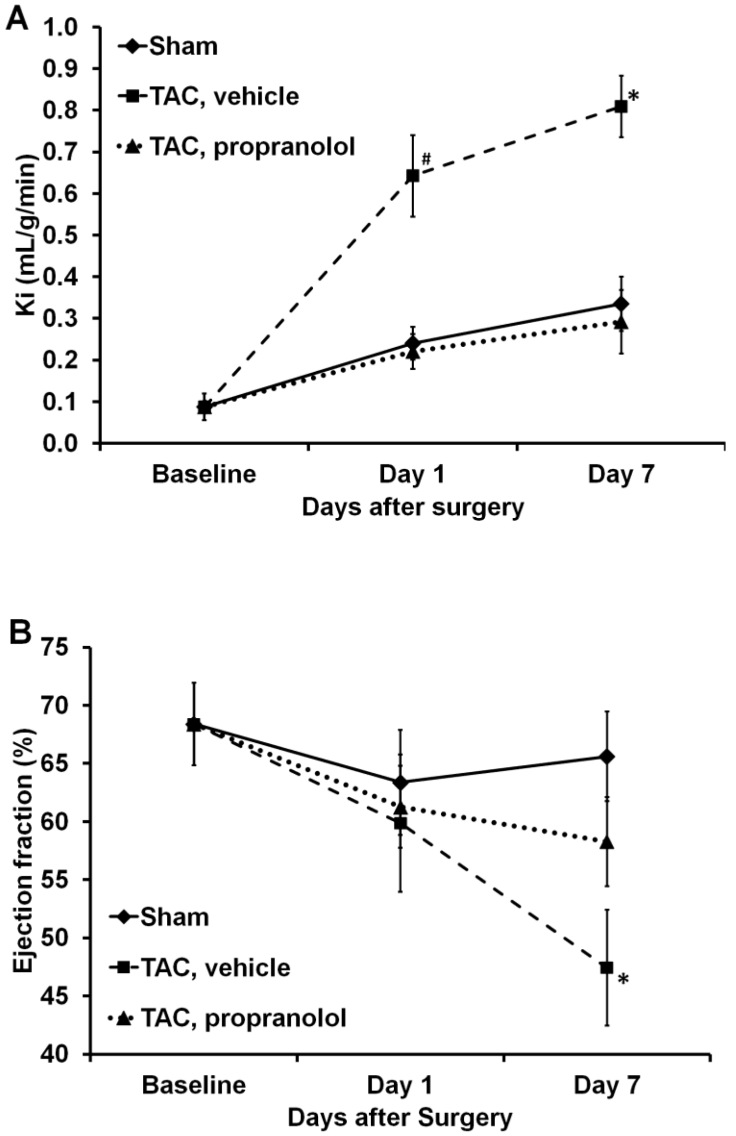

Figure 5-3 Measured rates of myocardial 18F-FDG uptake k_i and LVEF of the three groups over the 7 days period. **(A)** Measured rates of myocardial 18F-FDG uptake *in vivo*. k_i (mL/g/min) for sham mice (n = 5), TAC mice, vehicle (n = 5) mice, and TAC mice treated with propranolol (n = 6) are shown. Myocardial 18F-FDG uptake at day 1 after TAC surgery is increased by 580%, indicating adaptive response to stress. k_i increased further on day 7 in TAC mice, whereas TAC mice treated with propranolol exhibited attenuated rate of myocardial 18F-FDG uptake over 7-d period. Metabolic changes in TAC mice treated with propranolol were comparable to sham group. All values are mean ± SEM. **(B)** Measured LVEF from

dynamic gated PET images *in vivo*. Plot indicates insignificant drop in function in TAC mice on day 1. On day 7, function dropped by 24% in TAC mice whereas there is insignificant drop in function in TAC mice treated with propranolol. Sham group indicates no significant change in function over 7-day period. All values are mean 6 SEM. *#P , 0.05 vs. baseline, TAC treated with propranolol, and sham groups.

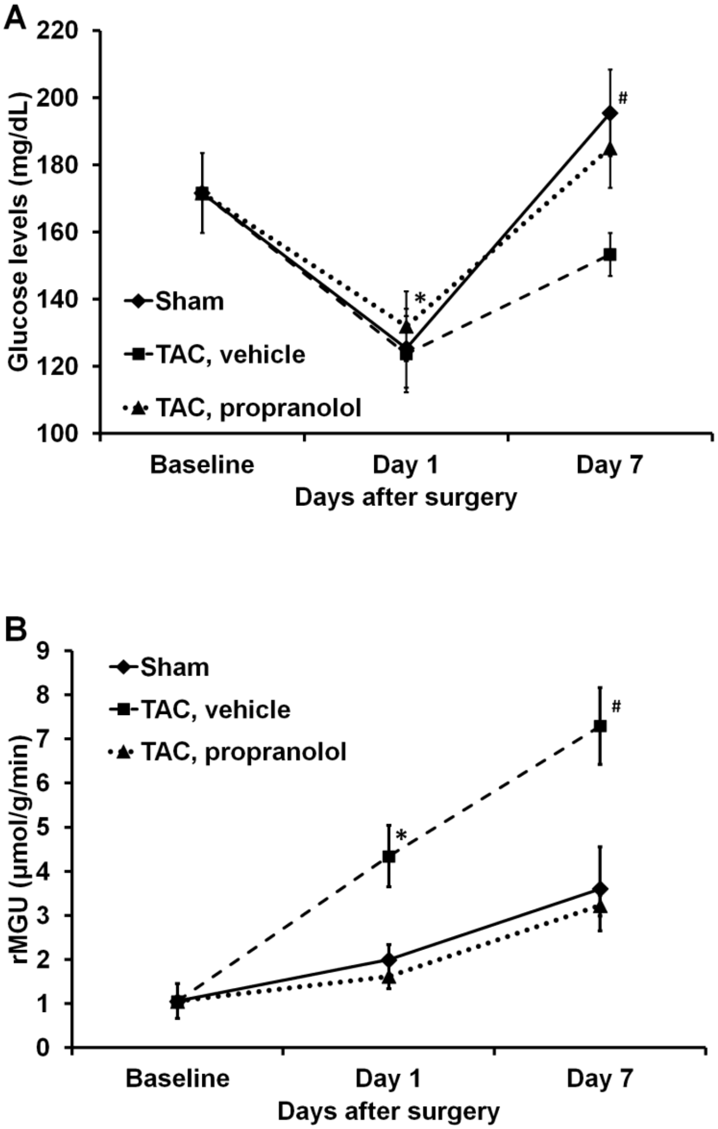

Figure 5-4 Blood glucose levels and rMGU of three groups over the 7 days period. **(A)** Blood glucose levels. Plot shows average blood glucose levels measured at each time point for sham mice, TAC mice, and TAC mice treated with propranolol. All values are mean ± SEM. *P , 0.05 vs. BSL and day 1. #P , 0.05 vs.

TAC at day 7. **(B)** rMGU was measured at each time point for sham mice, TAC mice, and TAC mice treated with propranolol. All values are mean ± SEM. *P , 0.05 vs BSL, day 1, TAC treated with propranolol, and sham groups. #P , 0.05 vs baseline, TAC treated with propranolol, and sham groups.

The blood glucose levels and rate of myocardial glucose utilization (rMGU) are also shown in Figure 5-4 (A-B) for the 3 categories over a period of 7 days. We observe a drop in the blood glucose levels at day 1 for the sham, TAC and TAC mice treated with propranolol. Mice treated with propranolol show an elevation in blood glucose levels at day 7 significantly different from day 1 and comparable to shams or mice at baseline. The TAC mice exhibit an insignificant increase in the blood glucose levels between day 1 and day 7 (Figure 5-4(A)). The rMGU (Figure 5-4(B)) did not increase linearly with k_i. Rather, rMGU increased at a much slower rate than k_i, thereby resulting in a mismatch of 29% between k_i and rMGU in the TAC mice (Figure 5-5).

On the other hand, early treatment with propranolol [105] targeting metabolic alterations attenuated rate of myocardial FDG uptake (Figure 5-3 (A)), reduced mismatch between k_i and rMGU to 9% and rescued cardiac function (Figure 5-3 (B)). The metabolic changes and cardiac function in the TAC mice treated with propranolol were comparable to the shams. The *in vivo* imaging results suggest that early metabolic remodeling may precede and trigger the onset of severe contractile dysfunction in LVH in mice.

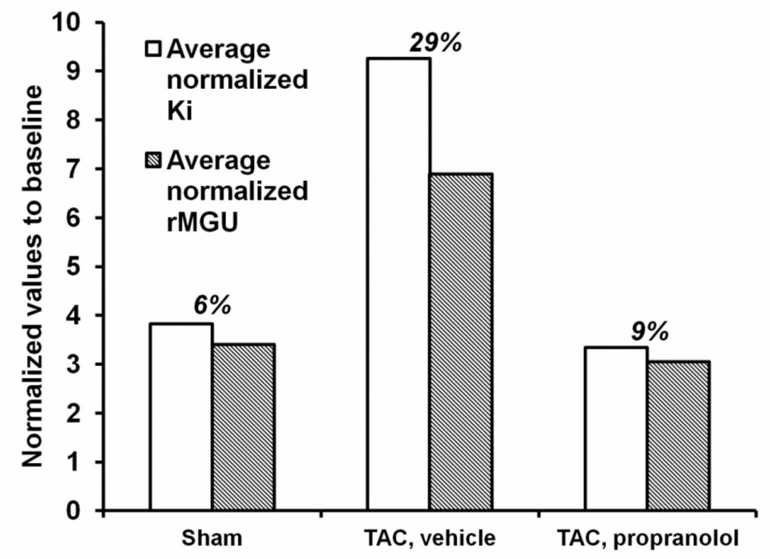

Figure 5-5 Comparison between k_i and rMGU measured *in vivo* at day 7.

Figure 5-5 shows that rMGU did not increase linearly with k_i. rMGU increased at much slower rate than k_i, resulting in mismatch of 29% between k_i and rMGU in TAC mice. Treatment with propranolol reduced mismatch to 9% and rescued cardiac function.

5.6 Conclusions

In the normal heart fatty acid oxidation is the predominant source (60-90%) of ATP, with glucose oxidation and lactate contributing the rest [106]. Stress on the myocardium, such as biomechanical stress from pressure overload, changes normal myocardial substrate metabolism. In the case of pressure-overload induced hypertrophy the prevailing notion is that alterations in energy substrate metabolism adversely affect the response to myocardial ischemic stresses and contribute to contractile dysfunction. Specifically, in the hypertrophic heart there is a shift away from fatty acid oxidation towards glucose metabolism [94]. At least initially, this metabolic remodeling may be considered as adaptive, most likely because glucose oxidation yields more ATP per atom of oxygen [95]. With time, however, the adaptive response becomes maladaptive as this shift in metabolism does not increase ATP production commensurate with the increased demand for energy by the heart.

Recently we have proposed a requirement for hexose 6-phosphate in mTOR signaling, and cardiac growth [107]. However, in the setting of insulin resistance, an oversupply of substrate (glucose) may “starve the heart in the midst of plenty” [108]. The hypothesis, however, has never been tested serially *in vivo* due to the limited availability of technologies for studying complex metabolic parameters and LV function. It is tempting to speculate that strategies to improve myocardial substrate utilization and to improve metabolic flexibility [96][109] in the hypertrophic heart may improve contractile performance and prevent the onset of heart failure.

During acute pressure overload and inotropic stimulation [110], glucose oxidation is increased, but it is not yet completely clear how glucose uptake is related to LV function during pressure overload LVH. Studies using Single Photon Emission Computed Tomography (SPECT) imaging have demonstrated that the metabolic switch can be measured in both small animals and human beings [111][112]. However, a serial study on the temporal relationship between glucose uptake and cardiac function *in vivo* in mice using PET has not been done. We demonstrated that MCBIF applied to an IDIF obtained from high resolution gated images with less severe SP and PV effects is quantitative and also repeatable as compared to that obtained from low resolution un-gated images [80]. The results of our present study support the hypothesis that increase in glucose metabolism in the form of increased FDG uptake precedes and triggers the onset of severe dysfunction of the heart in LVH. This is an important point, since early detection of metabolic remodeling may lead to early intervention targeting metabolic changes to prevent the onset of severe contractile dysfunction and improve patient outcomes clinically. We also observe that early treatment with propranolol attenuated myocardial glucose uptake and rescued cardiac function *in vivo*. Thus, metabolic imaging with FDG-PET may provide an early indication of a beneficial effect of a therapy, which may provide a platform for aggressive treatment strategies to improve outcomes clinically.

Dietary conditions affect FDG PET imaging studies [113]. Some clinical studies use glucose load conditions without fasting to obtain higher quality images. On the other hand, fasting can produce similar quality images. Because we are interested in FDG dynamics, a reasonable contrast between the blood pool and the myocardial tissue enables us to draw ROI's and determine rate of myocardial FDG influx with SP and PV corrections. Moreover, performing glucose clamps in mice is challenging in addition to the TAC surgery, so we resort to overnight fasting for our FDG PET scans in order to achieve uniform metabolic conditions to obtain k_i, and rMGU.

The lumped constant, LC, is an important parameter in the determination of the rMGU in a dynamic PET scan. This value may vary, depending upon plasma substrate and hormonal conditions. Many authors have used a constant value of LC to compute MGU in humans with T2D [114]. Botker et al. [115] proposed that LC is a function of rates of FDG transport and phosphorylation and applied the method to assess MGU in humans with ischemic cardiomyopathy [116]. In a study by Herrero et al [117], a constant value of LC was used for assessing myocardial glucose uptake for FDG PET studies in dogs. However, they also observe that the correlation between Fick derived and PET derived rMGU has lower correlation with variable LC. The correlation coefficient does not differ after correcting for LC=0.67 for FDG PET studies. They also observe that using variable LC leads to significant underestimation of rMGU in large animals. In the current work, we used LC=1 as we did not measure this constant and there is no consensus on how to deal with this issue. The concerns expressed earlier by Botker et al [115] do not apply because here the metabolic conditions were the same for all animals and in steady state. Nevertheless, further studies need to be done to characterize LC in small animal PET imaging of the heart.

Our study is not without limitations. First, FDG can only be considered as a surrogate marker for glucose metabolism. While FDG indirectly assesses glucose transport and phosphorylation the tracer analog is subjected to changes in the lumped constant [100]. Secondly, although clinically relevant, the acute nature of the model may be a limitation in evaluating the hypothesis of metabolic remodeling precede and trigger cardiac dysfunction in LVH. The slowly progressive Dahl salt sensitive hypertensive rat model may be more relevant to evaluate metabolic and functional changes in the heart, *in vivo*, but the costs for a study like the present one would be prohibitive [118]. Using the one-kidney, one-clip rabbit model of hypertension we have already shown by invasive measurements that metabolic remodeling of the heart precedes hypertrophy [95]. Third, we have not considered any possible differences in plasma substrate or hormone levels, although all scans were obtained under the same conditions and errors would be systematic errors.

Non-invasive serial imaging of the heart subjected to pressure overload hypertrophy using PET supports the hypothesis that changes in glucose analogue FDG metabolism precedes and triggers the onset of severe cardiac dysfunction in LVH. We found that enhanced uptake of FDG by the myocardium in mice subjected to pressure overload hypertrophy precedes and possibly triggers the onset of contractile dysfunction. Early intervention with a standard of care treatment prevented maladaptive response and rescued cardiac function. We speculate that early detection of metabolic remodeling may offer a metabolic target for modulation of hypertrophy.

6 Non-Invasive Detection of Early Metabolic Remodeling from Dynamic FDG PET Images of the Heart: First in Human Study

6.1 Introduction

Hypertension, characterized by an increase in systemic arterial blood pressure affects about 30% of the US population ≥ 20 years of age [119] and is a common cause of left ventricular hypertrophy (LVH) [120]. LVH is a powerful and independent predictor of increased cardiovascular morbidity and mortality in patients with hypertension. There is a lack of effective therapies to treat LVH due to hypertension; therefore early detection and prevention are important. Acute pressure overload prompts the heart muscle to switch from fatty acids to glucose as its main source for oxidative energy production [94][110][121]-[123]. This adaptive response is beneficial to cardiac function in the acute situation. However, sustained pressure overload reactivates the fetal gene program [124] and makes the metabolic change permanent. This in turn leads to metabolic inflexibility and dysregulation that characterizes the failing heart [96][97]. Therefore, strategies to improve energy generation and use have received renewed interest as a therapeutic target to improve patient outcomes [125]-[131]. The key issue is to identify the temporal and causal relationship between metabolic remodeling and impaired cardiac function and the development of LVH, and to define a window for aggressive therapy to prevent disease progression. PET imaging is an excellent tool to address this issue [2][132][133].

Accurate non-invasive imaging of myocardial substrate metabolism that can be performed in animals and humans will be important in identifying changes in myocardial metabolism before and during the development of LVH and in identifying and establishing therapies to prevent LVH [132][134]. We hypothesize that alterations in glucose metabolism in the pressure-overloaded heart precede the development of impaired cardiac function and thus, targeting the changes in glucose metabolism may prevent the development of functional and consequently structural changes in the pressure-overloaded heart that lead to LVH and heart failure.

In chapter 4 and 5 we developed an improved methodology for non-invasive quantification of rate of myocardial glucose uptake *in vivo* in the mouse heart using dynamic FDG PET imaging [1][2]. Using this method we tested the hypothesis in mice heart *in vivo*, that early metabolic remodeling in the form of increased myocardial FDG uptake precedes structural LV remodeling in conjunction with a decrease in cardiac function, in an acute mouse model of transverse aortic constriction (TAC) induced pressure overload LVH [2][87]. The TAC mouse model [79][136] lacks some of the key features of the human disease, most importantly the slow progressive development of pressure overload. This makes it difficult to distinguish the maladaptive from the adaptive metabolic response and to identify the window for aggressive therapeutic strategies that improve outcome and could be readily translated to clinical practice. In this first-in-human clinical study, adapting the dynamic FDG PET imaging and quantitative techniques developed in mouse heart, we tested the hypothesis that metabolic remodeling precedes structural and functional remodeling in hypertension-induced LVH.

6.2 Materials and Methods

6.2.1 Patients

Thirty-one patients (11 men, 20 women) participated in the study. The presence of hypertension was determined through chart review. All patients without known coronary disease or symptoms of ischemia underwent resting 2-dimensional echocardiography at the University of Virginia Echocardiography Laboratory.

6.2.2 Echocardiography

All patients underwent resting 2-dimensional transthoracic echocardiography. LVH was considered present in the setting of an end-diastolic left ventricular interventricular septal or posterior wall dimension ≥ 1.2mm measured after closure of the mitral valve at end-diastole (ASE Chamber Quant). Left ventricular mass was calculated using the Devereaux formula, and dividing by the body surface area gives the left ventricular mass index [135]. Left ventricular diastolic function assessment included assessment of tissue Doppler and mitral inflow velocity Doppler. LV ejection fraction was also determined by echocardiography. Heart weight to body weight ratios (HW/BW) were calculated using LV mass. The echocardiogram was ordered clinically, and the imaging study was performed following the clinical protocol.

6.2.3 FDG PET Imaging Protocol

All the patients in the 3 different groups were fasted for > 6 hours prior to the PET procedure. During the initial phase of each protocol, the patients were positioned in a Siemens Biograph mCT PET-CT scanner. A 10 minutes 40-slice CT scan was acquired before the FDG PET scan for attenuation correction.

For evaluation of myocardial glucose metabolism, 20 minutes dynamic 2-[^{18}F] fluoro-2deoxy-D-glucose (FDG) PET scan was performed with cardiac gating on a Siemens Biograph mCT PET-CT scanner. FDG in the amount of 10-15 mCi was slowly administrated over 30 seconds via an intravenous catheter, 20 minutes of dynamic PET data acquisition followed within a few seconds. The list mode PET data were reconstructed using an iterative reconstruction algorithm into 30 dynamic frames as follows: frames x time (seconds) (12×10 s; 8×30 s; 8×60 s; 2×180 s).

6.2.4 Data Analysis

The data were analyzing blinded of clinical data. For each patient, midventricular transaxial slice from the last time frame of dynamic PET image was used for drawing regions of interest (ROIs) in the areas corresponding to the LV blood pool and the myocardium, and time activity curves generated from the dynamic PET images using Siemens Syngo. The methodology [1] in which the blood input function with spillover and partial volume corrections and the metabolic rate constants were simultaneously estimated in a 3-compartment tracer kinetic model, was used to determine the rate of myocardial FDG uptake, ki (ml/ min/ g). Mean values of Ki, HW/BW ratios and wall thickness in the 3 groups of patients were compared using ANOVA and Tukey's Studentized Range testing.

6.3 Results

Among the thirty-one patients enrolled, 9 were with hypertension (HTN) with left ventricular hypertrophy (LVH), 11 were with HTN without LVH, and 11 controls were with neither LVH nor hypertension. All patients had normal left ventricle ejection fraction (55-65 %). The mean age differed significantly between the groups ($p = 0.017$); it was lower in the control group (43 ± 13 y) than in HTN with LVH (59 ± 13 y, $p = 0.029$). There was no significant age difference between HTN with LVH and HTN without LVH (57 ± 12 y, $p = 0.971$) patients. Female gender comprised of 65% of the patient population in the control group with 67% and 50% respectively for the HTN with LVH and HTN without LVH groups.

The mean metabolic measurements (ki) for the three groups were significantly different (Figure 6-1 A). It was higher in HTN without LVH patients (0.104 ± 0.012 mL/min/g) compared to HTN with LVH (0.029 ± 0.004 mL/min/g) ($p < 0.001$) and control (0.069 ± 0.003 mL/min/g) ($p = 0.003$) patients. The mean Ki for the controls differed significantly from the HTN with LVH group ($p<0.001$).

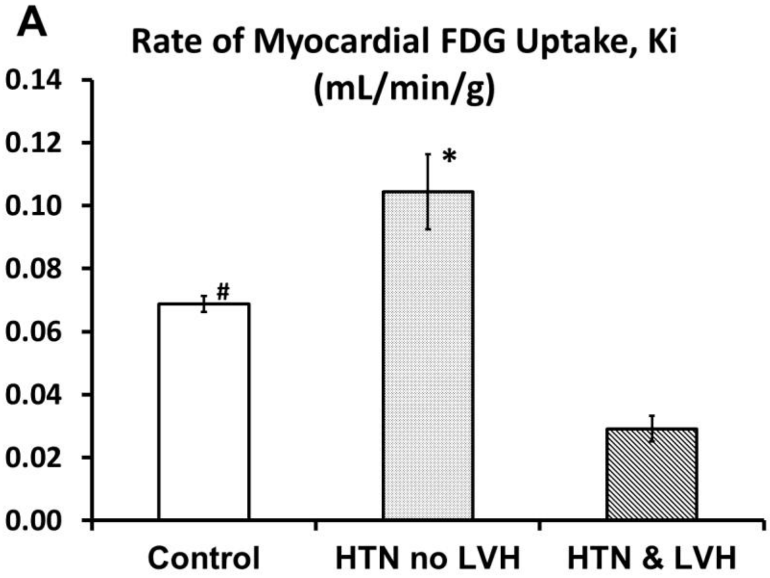

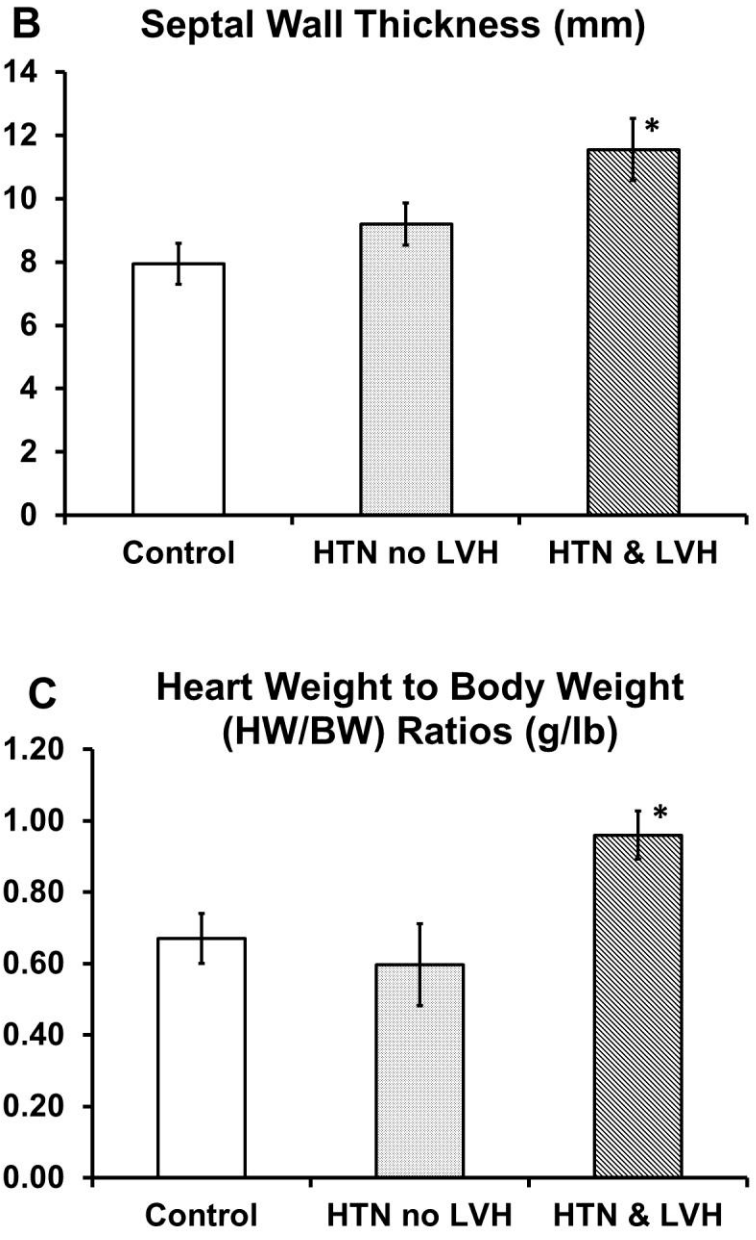

Figure 6-1 Myocardial metabolism and left ventricle structure in hypertension induced LVH patients. (A) Measured rate of myocardial FDG uptake, Ki. $*p < 0.05$ vs control and HTN &LVH; $\#p < 0.05$ vs HTN & LVH. (B) Measured septal wall thickness, $*p < 0.05$ vs control and HTN &LVH; (C) Heart weight measured from LV mass, $*p < 0.05$ vs control and HTN &LVH.

The mean septal wall thickness (Figure 6-1 B) differed significantly between the groups (p = 0.009); it was higher in HTN with LVH (11.5 ± 2.9 mm) than in control (7.9 ± 2.3 mm, p = 0.006) patients. The mean wall thickness for the HTN without LVH patients did not differ significantly from the control patients (p = 0.523). The mean HW/BW (Figure 6-1 C) differed significantly between the groups (p = 0.013); it was higher in HTN with LVH (0.96 ± 0.2 g/lb) than in HTN without LVH (0.6 ± 0.3 g/lb, p = 0.021) and control (0.67 ± 0.3 g/lb, p = 0.034) patient populations. There was no significant difference in HW/BW ratios between HTN without LVH and control (p = 0.809) patients.

6.4 Discussion

First, our results indicated that metabolic changes (Figure 6-1 A) precede structural remodeling (Figure 6-1 B) in patients with hypertension. Figure 6-1 (B) (C) indicates heart weight to body weight ratios and septal wall thickness measurements in control patients and patients with hypertension, and the data show no significant changes in heart structure with hypertension alone. Thus significant metabolic changes in the form of increased rate of myocardial FDG uptake Ki, precedes any changes in heart weight to body weight ratios and wall thickening in hypertensive patients as compared to controls. Successful observation of this trend in a larger patient population may provide a window for early intervention using aggressive therapeutic strategies to prevent structural remodeling, progression to LVH, and heart failure.

Secondly, in patients with hypertension and LVH, we observe a reduction in the rate of myocardial FDG uptake with preserved function. The lower myocardial FDG uptake in the HTN with LVH patient group may be due to impaired glucose tolerance. We hypothesize that insulin resistance (IR) may be a protective mechanism for the pressure overloaded hearts. The hypertrophied and failing heart exhibits defective insulin stimulated glucose transport, or IR. Since IR is one of the earliest detectable changes in the development of cardiovascular disease (CVD) [137], it is often branded as a perpetrator of cellular and physiologic damage and most therapeutic interventions are aimed at overcoming this condition. However, more recent evidence indicates a seemingly paradoxical finding that insulin sensitizers such as Rosiglitazone, which improve glucose transport into the insulin resistant heart [138], are linked to cardiovascular events in type II diabetic patients [139][140]. These data have led to the speculation that IR in the pressure overload heart may be a protective mechanism. IR reduces glucose transport into cardiac tissue. On the one hand, this could be viewed as a maladaptation which limits the heart’s ability to function normally, while on the other hand IR might be a mechanism for cellular preservation by reducing glucose toxicity. This hypothesis can be tested by imaging a larger patient population, along with the measurement of other metabolic parameters such as blood glucose levels and glycated hemoglobin (HbA1c).

The significance of this study lies in the early detection strategy of metabolic changes in the pressure overload heart, using improved PET acquisition and analysis techniques, before any structural remodeling happens. The unique advantage of this multi-parameter approach is that no prior knowledge of the cardiac dimensions is needed. From a clinical perspective, measurement of absolute metabolic activity is very important when using one single measurement to identify which hypertensive patients are going to develop LVH or heart failure.

6.5 Conclusions

Metabolic remodeling preceded the development of LVH [2]. The LVH population exhibited higher septal wall thickness and heart weight to body weight ratios compared to HTN without LVH and control patients with preserved function. Noninvasive detection of early metabolic changes may allow early aggressive therapy to prevent disease progression in hypertension induced LVH [3][4].

7 Myocardial Blood Flow Measured by ^{13}N-Ammonia Dynamic PET Imaging

7.1 Introduction

Myocardial metabolism, blood flow and contractile function of the heart are closely coupled. The heart under pressure overload exhibits impaired myocardial blood flow (MBF), with an increase in the rate of myocardial glucose uptake due to reactivation of the fetal gene program [96][97] and down regulation of contractile function and oxygen consumption [109] as an adaptive response. The myocardium can regain normal contractility once the pressure is relieved. This reversible response of myocardial tissue has been described as hibernating myocardium. However, it is not clear whether metabolic derangements in myocardial glucose metabolism is a cause or an effect of the impairment in MBF observed in the pressure overload heart [141]. The flow-metabolism mismatch during the adaptive phase is used as a diagnostic tool in clinical practice, wherein patients with a mismatch are sent for revascularization, as opposed to patients with a flow-metabolism match indicating scar tissue formation. Accurate assessment of dysfunctional but viable myocardium is important in patients with left ventricle dysfunction, especially myocardial infarction. Identification of hibernating myocardium is most valuable in those patients with the greatest impairment of left ventricle function and areas of myocardial asynergy, where revascularization improves contractility to the greatest degree and improves survival. Therefore, simultaneous assessment of impairments in myocardial metabolism and blood flow is important for earlier diagnosis and subsequent therapy to prevent cardiac dysfunction.

PET imaging provides an effective tool for assessing both absolute MBF and metabolic processes in myocardial cells from small animal models to clinical practice. Radioactive tracers such as ^{11}C-acetate [142], 82-Rubidium [143][144], ^{13}N-ammonia [145] and more recently ^{18}F-Flurpiridaz [146] are widely used for measuring myocardial perfusion in small and large animals, and also in humans. Previous measurements of MBF in rat hearts [147][148] has accounted for SP contamination from the blood to the tissue with PV correction. Some measurements in mouse hearts have performed standard uptake rate (SUV) calculations [149], which are only semi-quantitative [150]. In chapters 4 and 5 we evaluated myocardial glucose metabolism in mouse heart using FDG PET [2][84] in a 3-compartment tracer kinetic model. Quantitative measurement of MBF in mouse heart using 13N-ammonia is more challenging than measuring glucose metabolism using FDG due to the larger range of positrons emitted by ^{13}N (see table 3-1). Degradation in the system spatial resolution and the small size of mouse heart thereby results in poor quality images. Rapid heart rate results in further image blur confounding the effects of SP in the quantitative estimation of the image derived blood input function (IDBIF) [69][72][73] in a dynamic PET scan. In this chapter we measure absolute MBF in mouse heart for the first time *in vivo* using ^{13}N-ammonia dynamic PET imaging at rest and under vasodilator stress. Myocardial flow reserve (MFR) defined as the ratio of the flow under stress to that at rest was also computed. Dynamic PET data was analyzed in the modified tracer kinetic model correcting for SP and PV effects of both the blood and the tissue in a dynamic 13N-ammonia PET scan. The *in vivo* measurements were validated with the magnetic resonance imaging (MRI) measurements [151] in literature.

7.2 Measuring Absolute Myocardial Blood Flow (MBF) using a 3-Compartment Tracer Kinetic Model in Mouse Heart

7.2.1 MicroPET Imaging Protocol

Rest Imaging: PET imaging for measuring MBF was carried out using ^{13}N-ammonia in adult C57BL/6 male mice as follows: following the insertion of a tail-vein catheter, ECG surface electrodes (Blue Sensor, Ambu Inc., Glen Burnie, MD) were placed on both forepaws and the left hindpaw and a pneumatic respiratory pillow was placed on the animal's chest. 10 minute dynamic PET scan was performed under 1-1.5 % isofluorane anesthesia in oxygen [82], where data acquisition was initiated a few seconds before the slow administration of about 800 μCi ^{13}N-amonia over 30 seconds via the catheter. Small Animal Instruments, Inc., model 1025L for PET was used for continuously monitoring heart rate, respiration, and core body temperature. Transmission scan using ^{57}Co point source was done for attenuation correction prior to ^{13}N-amonia dynamic PET scan.

During Vasodilator Stress: Ten minutes after the rest scan, allowing for tracer decay time, an intravenous (i.v) bolus of Lexiscan (regadenoson, an adenosine A2a receptor agonist) was administered into the tail-vein catheter (2.5 ug/ kg in 50 uL), without disturbing the position of the mouse in the scanner. Two minutes after adenosine administration, allowing for the heart rate to increase to at least 600 bpm, a second 10 minute PET scan was initiated before the administration of 800 μCi ^{13}N-ammonia via the intravenous catheter.

The list mode data sorted into 22 time bins (12 × 5 s, 8 × 30 s, 2 × 150s) were reconstructed using OSEM-MAP algorithm [79][86] with attenuation correction. An OSEM-MAP (FastMAP) version 2.4 was used for reconstruction and the parameters were 12 OSEM-3D subsets with 2 OSEM-3D iterations, 18 MAP iterations, span 3, ring difference 47 and image resolution 1.438 mm. The reconstructed image consisted of 95 slices with 128×128 pixels and an in-plane voxel resolution of 0.4 mm × 0.4 mm, corresponding to a zoom factor of 2.164 and slice thickness of 0.8 mm. The images were corrected for radioactive decay, random coincidences and dead-time losses using the MicroPET Manager (Siemens Inc.).

7.2.2 Tracer Kinetic Model Development for Absolute MBF Measurement

Regions of interest (ROI) in the region corresponding to the LV blood pool (LVBP) and the myocardium were drawn in the last frame of the dynamic image data and time activity curves for the LVBP and the myocardium were generated for the entire scan duration of 10 minutes.

Based on the 3-compartment model, the differential equations for ^{13}N-ammonia kinetics in terms of the rate constants shown in Figure 7-1 can be written as follows:

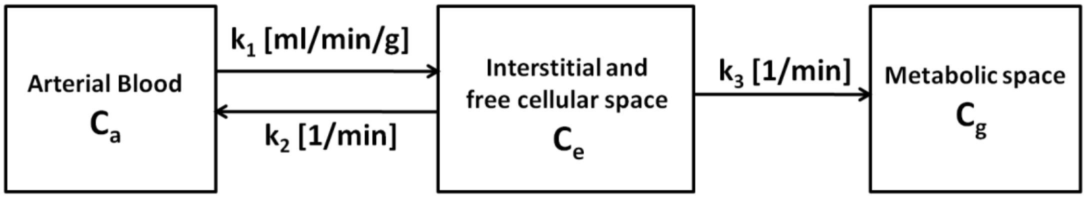

Figure 7-1 The schematic block diagram of 3-compartment myocardial blood flow model.

$$\begin{cases} \dfrac{dC_e(t)}{dt} = \rho k_1 C_a(t) - (k_2 + k_3) C_e(t) \\ \dfrac{dC_g(t)}{dt} = k_3 C_e(t) \end{cases} \tag{7-1}$$

$$C_t = C_e + C_g = \frac{\rho k_1}{k_2 + k_3} \times [k_3 + k_2 e^{-(k_2+k_3)t}] \otimes C_a(t) \tag{7-2}$$

where, k_1 (ml/ min/ g) is absolute MBF, ρ=1.04 g/ ml is the myocardial tissue density. The model equation for the blood input function can be written as [89]:

$$C_a = \begin{cases} 0, if\ t < \tau \\ [A_1(t-\tau) - A_2] e^{L_1(t-\tau)} + A_2 e^{L_2(t-\tau)}, otherwise \end{cases} \tag{7-3}$$

However, due to SP and PV effects, the model equations for an image-derived time activity curve from the blood pool and the myocardium can be written in terms of fraction of the tissue concentration in the blood compartment and partial recovery of radioactivity concentration from the blood and vice-versa as:

$$\begin{cases} Model_{IDBIF,i} = \dfrac{\int_{t_b^i}^{t_e^i} [S_{mb}(C_e(t) + C_g(t)) + r_b C_a] dt}{t_e^i - t_b^i} \\ Model_{myo,i} = \dfrac{\int_{t_b^i}^{t_e^i} [r_m(C_e(t) + C_g(t)) + S_{bm} C_a] dt}{t_e^i - t_b^i} \end{cases} \tag{7-4}$$

where, r_m, r_b, are the recovery coefficients (accounting for PV effect) for the myocardium and blood pool respectively. S_{bm}, S_{mb} are the SP coefficients from the blood pool to the myocardium and vice versa respectively. t_b^i *and* t_e^i are the beginning and end times for a single frame in a dynamic PET scan. Optimization of the model equations to the time activity curves obtained from the dynamic PET image was performed by minimizing the objective function in MATLAB using “fmincon”, which is based on an interior-reflective Newton method [1][80]:

$$O(p) = \sum_{i=1}^{n} [(Model_{IDBIF,i} - PET_{IDBIF,i})^2 + (Model_{myo,i} - PET_{myo,i})^2] \qquad \textbf{7-5}$$

where, PET_{IDBIF} is image derived blood input function (blood pool time-activity concentration), PET_{myo} is myocardium time-activity concentration obtained from PET image and p is the parameter vector including the SP and PV coefficients. MFR was computed as the ratio of the flow under vasodilator stress to the flow at rest as follows:

$$MFR = \frac{MBF_{stress}}{MBF_{rest}} \qquad \textbf{7-6}$$

Myocardial blood flow with ^{13}N-ammonia PET imaging *in vivo* in mouse heart at rest was obtained using the methodology described in the methods section. Figure 7-2(A-D) exhibits the dynamic PET images at various time points in a dynamic PET scan of mouse heart *in vivo*. Figure 7-2 E shows the model fits obtained using the formalism discussed in the methods section.

Absolute MBF at rest was measured to be 4.8 mL/ min/g. This compares well with the existing literature for measuring MBF in mouse heart at rest with quantitative first-pass [152] and arterial spin-labeling MRI [151]. Absolute MBF under vasodilator stress obtained from the second PET was 8.9 mL/ min/ g. The MFR in mouse heart was hence computed to be 1.9 (Flow at stress/Flow at rest).

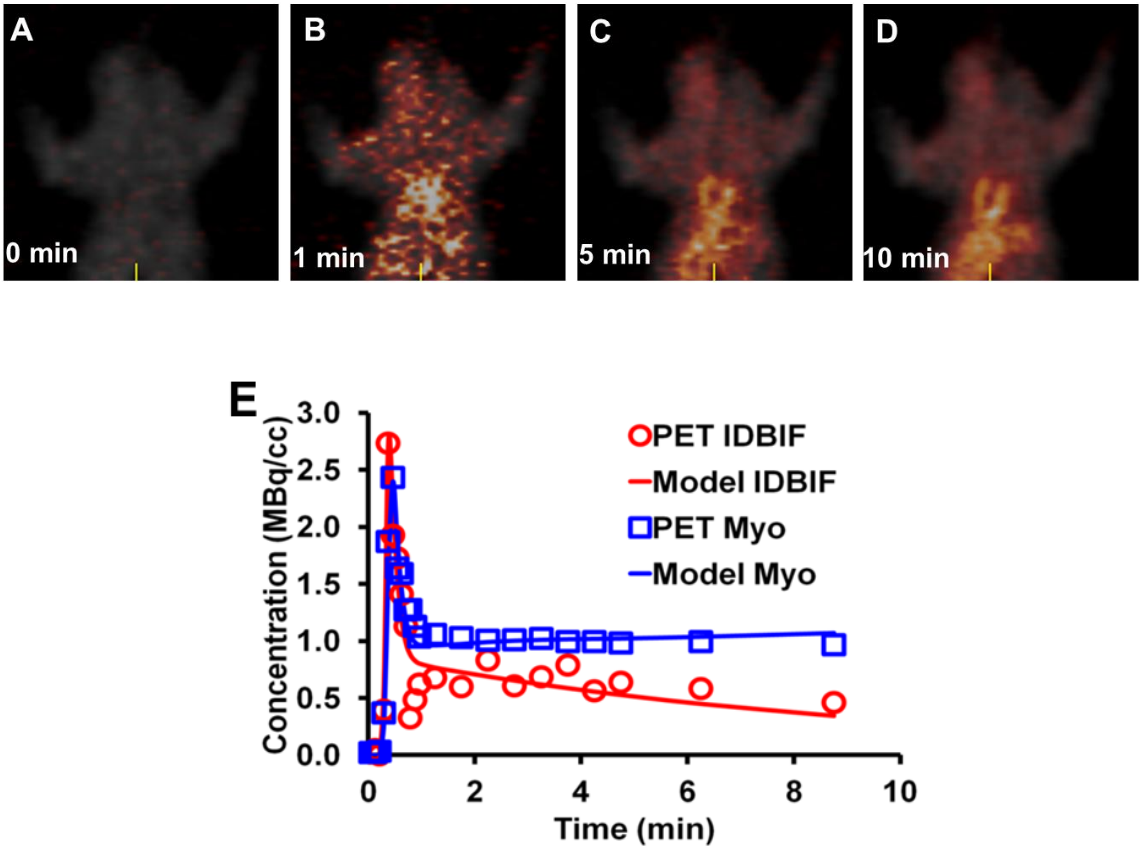

Figure 7-2 Dynamic ^{13}N-ammonia PET imaging *in vivo* in mouse heart and model fits at rest. (A-D) Example fused dynamic PET images at pre, at early and late time points post ^{13}N-NH$_3$ injection over a scan time of 10 minutes. (E) Model fits of the tissue and blood time activity curves obtained from PET images.

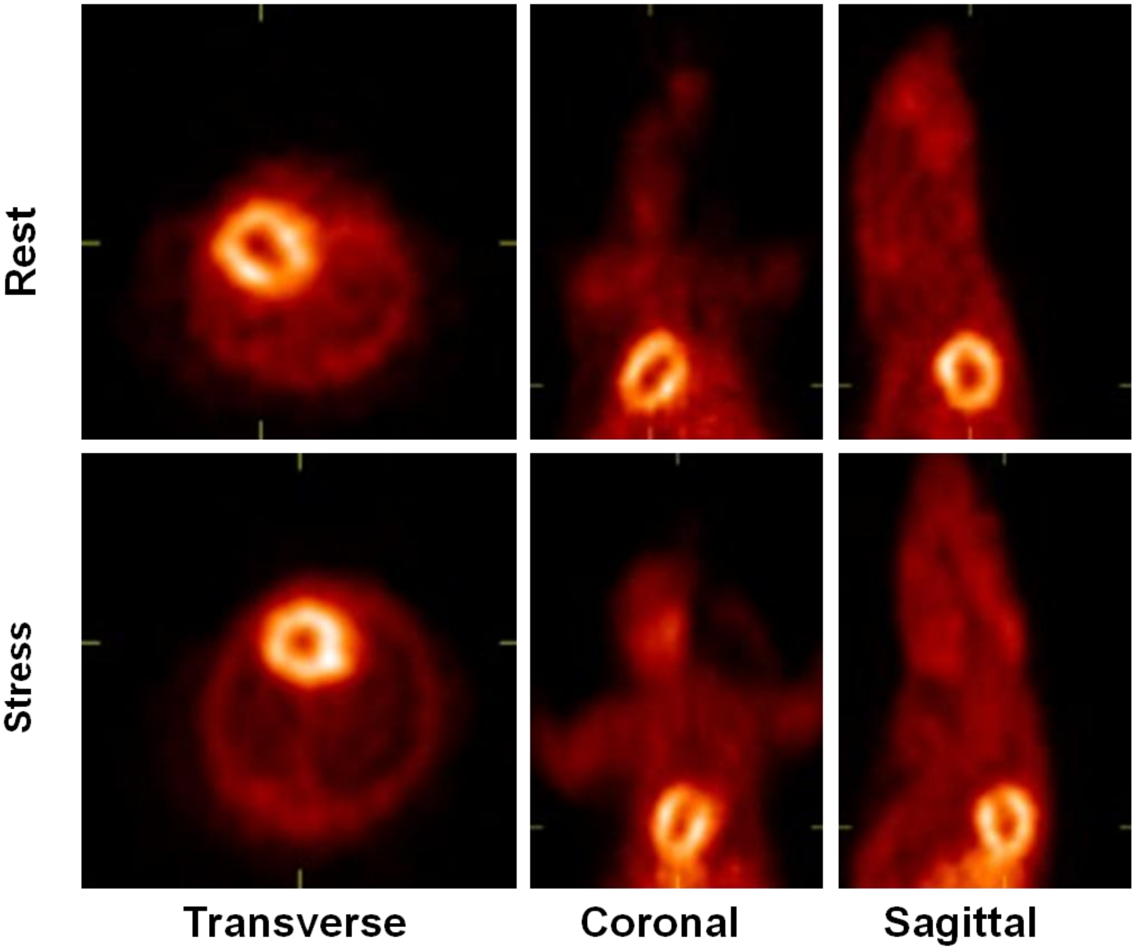

Figure 7-3 ^{13}N-ammonia PET images of mouse heart at rest and during vasodilator stress (regadenoson, 2.5 ug/kg in 50 uL) *in vivo*.

7.3 Measuring Absolute MBF and glucose metabolism mismatch in a TAC Mouse Model

The preliminary study in the control mouse heart showed the feasibility of using ^{13}N-ammonia quantitative dynamic PET imaging for absolute MBF measurement. In this section, we established a correlation between absolute MBF and glucose metabolism in a stressed mouse heart for the first time *in vivo*. Stress in the mouse heart was created following the same surgical protocol described in section 5.2. Dynamic 13N-ammonia PET imaging followed by FDG PET imaging was performed 1 day after the surgery.

7.3.1 MicroPET Imaging Protocol

A 10 minutes transmission scan using ^{57}Co point source was done for attenuation correction prior to ^{13}N-amonia dynamic PET scan. PET imaging for measuring MBF was carried out using ^{13}N-ammonia on adult C57BL/6 male mice as follows: following the insertion of a tail-vein catheter, ECG surface electrodes (Blue Sensor, Ambu Inc., Glen Burnie, MD) were placed on both forepaws and the left hindpaw and a pneumatic respiratory pillow was placed on the animal's chest. 10 minutes dynamic PET scan was performed under 1-1.5 % isofluorane anesthesia in oxygen [82], where data acquisition was initiated a few seconds before the slow administration of about 800 µCi ^{13}N-amonia over 30 seconds via the catheter. 10 minutes after the rest scan, allowing for ^{13}N-ammonia tracer decay time, 60 minutes dynamic PET imaging for glucose metabolism was carried out using ^{18}F-FDG on the same mouse without disturbing mouse position in the MircroPET scanner. Data acquisition was initiated few seconds before the slow administration of 800 µCi ^{18}F-FDG via the same tail-vein catheter. Small Animal Instruments, Inc., model 1025L for PET was used for continuously monitoring heart rate, respiration, and core body temperature. Cardiac gate signals generated at the end-expiration phase of the respiratory cycle, using the small animal gating system, were used to trigger the PET scanner only in dynamic FDG PET imaging. The time stamped list mode PET data was then retrospectively arranged into 23 time bins and 3 cardiac phases per time bin [83]. The list mode data of ^{13}N-ammonia scan sorted into 22 time bins (12 × 5 s, 8 × 30 s, 2 × 150s), and the list mode data of ^{18}F-FDG PET scan sorted into 23 time bins (11 × 8 s, 1 × 12 s, 2 × 60 s, 1 × 180 s, and 8 × 400 s) [1][79][84]. An OSEM-MAP (FastMAP) version 2.4 was used for reconstruction and the parameters were 12 OSEM-3D subsets with 2 OSEM-3D iterations, 18 MAP iterations, span 3, ring difference 47 and image resolution 1.438 mm. The reconstructed image consisted of 95 slices with 128×128 pixels and an in-plane voxel resolution of 0.4 mm × 0.4 mm, corresponding to a zoom factor of 2.164 and slice thickness of 0.8 mm.

7.3.2 Left Ventricle Segmentation Analysis

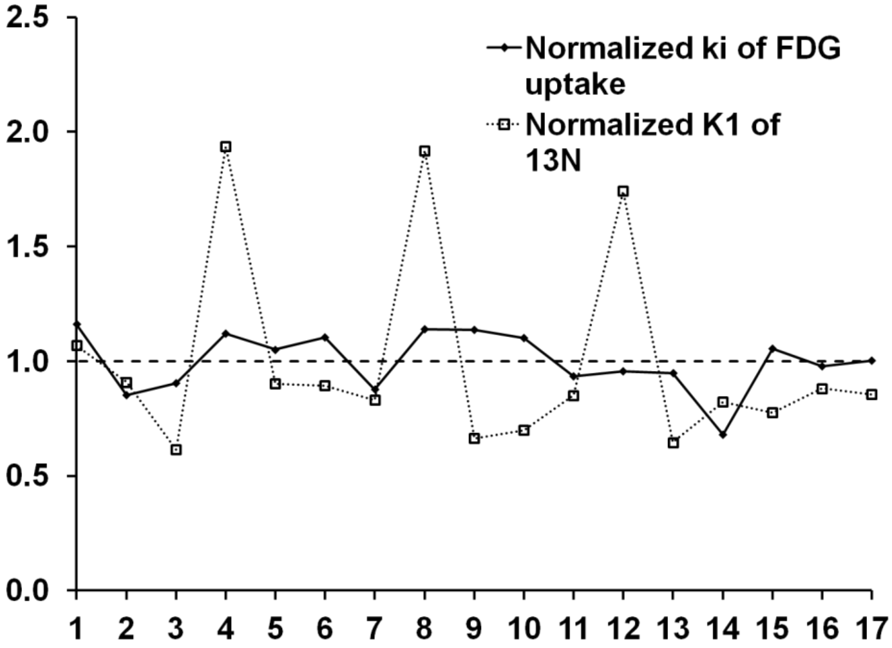

Figure 7-4 Left ventricle segmentation analysis for metabolism and perfusion

For the identification of blood flow and metabolism mismatch, regions of interest were determined by following the standardized left ventricle segmentation described by Manuel D. Cerqueira et al [153]. Tracer kinetic models developed for MBF (section 7.2.2) and glucose metabolism (section 3.3) were used for processing total 17 left ventricle segmentations from basal to apex. Absolute MBF K_1 and myocardial glucose uptake rate ki were calculated for each segment, then normalized by average number over the entire left ventricle myocardium. Figure 7-4 indicates blood flow and glucose metabolism mismatch in segments 5, 6, 9, 10, 12 and 15, and match in the remaining segments.

This is the first time that using dynamic PET imaging we have established a correlation between absolute MBF and myocardial glucose metabolism in mouse heart *in vivo*. The preliminary results showed an increase in glucose uptake rate (global average ki =0.18 mL/ g/ min) and impaired blood flow (global average k_1 = 3.2 mL/ min/ g) in the heart, as an adaptive response to acute pressure overload surgery on day 1.

7.4 Discussion

The correction for ^{13}N-ammonia metabolites in blood would further improve the quantitative accuracy of MBF estimate in mouse heart at rest and under stress [5]. It is expected that with improved tracer kinetic modeling techniques, we can characterize the alteration of flow and metabolism with function in the mouse heart subject to pressure overload LVH serially over a time course *in vivo*.

The one mouse heart, subjected to TAC induced LVH, 17 segmentation analysis showed the feasibility to monitor MBF and myocardial glucose metabolism by applying advanced tracer kinetic models following serial dynamic ^{13}N-ammonia and ^{18}F-FDG PET imaging *in vivo*. Further studies of interventions at early and late time points will test the hypothesis *in vivo* that derangements in myocardial glucose metabolism possibly triggers impairment in MBF and contractile dysfunction in the pressure overload mouse heart.

In summary, the results from these preliminary studies are of interest because they will advance the field of dynamic cardiac PET imaging of MBF in the mouse heart. A translation of the PET imaging and quantification methods, developed and optimized in mice, to the clinical scenario may lead to the development of fundamental knowledge in myocardial perfusion and better understanding in its correlation with metabolic alterations on subsequent cardiac function in human heart, which may help reduce cardiovascular morbidity and mortality in patients with hypertension.

7.5 Conclusions

In this chapter we developed a 3-compartment tracer kinetic model to quantitatively assess blood flow and flow reserve in mouse heart using ^{13}N-ammonia dynamic PET imaging *in vivo*. Preliminary data indicated a correlation between blood flow and glucose metabolism in the stressed mouse heart *in vivo*.

8 Conclusion and Future Work

8.1 Research Summary

The objective of this dissertation is to develop and validate tracer kinetic models for evaluation of metabolism and perfusion in the heart *in vivo*, with correction for incomplete radioactivity recovery and spillover contamination. Using this advanced quantitative model in conjunction with optimized PET imaging technique, efforts were also made to explore the model as a tool for early detection and therapy planning.

Quantification of dynamic FDG PET imaging of the heart was extensively studied from mouse to man. MCBIF applied to OSEM-MAP gated images correctly accounts for the shape, wash-in and wash-out dynamics of FDG from mouse blood without the need of any invasive blood sampling. Lower SP of radioactivity from the myocardium to the BP and higher PV recovery from OSEM-MAP gated images lead to improved MCBIF estimate as compared to that obtained from un-gated FBP images in a dynamic PET scan of the mouse heart. We demonstrated that MCBIF applied to an IDIF obtained from high resolution gated images with less severe SP and PV effects is quantitative and also repeatable as compared to that obtained from low resolution un-gated images [80].

In the mouse heart of left ventricle hypertrophy, quantification of metabolism was studied in an acute mouse model. Non-invasive serial dynamic FDG imaging of the mouse heart subjected to TAC surgery induced hypertrophy supports the hypothesis that changes in glucose analogue FDG metabolism in the form of enhanced uptake of FDG by the myocardium in mice precedes and triggers the onset of severe cardiac dysfunction in LVH. Early intervention with a standard of care treatment prevented maladaptive response and rescued cardiac function. We speculate that early detection of metabolic remodeling may offer a metabolic target for modulation of hypertrophy.

Although clinically relevant, the acute nature of the model may be a limitation in evaluating the hypothesis of metabolic remodeling preceding and triggering cardiac dysfunction in LVH, which makes it difficult to distinguish the maladaptive from the adaptive metabolic response and thereby to identify the window for aggressive therapeutic strategies that improve outcome which then could be readily translated to clinical practice. In the first-in-human clinical study, adapting the dynamic FDG PET imaging and quantitative techniques developed in mouse heart, it was observed that metabolic remodeling precedes any structural and functional remodeling in hypertension induced LVH patients. The LVH population exhibited higher septal wall thickness and heart weight to body weight ratios compared to HTN without LVH and control patients with preserved function. Noninvasive detection of early metabolic changes may allow early aggressive therapy to prevent disease progression in hypertension induced LVH.

Simultaneous assessment of impairments in myocardial metabolism and blood flow is important for earlier diagnosis and subsequent therapy to prevent cardiac dysfunction. Preliminary efforts were made into exploring quantitative assessment of absolute blood flow in mouse heart using dynamic ^{13}N-ammonia imaging in a 3-compartment tracer kinetic model. The modified 3-compartment tracer kinetic model for myocardial blood flow can quantitatively measure absolute MBF and MFR in mouse heart using 13N-ammonia dynamic PET imaging *in vivo*.

8.2 Future Work

The simultaneous assessments of metabolism and perfusion play an important role in diagnosis and treatment planning. The preliminary study showed feasibility of using optimized tracer kinetic model in dynamic ^{13}N-ammonia imaging for absolute myocardial blood flow measurement. To validate the parametric model, future work including collecting at least n = 5 control mice ^{13}N-ammonia imaging data, and comparing with gold standard microsphere measurements *ex vivo* are necessary. However, the surgery for microsphere measurement preparation in mouse may be very difficult. As an alternative method, cross-validation between dynamic PET imaging and a different modality such as arterial spin labeling (ASL) MRI also can help address this issue.

Following validation of measuring absolute blood flow in mouse heart, non-invasive serial imaging can be performed on n = 5 stressed mice (using a similar surgical protocol described in chapter 5) over a period of 7 days using dynamic ^{13}N-ammonia and FDG PET in a 3-compartment kinetic model for identification of hibernating myocardium and to establish a correlation between flow and metabolism *in vivo*. These imaging data can then be compared to control data by imaging n=5 sham mice.

In summary, the 3-compartment tracer kinetic model showed good adaptability when translating from mouse to humans, and also when switching from measuring glucose metabolism to absolute blood flow in the heart. The kinetic models developed in this dissertation can also be adapted to different PET tracers such as acetate for measuring oxygen consumption *in vivo* [154]. The kinetic rate constants and compartments can be adjusted to adapt to different metabolic processes for different tracers, while the form of the equations of model corrected image-derived heart ventricle and image-derived tissue time activity would have a similar form. Also, the initial values and optimization bounds should be modified when switching to other tracers or animal models. In addition, blood samples from a number of experimental subjects may be necessary to validate model output estimates. Nevertheless, application of this technique to other scanners and isotopes would require careful validation since positron range and depth of interaction will be different for other isotopes and scanners.

Reference

[1] Zhong M, Kundu B K. Optimization of a model corrected blood input function from dynamic FDG-PET images of small animal heart in vivo, *IEEE Trans Nucl Sci.*, Oct 2013;160(5): 3417-3422.

[2] Zhong M, Alonso C E, Taegtmeyer H, Kundu BK. Quantitative PET imaging detects early metabolic remodeling in a mouse model of pressure-overload left ventricular hypertrophy in vivo. *Journal of Nuclear Medicine*, 2013, 54(4): 609-615.

[3] Zhong M, Hamirani Y, Bourque J, Kundu BK. Non-invasive detection of early metabolic remodeling in left ventricular hypertrophy. Late Breaking Abstract, *World Molecular Imaging Congress*, Savannah, Georgia, 2013.

[4] Hamirani Y*, Zhong M*, McBride A, Bourque J, Kundu BK. Myocardial Metabolic Remodeling in Hypertension Induced Left Ventricular Hypertrophy. Abstract, Best poster, American College of Cardiology (ACC) Meeting, Washington DC, April 2014. *equal contribution.

[5] Zhong M, Mistry M, Dimastromatteo J, Taegtmeyer H, Glover D, Kundu B. PET imaging of myocardial blood flow in the stressed mouse heart in vivo. *J NUCL MED MEETING ABSTRACTS* 2013 54: 1635.

[6] Freudenrich C, How Nuclear Medicine Works, *HowStuffWorks.com*, 2000.

[7] National Research Council (US) and Institute of Medicine (US) Committee on State of the Science of Nuclear Medicine. Advancing Nuclear Medicine Through

Innovation. *Washington (DC): National Academies Press (US);* 2007. 3, Nuclear Medicine Imaging in Diagnosis and Treatment.

[8] Moon D H, Maddahi J, Silverman D H, et al. Accuracy of whole-body fluorine-18-FDG PET for the detection of recurrent or metastatic breast carcinoma. *Journal of nuclear medicine*, 1998, 39(3): 431-435.

[9] Ntziachristos V, Ripoll J, Wang L V, et al. Looking and listening to light: the evolution of whole-body photonic imaging. *Nature biotechnology*, 2005, 23(3): 313-320.

[10] Huh W K, Falvo J V, Gerke L C, et al. Global analysis of protein localization in budding yeast. *Nature*, 2003, 425(6959): 686-691.

[11] Hoh C K, Hawkins R A, Glaspy J A, et al. Cancer detection with whole-body PET using 2-[18F] fluoro-2-deoxy-D-glucose. *Journal of computer assisted tomography,* 1993, 17(4): 582-589.

[12] Mart íBonmat íL, Sopena R, Bartumeus P, et al. Multimodality imaging techniques. Contrast media & molecular imaging, 2010, 5(4): 180-189.

[13] Massoud T F, Gambhir S S. Molecular imaging in living subjects: seeing fundamental biological processes in a new light. *Genes & development*, 2003, 17(5): 545-580.

[14] Prescher J A, Bertozzi C R. Chemistry in living systems. *Nature chemical biology*, 2005, 1(1): 13-21.

[15] Rahmim A, Zaidi H. PET versus SPECT: strengths, limitations and challenges. *Nuclear medicine communications*, 2008, 29(3): 193-207.

[16] Boellaard R. Standards for PET image acquisition and quantitative data analysis. *Journal of nuclear medicine*, 2009, 50(Suppl 1): 11S-20S.

[17] Levin C S, Hoffman E J. Calculation of positron range and its effect on the fundamental limit of positron emission tomography system spatial resolution. *Physics in Medicine and Biology*, 1999, 44(3): 781.

[18] Evans R D, Noyau A. The atomic nucleus. *New York: McGraw-Hill*, 1955.

[19] Ter-Pogossian M M, Phelps M E, Hoffman E J, et al. A Positron-Emission Transaxial Tomograph for Nuclear Imaging (PETT) 1. *Radiology*, 1975, 114(1): 89-98.

[20] Ter-Pogossian M M. Positron emission tomography (PET). *Diagnostic Imaging in Medicine*, 1983: 273-277.

[21] Griffiths D J. Introduction to Elementary Particles. *Wiley*, 1987.

[22] Berends F A, Kleiss R. Distributions for Electron-Positron Annihilation into two and three Photons. *Nuclear Physics B*, 1981, 186(1): 22-34.

[23] Phelps M E. PET: molecular imaging and its biological applications. *Springer*, 2004.

[24] Phelps M E, Hoffman E J, Mullani N A, et al. Application of annihilation coincidence detection to transaxial reconstruction tomography. *Journal of nuclear medicine*, 1975, 16(3): 210-224.

[25] Derenzo S E. Precision measurement of annihilation point spread distributions for medically important positron emitters. *Proceeding of the 5th International Conference on Positron Annihilation*, Lake Yamanaka, Japan, April 8-11, 1979.

[26] Phelps M E. PET: physics, instrumentation, and scanners. *Springer*, 2006.

[27] Frackowiak R. Positron Emission Tomography and Autoradiography: principles and applications for the brain and heart. *Journal of neurology, neurosurgery, and psychiatry*, 1986, 49(7): 848.

[28] Bell R E, Graham R L, Petch H E. Design and use of a coincidence circuit of short resolving time. *Canadian Journal of Physics*, 1952, 30(1): 35-52.

[29] Sorenson J A, Phelps M E, Cherry S R. Physics in nuclear medicine. *Saunders*, 1987.

[30] Ter-Pogossian M M, Mullani N A, Ficke D C, et al. Photon time-of-flight-assisted positron emission tomography. *Journal of computer assisted tomography*, 1981, 5(2): 227-239.

[31] Birks, J B. The theory and practice of scintillation counting. *Pergamon Press*, 1964.

[32] Knoll G F. Radiation detection and measurement. *John Wiley & Sons*, 2010.

[33] Steén M, Uhlén P. Development of a Time-of-Flight and 3D Demonstration Set-up for Positron Emission Tomography. PhD thesis, *The Royal Institute of Technology Stockholm*, 1998.

[34] Badawi R D, Marsden P K, Cronin B F, et al. Optimization of noise-equivalent count rates in 3D PET. *Physics in medicine and biology*, 1996, 41(9): 1755.

[35] L'Annunziata M F. Handbook of radioactivity analysis. *Academic press*, 1998.

[36] Dahlbom M, MacDonald L R, Eriksson L, et al. Performance of a YSO/LSO phoswich detector for use in a PET/SPECT system. *Nuclear Science, IEEE Transactions on*, 1997, 44(3): 1114-1119.

[37] Ficke D C, Hood J T, Ter-Pogossian M M. A spheroid positron emission tomograph for brain imaging: a feasibility study. *Journal of Nuclear Medicine*, 1996, 37(7): 1219-1225.

[38] Bailey D L. Quantification in 3D positron emission tomography. PhD thesis, *University of Surrey*, 1996.

[39] Jadvar H, Parker J A. Clinical PET and PET/CT. *Springer*, 2005.

[40] Casey M E, Nutt R. A multicrystal two dimensional BGO detector system for positron emission tomography. *Nuclear Science, IEEE Transactions on*, 33(1),460-463, 1986.

[41] Casey ME, An Analysis of Counting Losses in Positron Emission Tomography PhD Thesis, *University of Tennessee*, 1992.

[42] Anger H O. Scintillation Camera. *Review of Scientific Instruments*, 1958, 29(1): 27-33.

[43] Fahey F H. Data acquisition in PET imaging. *Journal of nuclear medicine technology*, 2002, 30(2): 39-49.

[44] Liow J-S, Strother SC. Normalisation using rotating rods for 3D PET, *Proceedings of the 3rd International Meeting on Fully Three-Dimensional Image Reconstruction in Radiology and Nuclear Medicine*, Aix-les-Bains, France, 1995.

[45] Hoffman E J, Guerrero T M, Germano G, et al. PET system calibrations and corrections for quantitative and spatially accurate images. *Nuclear Science, IEEE Transactions on*, 1989, 36(1): 1108-1112.

[46] Casey M E, Gadagkar H, Newport D. A component based method for normalization in volume PET. *Proceedings of the 3rd International Meeting on*

Fully Three-Dimensional Image Reconstruction in Radiology and Nuclear Medicine, Aix-les-Bains, France, 1996.

[47] Badawi R D, Lodge M A, Marsden P K. Algorithms for calculating detector efficiency normalization coefficients for true coincidences in 3D PET. *Physics in medicine and biology*, 1998, 43(1): 189.

[48] Thompson C J, Dagher A, Lunney D N, et al. A technique to reject scattered radiation in PET transmission scans, *Physics and Engineering of Computerized Multidimensional Imaging and Processing. International Society for Optics and Photonics*, 1986: 244-253.

[49] Xu M, Cutler P D, Luk W K. Adaptive, segmented attenuation correction for whole-body PET imaging. *Nuclear Science, IEEE Transactions on*, 1996, 43(1): 331-336.

[50] Tarantola G, Zito F, Gerundini P. PET instrumentation and reconstruction algorithms in whole-body applications. *Journal of Nuclear Medicine*, 2003, 44(5): 756-769.

[51] Ollinger J M. Model-based scatter correction for fully 3D PET. *Physics in medicine and biology*, 1996, 41(1): 153.

[52] Watson C C, Newport D, Casey M E. A single scatter simulation technique for scatter correction in 3D PET, Three-dimensional image reconstruction in radiology and nuclear medicine. *Springer,* 1996: 255-268.

[53] Weinberg S. The quantum theory of fields. *Cambridge university press,* 1996.

[54] Stearns CW. Scatter correction method for 3D PET using 2D fitted Gaussian functions. *Journal of Nuclear Medicine*. 36 105P, 1995.

[55] Cherry S R, Huang S C. Effects of scatter on model parameter estimates in 3D PET studies of the human brain. *Nuclear Science, IEEE Transactions on*, 1995, 42(4): 1174-1179.

[56] Cooke B E, Evans A C, Fanthome E O, et al. Performance figures and images from the Therascan 3128 positron emission tomograph. *Nuclear Science, IEEE Transactions on*, 1984, 31(1): 640-644.

[57] Leo W R. Techniques for nuclear and particle physics experiments: a how-to approach. *Springer*, pp. 122–127. 1994.

[58] Sharma A, Walker J G. Paralyzable and nonparalyzable deadtime analysis in spatial photon counting. *Review of scientific instruments*, 1992, 63(12): 5784-5793.

[59] Phelps M E, Hoffman E J, Huang S C, et al. Effect of positron range on spatial resolution. *Journal of nuclear medicine*. 1975, 16(7): 649-652.

[60] Raylman R R, Hammer B E, Christensen N L. Combined MRI-PET scanner: a Monte Carlo evaluation of the improvements in PET resolution due to the effects of a static homogeneous magnetic field. *Nuclear Science, IEEE Transactions on*, 1996, 43(4): 2406-2412.

[61] Harrison R L, Kaplan M S, Vannoy S D, et al. Positron range and coincidence non-collinearity in SimSET, *Nuclear Science Symposium, 1999. Conference Record. 1999 IEEE*. IEEE, 1999, 3: 1265-1268.

[62] Hoffman E J, Huang S C, Phelps M E. Quantitation in positron emission computed tomography: 1. Effect of object size. *Journal of computer assisted tomography*, 1979, 3(3): 299-308.

[63] Soret M, Bacharach S L, Buvat I. Partial-volume effect in PET tumor imaging. *Journal of Nuclear Medicine*, 2007, 48(6): 932-945.

[64] Morris E D, Endres C J, Schmidt K C, et al. Kinetic modeling in positron emission tomography. *Emission Tomography: The Fundamentals of PET and SPECT*. Academic, San Diego, 2004.

[65] Carson R E. Tracer kinetic modeling in PET. *Positron Emission Tomography: Basic Sciences*, 2005: 127-159.

[66] Watabe H, Ikoma Y, Kimura Y, et al. PET kinetic analysis—compartmental model. *Annals of nuclear medicine*, 2006, 20(9): 583-588.

[67] Phelps M E, Huang S C, Hoffman E J, et al. Tomographic measurement of local cerebral glucose metabolic rate in humans with (F‐18) 2‐fluoro‐2‐deoxy‐D‐glucose: validation of method. *Annals of neurology*, 1979, 6(5): 371-388.

[68] Sadato N, Tsuchida T, Nakaumra S, et al. Non-invasive estimation of the net influx constant using the standardized uptake value for quantification of FDG uptake of tumours. *European journal of nuclear medicine*, 1998, 25(6): 559-564.

[69] Pain F, Lanièce P, Mastrippolito R, et al. Arterial input function measurement without blood sampling using a beta-microprobe in rats. *Journal of Nuclear Medicine*, 2004;45(9):1577-82.

[70] Tai YC, Chatziioannou AF, Yang Y, et al. MicroPET II: design, development and initial performance of an improved microPET scanner for small-animal imaging, Physics in Medicine and Biology 2003;48:1519-1537.

[71] Laforest R, Longford D, Siegel S, et al. Performance evaluation of the microPET®—FOCUS-F120, *Nuclear Science, IEEE Transactions on,*. 2007;54:42-49.

[72] Laforest R, Sharp TL, Engelbach JA, et al. Measurement of input functions in rodents: challenges and solutions, *Nuclear Medicine and Biology*. 2005;32:679-685.

[73] Wu HM, Sui G, Lee CC, Prins ML, Ladno W, et al. In vivo quantitation of glucose metabolism in mice using small-animal PET and a microfluidic device, *Journal of Nuclear Medicine.* 2007 May;48(5):837-45.

[74] Shoghi KI, Welch MJ, Hybrid image and blood sampling input function for quantification of small animal dynamic PET data, *Nuclear Medicine and Biology.* 2007 Nov;34(8):989-94.

[75] Kim J, Herrero P, Sharp T, et al, Minimally invasive method of determining blood input function from PET images in rodents, *Journal of Nuclear Medicine.* 2006 Feb;47(2):330-6.

[76] El Fakhri G, Sitek A, Guérin B, Kijewski MF, Di Carli MF, Moore SC. Quantitative dynamic cardiac 82Rb PET using generalized factor and compartment analyses, *Journal of Nuclear Medicine.* 2005 Aug;46(8):1264-71.

[77] Stout D, Kreissl MC, Wu HM, Schelbert HR, Huang SC, Left ventricular blood TAC quantitation with microPET imaging in mice using MAP, FBP and blood sampling, *Nuclear Science Symposium Conference Record, 2005 IEEE,* Volume: 5, Page(s): 2529-2531.

[78] Cheng JC, Shoghi K, Laforest R, Quantitative accuracy of MAP reconstruction for dynamic PET imaging in small animals, *Medical Physics*. 2012; 39:1029-41.

[79] Locke LW, Berr SS, Kundu BK, Image-derived input function from cardiac gated maximum a posteriori reconstructed PET images in mice, *Molecular Imaging and Biology*. 2011;13:342-347.

[80] Fang Y H D, Muzic R F. Spillover and partial-volume correction for image-derived input functions for small-animal 18F-FDG PET studies. *Journal of Nuclear Medicine*, 2008, 49(4): 606-614.

[81] Lee KH, Ko BH, Paik JY, et al. Effects of anesthetic agents and fasting duration on F-18-FDG biodistribution and insulin levels in tumor-bearing mice, *Journal of Nuclear Medicine.* 2005;46:1531-1536.

[82] Flores JE, McFarland LM, Vanderbilt A, et al. The effects of anesthetic agent and carrier gas on blood glucose and tissue uptake in mice undergoing dynamic FDG-PET imaging: sevoflurane and isoflurane compared in air and in oxygen, *Molecular Imaging and Biology*. 2008;10:192-200.

[83] Yang Y, Rendig S, Siegel S, et al, Cardiac PET imaging in mice with simultaneous cardiac and respiratory gating, *Physics in Medicine and Biology* 2005;50:2979-2989.

[84] Locke LW, Williams MB, Fairchild KD, Zhong M, Kundu BK, Berr SS. FDG-PET Quantification of Lung Inflammation with Image-Derived Blood Input Function in Mice, *International Journal of Molecular Imaging*. 2011;2011:356730.

[85] Zhou Z, Kozlowski J, Goodrich A L, et al, Molecular imaging of lung glucose uptake after endotoxin in mice, *American Journal of Physiology*, vol. 289, no. 5, pp. L760–L768, 2005.

[86] Qi JY, Leahy RM, Cherry SR, et al, High-resolution 3D Bayesian image reconstruction using the microPET small-animal scanner, *Physics in Medicine and Biology* 1998;43:1001-1013.

[87] Sen S, Kundu B K, Wu H C J, et al. Glucose regulation of load - induced mTOR signaling and ER stress in mammalian heart. *Journal of the American Heart Association*, 2013, 2(3): e004796.

[88] Krivokapich J, Huang SC, Phelps ME, et al., Estimation of rabbit myocardial metabolic rate for glucose using fluorodeoxyglucose. *American Journal of Physiology*, 243(6):H884-H895.. Dec. 1982.

[89] Feng D, Huang SC, Wang X., Models for computer simulation studies of input functions for tracer kinetic modeling with positron emission tomography, *International Journal of Bio-Medical Computing*. 1993; 32, 95-110.

[90] Sharp TL, Dence CS, Engelbach JA, et al., Techniques necessary for multi-tracer quantitative small-animal imaging studies, *Nuclear Medicine and Biology*. 2005;32:875-884.

[91] Tantawy MN, Peterson TE, Simplified [18F]FDG image-derived input function using the left ventricle, liver, and one venous blood sample, *Molecular Imaging*. 2010;9:76-86.

[92] Chen BB, Metzler SD, Lemaire A et al. Left ventricular functional assessment in mice: feasibility of high spatial and temporal resolution ECG-gated blood pool SPECT, *Radiology*. 2007; 245:440-448

[93] Convert L, Morin-Brassard G, Cadorette J, et al., A new tool for molecular imaging: the microvolumetric beta blood counter, *Journal of Nuclear Medicine.* 2007;48:1197–1206.

[94] Bishop SP, Altschuld RA. Increased glycolytic metabolism in cardiac hypertrophy and congestive failure. *Am J Physiol*. 1970;218:153-159.

[95] Taegtmeyer H, Overturf ML. Effects of moderate hypertension on cardiac function and metabolism in the rabbit. *Hypertension*. 1988;11:416-426.

[96] Taegtmeyer H, Golfman L, Sharma S, et al. Linking gene expression to function: Metabolic flexibility in the normal and diseased heart. *Ann N Y Acad Sci*. 2004;1015:202-213.

[97] Taegtmeyer H, Sen S, Vela D. Return to the fetal gene program: a suggested metabolic link to gene expression in the heart. *Ann N Y Acad Sci*. 2010;1188:191-198.

[98] Liao YL, Ishikura F, Beppu S, et al. Echocardiographic assessment of LV hypertrophy and function in aortic-banded mice: necropsy validation. *Am J Physiol. Heart Circ Physiol*. 2002;282:H1703-H1708.

[99] Hariharan R, Bray M, Ganim R, et al. Fundamental limitations of [18F]2-deoxy-2-fluoro-D-glucose for assessing myocardial glucose uptake. *Circulation*. 1995;91:2435-2444.

[100] Botker HE, Bottcher M, Schmitz O, et al. Glucose uptake and lumped constant variability in normal human hearts determined with [F-18]fluorodeoxyglucose. *J Nucl Cardiol*. 1997;4:125-132.

[101] Ng CK, Holden JE, Degrado TR, et al. Sensitivity of myocardial fluorodeoxyglucose lumped constant to glucose and insulin. *Am J Physiol*. 1991;260:H593-H603.

[102] Katsuji Hashimoto. Lumped constant for deoxyglucose is decreased when myocardial glucose uptake is enhanced. *Am J Physiol*. *Heart Circ Physiol.* 1999; 276, 129-133.

[103] Shoghi KI, Gropler RJ, Sharp T, et al. Time course of alterations in myocardial glucose utilization in the Zucker diabetic fatty rat with correlation to gene expression of glucose transporters: a small-animal PET investigation. *J Nucl Med*. 2008;49:1320-1327.

[104] Shoghi KI, Finck BN, Schechtman KB, et al. In vivo metabolic phenotyping of myocardial substrate metabolism in rodents: differential efficacy of metformin and rosiglitazone monotherapy. *Circ Cardiovasc Imaging*. 2009;2:373-381.

[105] Wallhaus TR, Taylor M, Degrado TR, et al. Myocardial free fatty acid and glucose use after carvedilol treatment in patients with congestive heart failure. *Circulation*. 2001;103:2441-2446.

[106] Taegtmeyer H, Hems R, Krebs HA. Utilization of energy-providing substrates in the isolated working rat heart. *Biochem J*. 1980;186:701-711.

[107] Sharma S, Guthrie PH, Chan SS, et al. Glucose phosphorylation is required for insulin-dependent mTOR signalling in the heart. *Cardiovasc Res*. 2007;76:71-80.

[108] Taegtmeyer H. Glucose for the heart: too much of a good thing? *J Am Coll Cardiol*. 2005;46(1):49-50.

[109] Taegtmeyer H, Dilsizian V. Imaging myocardial metabolism and ischemic memory. *Nat Clin Pract Cardiovasc Med*. 2008;5 Suppl 2:S42-S48.

[110] Goodwin GW, Taylor CS, Taegtmeyer H. Regulation of energy metabolism of the heart during acute increase in heart work. *J Biol Chem*. 1998;273:29530-29539.

[111] Mochizuki T, Tsukamoto E, Ono T, et al. Sequential change of BMIPP uptake with age in spontaneously hypertensive rat model. *Ann Nucl Med*. 1997;11:299-306.

[112] de las FuentesL, Herrero P, Peterson LR, et al. Myocardial fatty acid metabolism: independent predictor of left ventricular mass in hypertensive heart disease. *Hypertension*. 2003;41:83-87.

[113] Wong KP, Sha W, Zhang X, Huang SC. Effects of administration route, dietary condition, and blood glucose level on kinetics and uptake of 18F-FDG in mice. *J Nucl Med*. 2011;52:800-807.

[114] Yokoyama I, Inoue Y, Moritan T, et al. Myocardial glucose utilisation in type II diabetes mellitus patients treated with sulphonylurea drugs. *Eur J Nucl Med Mol Imaging*. 2006;33:703-708.

[115] Botker HE, Goodwin GW, Holden JE, et al. Myocardial glucose uptake measured with fluorodeoxyglucose: a proposed method to account for variable lumped constants. *J Nucl Med*. 1999;40:1186-1196.

[116] Wiggers H, Bottcher M, Nielsen TT, et al. Measurement of myocardial glucose uptake in patients with ischemic cardiomyopathy: application of a new quantitative method using regional tracer kinetic information. *J Nucl Med*. 1999;40:1292-1300.

[117] Herrero P, Sharp TL, Dence C, et al. Comparison of 1-(11)C-glucose and (18)F-FDG for quantifying myocardial glucose use with PET. *J Nucl Med*. 2002;43:1530-1541.

[118] Nakamoto M, Ohya Y, Shinzato T et al. Pioglitazone, a thiazolidinedione derivative, attenuates left ventricular hypertrophy and fibrosis in salt-sensitive hypertension. *Hypertension Res*. 2008;31:353-361.

[119] Go A S, Mozaffarian D, Roger V L, et al. Heart disease and stroke statistics--2013 update: a report from the American Heart Association. *Circulation*, 2013, 127(1): e6.

[120] Dunn F G, Pringle S D. Left ventricular hypertrophy and myocardial ischemia in systemic hypertension. *The American journal of cardiology*, 1987, 60(17): 19-22.

[121] van Bilsen M, Smeets P J H, Gilde A J, et al. Metabolic remodelling of the failing heart: the cardiac burn-out syndrome? *Cardiovascular research*, 2004, 61(2): 218-226.

[122] Christe M E, Rodgers R L. Altered glucose and fatty acid oxidation in hearts of the spontaneously hypertensive rat. *Journal of molecular and cellular cardiology*, 1994, 26(10): 1371-1375.

[123] Allard M F, Schonekess B O, Henning S L, et al. Contribution of oxidative metabolism and glycolysis to ATP production in hypertrophied hearts. *American Journal of Physiology-Heart and Circulatory Physiology*, 1994, 267(2): H742-H750.

[124] Rajabi M, Kassiotis C, Razeghi P, et al. Return to the fetal gene program protects the stressed heart: a strong hypothesis. *Heart failure reviews*, 2007, 12(3-4): 331-343.

[125] Abel E D, Kaulbach H C, Tian R, et al. Cardiac hypertrophy with preserved contractile function after selective deletion of GLUT4 from the heart. *Journal of Clinical Investigation*, 1999, 104(12): 1703-1714.

[126] Ashrafian H, Frenneaux M P, Opie L H. Metabolic mechanisms in heart failure. *Circulation*, 2007, 116(4): 434-448.

[127] Ashrafian H, Neubauer S. Metabolic modulation in heart failure: high time for a definitive clinical trial. *Heart*, 2011, 97(4): 267-268.

[128] Ashrafian H, McKenna W J, Watkins H. Disease pathways and novel therapeutic targets in hypertrophic cardiomyopathy. *Circulation research*, 2011, 109(1): 86-96.

[129] Lopaschuk G D. Optimizing cardiac fatty acid and glucose metabolism as an approach to treating heart failure. *Seminars in cardiothoracic and vascular anesthesia. SAGE Publications*, 2006, 10(3): 228-230.

[130] Taegtmeyer H. Cardiac metabolism as a target for the treatment of heart failure. *Circulation*, 2004, 110(8): 894-896.

[131] Timmer S A J, Knaapen P. Coronary microvascular function, myocardial metabolism, and energetics in hypertrophic cardiomyopathy: insights from positron emission tomography. *European Heart Journal–Cardiovascular Imaging*, 2013, 14(2): 95-101.

[132] Gropler R J, Beanlands R S B, Dilsizian V, et al. Imaging myocardial metabolic remodeling. *Journal of Nuclear Medicine*, 2010, 51(Supplement 1): 88S-101S.

[133] Gropler R J. Recent advances in metabolic imaging. *Journal of Nuclear Cardiology*, 2013, 20(6): 1147-1172.

[134] Osterholt M, Sen S, Dilsizian V, et al. Targeted metabolic imaging to improve the management of heart disease. *JACC: Cardiovascular Imaging*, 2012, 5(2): 214-226.

[135] Devereux R B, Reichek N. Echocardiographic determination of left ventricular mass in man. Anatomic validation of the method. *Circulation*, 1977, 55(4): 613-618.

[136] Rockman H A, Ross R S, Harris A N, et al. Segregation of atrial-specific and inducible expression of an atrial natriuretic factor transgene in an in vivo murine model of cardiac hypertrophy. *Proceedings of the National Academy of Sciences*, 1991, 88(18): 8277-8281.

[137] Ingelsson E, Sundström J, Ärnlöv J, et al. Insulin resistance and risk of congestive heart failure. *Jama*, 2005, 294(3): 334-341.

[138] Kao D P, Witteles R M, Quon A, et al. Rosiglitazone increases myocardial glucose metabolism in insulin-resistant cardiomyopathy. *Journal of the American College of Cardiology*, 2010, 55(9): 926-927.

[139] Rubin J, Matsushita K, Ballantyne C M, et al. Chronic hyperglycemia and subclinical myocardial injury. *Journal of the American College of Cardiology*, 2012, 59(5): 484-489.

[140] Nissen S E, Wolski K. Effect of rosiglitazone on the risk of myocardial infarction and death from cardiovascular causes. *New England Journal of Medicine*, 2007, 356(24): 2457-2471.

[141] Di Carli M F, Charytan D, McMahon G T, et al. Coronary circulatory function in patients with the metabolic syndrome. *Journal of Nuclear Medicine*, 2011, 52(9): 1369-1377.

[142] Croteau E, Gascon S, Langlois R, et al. [^{11}C] Acetate rest–stress protocol to assess myocardial perfusion and oxygen consumption reserve in a model of congestive heart failure in rats. *Nuclear medicine and biology*, 2012, 39(2): 287-294.

[143] Ziadi M C, Williams K A, Guo A, et al. Impaired myocardial flow reserve on rubidium-82 positron emission tomography imaging predicts adverse outcomes in patients assessed for myocardial ischemia. *Journal of the American College of Cardiology*, 2011, 58(7): 740-748.

[144] Ziadi M C, Williams K, Guo A, et al. Does quantification of myocardial flow reserve using rubidium-82 positron emission tomography facilitate detection of multivessel coronary artery disease? *Journal of Nuclear Cardiology*, 2012, 19(4): 670-680.

[145] Fiechter M, Gebhard C, Ghadri J R, et al. Myocardial perfusion imaging with ^{13}N-Ammonia PET is a strong predictor for outcome. *International journal of cardiology*, 2013, 167(3): 1023-1026.

[146] Berman D S, Germano G, Slomka P J. Improvement in PET myocardial perfusion image quality and quantification with flurpiridaz F-18. *Journal of Nuclear Cardiology*, 2012, 19(1): 38-45.

[147] Lamoureux M, Thorn S, Dumouchel T, et al. Uniformity and repeatability of normal resting myocardial blood flow in rats using [13N]-ammonia and small animal PET. *Nuclear medicine communications*, 2012, 33(9): 917-925.

[148] Croteau E, Bénard F, Bentourkia M, et al. Quantitative myocardial perfusion and coronary reserve in rats with 13N-ammonia and small animal PET: impact of anesthesia and pharmacologic stress agents. *Journal of Nuclear Medicine*, 2004, 45(11): 1924-1930.

[149] Inubushi M, Jordan M C, Roos K P, et al. Nitrogen-13 ammonia cardiac positron emission tomography in mice: effects of clonidine-induced changes in cardiac work on myocardial perfusion. *European journal of nuclear medicine and molecular imaging*, 2004, 31(1): 110-116.

[150] Vaquero J J, Gao D W, García-Villaba C, et al. Approach to assessing myocardial perfusion in rats using static [13N]-ammonia images and a small-animal PET. *Molecular Imaging and Biology*, 2012, 14(5): 541-545.

[151] Vandsburger M H, Janiczek R L, Xu Y, et al. Improved arterial spin labeling after myocardial infarction in mice using cardiac and respiratory gated look‐locker imaging with fuzzy C‐means clustering. Magnetic Resonance in Medicine, 2010, 63(3): 648-657.

[152] Makowski M, Jansen C, Webb I, et al. First‐pass contrast‐enhanced myocardial perfusion MRI in mice on a 3‐T clinical MR scanner. *Magnetic Resonance in Medicine*, 2010, 64(6): 1592-1598.

[153] Cerqueira M D, Weissman N J, Dilsizian V, et al. Standardized myocardial segmentation and nomenclature for tomographic imaging of the heart a statement for healthcare professionals from the cardiac imaging committee of the Council on

Clinical Cardiology of the American Heart Association. *Circulation*, 2002, 105(4): 539-542.

[154] Bentourkia M, Croteau T, Langlois R, et al. Cardiac studies in rats with 11 C-acetate and PET: a comparison with 13 N-ammonia. *Nuclear Science, IEEE Transactions on*, 2002, 49(5): 2322-2327.